August 2017

River Influence on the Nearshore Ecosystem of Western Lake Superior

Joshua Delvaux
University of Wisconsin-Milwaukee

RIVER INFLUENCE ON THE NEARSHORE ECOSYSTEM OF WESTERN LAKE SUPERIOR

by

Joshua M. Delvaux

A Thesis Submitted in

Partial Fulfillment of the

Requirements for the Degree of

Master of Science

in Freshwater Sciences and Technology

at

The University of Wisconsin-Milwaukee

August 2017

ABSTRACT

RIVER INFLUENCE ON THE NEARSHORE ECOSYSTEM
OF WESTERN LAKE SUPERIOR

by

Joshua M. Delvaux

The University of Wisconsin-Milwaukee, 2017
Under the Supervision of Professor Harvey A. Bootsma

As the interface between the terrestrial landscape and the open lake, nearshore areas of the Great Lakes play an important role in modulating whole-lake response to inputs of nutrients and energy from the watershed. These inputs occur primarily via tributary loading, and so it is critical to understand the dynamics of river plumes and the fate of organic carbon and nutrients delivered in the plumes. To assess the influence of river plumes on the biogeochemistry and metabolism of the Lake Superior nearshore zone, the spatial and temporal distribution of turbidity, nutrients, phytoplankton, dissolved oxygen, and dissolved carbon dioxide were measured in the western arm of Lake Superior and select tributaries from June 2016 through October 2016. This study focused on the nearshore ecosystem response to a large storm even in July, showing how the nearshore zone transitioned from a highly turbid, low productivity system immediately following the storm to high phytoplankton productivity after a one-month lag. A steady decrease in surface pCO2 in the month following suggests that increased water clarity and nutrient concentration following the plume event drive nearshore primary production. The shift towards net heterotrophy immediately following the storm event appears to be more so due to decreased water clarity and associated suppressed phytoplankton primary production rather than increased biological breakdown of dissolved organic carbon.

TABLE OF CONTENTS

LIST OF FIGURES

LIST OF TABLES

LIST OF EQUATIONS

LIST OF SYMBOLS

Q	= discharge ($m^3\ s^{-1}$)
A	= area (km^2)
R_{rs}	= remote reflectance at the surface (sr^{-1})
z	= depth (m)
EC_{25}	= electrical conductivity normalized to 25°C
Alk_{carb}	= carbonate alkalinity ($\mu eq\ L^{-1}$)
k_T	= light extinction coefficient (m^{-1})
k_1	= First dissociation constant of carbonic acid
k_2	= Second dissociation constant of carbonic acid
p	= partial pressure (ppm)
k_H	= Henry's constant
$k_H^{\ominus}$	= Henry's constant standardized to 298.15 K
$_{\Delta soln}H/R$	= enthalpy of water for the dissolution of specific gas
T	= temperature
$T^{\ominus}$	= temperature standardized to 298.15 K
F	= gas flux
$[c]$	= variable representing concentration of gas
S	= salinity (psu)
K	= piston velocity ($m\ s^{-1}$)
k_{600}	= gas transfer velocity corrected for temperature ($m\ s^{-1}$)
U_{10}	= wind velocity at 10 m ($m\ s^{-1}$)
Sc	= Schmidt number

ACKNOWLEDGEMENTS

This research would not have been possible without the financial support of the National Park Service (NPS), and the efforts of Ms. Shania Leask, Dr. Brenda Moraska Lafrancois, Mr. Jay Glase of the NPS, and Cpt. Mike Garnich of Good Earth Outfitters, LLC in assisting me with my field work. Furthermore, I am especially indebted to my adviser, Dr. Harvey Bootsma, who provided me with this amazing opportunity, was supportive in my endeavors, and provided me with sound advice throughout this process. I am grateful to Ben Turschak, among others at the School of Freshwater Sciences, who provided assistance and constructive criticism throughout the course of this project. Finally, I would like to thank my committee members Dr. Laodong Guo, Dr. Jim Waples, and Dr. Brenda Moraska Lafrancois for their input and taking the time to be a part of my committee.

Chapter 1: Introduction and Background

The Great Lakes basin is an immense ecosystem covering more than 780,000 km^2 (Wolter et al., 2006) and spanning 9^o of latitude and 19^o of longitude. Within this ecosystem, the Laurentian Great Lakes are the most prominent feature. These lakes have a combined surface area of about 244,000 km^2 and a volume of 22,700 km^3, which makes them the single largest collection of fresh water in the world, apart from polar ice caps and ground water (Herdendorf, 1982). Despite their vast overall size, humans have dramatically altered the Great Lakes basin through agricultural practices, urban development, industrial, commercial, and recreational activities, as well as the introduction of non-native species (Mackey and Goforth, 2005; Niemi et al., 2009; Homer et al., 2015).

These combined stressors have altered the chemistry, biological composition, productivity, and resiliency of these natural ecosystems. At the same time, they continue to provide critical resources to communities throughout the region, in terms of cultural and economic benefits. Cumulative stress is often the greatest in nearshore zones of the Great Lakes (Allan et al., 2013). Nearshore zones are dynamic transition zones between the terrestrial landscape and the open-lake, and as such they are susceptible to anthropogenic influences (Chu et al., 2014). Despite their obvious societal importance and current stressors, nearshore ecosystems have received little scientific attention in comparison to the open lake (Niemi et al., 2009; Vadeboncoeur et al., 2011).

The nearshore zones of the Great Lakes are heterogeneous ecosystems characterized by unique circulation patterns (Rao and Schwab, 2007; Boyce, 1974) and high biodiversity relative to offshore waters (Vadeboncoeur et al., 2011). Although these zones perform key ecosystem functions such as facilitating the lateral transfer of nutrients and energy to pelagic ecosystems,

the exact definition as to what constitutes the nearshore zone of large lakes is still debated. Some (Kelly et al., 2015; Yurista et al., 2015) describe the nearshore zone as 0-30 m in depth and less than 5 km from the shore. Here, depth and distance serve as simple, operational distinctions between nearshore and offshore zones. Using a different perspective, Edsall and Charlton (1997) describe nearshore zones as regions where the thermocline intersects the lake bed once stratification has firmly established. This definition can occasionally lead to significant differences between lakes, however. For example, Lake Erie's thermocline develops at 20-30 m which is approximately the average depth of the entire lake, and encompasses most of the western basin (Edsall and Charlton, 1997). In comparison, deeper Lake Superior typically forms a thermocline at 10-20 m, and only a small proportion of the lake is classified as nearshore due to its steeply sloped sides. The stratified season in the Great Lakes typically begins mid- to late-June and ends in late-September to early-October (Austin and Colman, 2007). Therefore, for the purposes of this project, hydrodynamic patterns may provide the best means of delineating the nearshore zone.

The hydrodynamic regimes of large lakes are not all uniform but vary accordingly with depth, lake size, and morphometry. Spatial variations in the hydrodynamics of large lakes allow for the characterization of the nearshore zone, relative to offshore waters. Momentum in the open lake is driven by wind stress resulting in near-inertial oscillations that are balanced by the Coriolis force, including internal seiches and Poincaré waves (Mortimer, 2006; Ahmed et al., 2014). Winds blowing over a lake transfer kinetic energy to the lake surface, and this energy subsequently propagates through the water column due to internal friction. The strength of these oscillations is directly related to the strength of stratification; when stratification exists, the magnitude and duration of near-inertial oscillations increases (Austin, 2013). The current

patterns of the open lake tend to mirror variations in wind patterns, with a deflection to the right in the northern hemisphere, at the lake surface. Currents at greater depths within the epilimnion become progressively weaker and are often directed farther to the right under the influence of Coriolis Effect. The influence of wind on water movement often disappears below 20-30 m (Csanady, 1972), and currents below these depths are typically 180^{o} out of phase with those above (Austin, 2013). Although the prevailing winds of the Great Lakes region typically blow from the southwest and west, winds at mid-latitudes are highly variable. Winds from other directions are frequent, and periods of winds out of the east or northeast are not unusual. Therefore, wind-driven movement of water is highly episodic and subject to rapid changes. In large lakes, open lake circulation is driven primarily by wind stress, and geostrophic flow is often of minimal importance (Beletsky et al., 1999; Bennington et al., 2010; Thupacki, 2012; Csanady, 2013).

Several researchers (Murthy and Rao, 2003; Rao and Schwab, 2007) have illustrated the significance of open-lake circulation patterns on nearshore hydrodynamics of large lakes. Rao and Schwab (2007), in particular, provide an extensive review of mechanisms influencing the dynamics of water movement within the nearshore. Hydrodynamic patterns in the nearshore zone of large lakes are highly turbulent, and a result of the interaction between the coastal boundary and open-lake circulation patterns. Rao and Schwab (2007) describe the nearshore zone as the region between the wave breaking zone and the open lake, where bottom frictional forces and the diverting effect of the shoreline are dominant processes. Within the nearshore zone, wind stress is still the primary driving force of circulation.

The nearshore zone can be sub-divided into the Frictional Boundary Layer (FBL) and the Inertial Boundary Layer (IBL), based on the relative importance of frictional and inertial forces

respectively. In Lake Huron, Murthy and Dunbar (1981) identified the IBL and FBL to extend approximately 10 km and 2 km offshore, respectively; however, these distinctions may vary between lakes. In their study, fluctuations in kinetic energy were used to delineate the different layers of the nearshore zone. Kinetic energy increases with distance offshore, as near-inertial oscillations become more dominant, and develops a peak at the interface between the FBL and IBL. Within the FBL, current patterns are directly influenced by bottom and shoreline friction.

As wind-driven waves propagate from the open-lake toward the shore, the decreasing depth alters the wave kinematics (Boyce, 1974). Within the nearshore zone, shallower depths result in increased bottom friction. The vertical, circular motion found in open water waves shifts to elliptical orbits as waves propagate to the bottom (Wetzel, 2001; Yang et al., 2013). Waves within the nearshore are no longer energy dispersive, and the influence of the bottom causes velocity and wavelength to decrease while amplitude increases. As a result of the steepening of the wave in shallow water, the wave gradually becomes asymmetric, unstable, and finally breaks. Breaking waves transfer potential energy stored within the wave to kinetic energy, which acts on the lake bottom and shoreline (Eadie et al., 2002; Yang et al., 2013). Close to shore, wave-driven turbulence extends to the bottom of the lake, affecting sediment-water exchange and resulting in occasional sediment resuspension events, which can affect the transport of carbon and nutrients, as well as the light environment (Eadie et al., 2002). Within the wave-breaking zone of the FBL, longshore current, which flows parallel to shore, is generated by the stresses associated with the breaking process of obliquely incoming waves. Longshore current contributes to the transport of sediment along the shoreline, and therefore to the accretion and erosion of the shoreline as well as the entrapment of riverine input (Jackson et al., 2017). It is important to note that episodic wind, out of different directions, may occasionally reverse mean longshore current patterns. This

abrupt change in longshore current patterns was illustrated by Bennington et al. (2010) for the western region of Lake Superior. This region where bottom and shoreline frictional forces dominate constitutes the FBL, and extends between 2-3 km offshore (Murthy and Dunbar, 1981; Rao and Schwab, 2007).

Beyond 3 km, the adjustment of open-lake inertial oscillations for the shoreline forms the IBL (Murthy and Dunbar, 1981; Rao and Schwab, 2007). The presence of the shoreline acts as a lateral constraint on water movements, tending to divert currents so that they flow nearly parallel to the shoreline (Rao and Murthy, 2001). In the nearshore zone, a near balance exists between the Coriolis force, wind stress, and horizontal pressure gradients. Following a strong wind event, the balance between these factors gives rise to internal and surface Kelvin waves. These waves are coastally trapped oscillations of the thermocline or surface water that propagate with the shoreline to the right in the northern hemisphere. The Coriolis force results in wind-driven waves to deflect to the right; however, the coast prevents these waves from turning right, and instead causes water to pile up along the shoreline. The pile up of water causes a horizontal pressure gradient to develop, directed offshore. This results in a geostrophic, coastal current traveling along the shoreline (Jackson, 1988; Wang, 2002). The offshore extent of these currents and the IBL depends on the thermal structure and morphometry of the lake basin.

The main driving force of circulation within the nearshore zone is wind stress; however, stratification can become very influential during the summer. During the stratified season, significant wind events cause rhythmic motions, including both oscillations of the water surface and internal oscillations at the thermocline. The motion of a surface seiche is barotropic, whereas the motion of an internal seiche is baroclinic and is associated with the maximum density gradient in stratified lakes. As a steady wind blows across the lake, the lake forms a depression

along the upwind end, and an increase in elevation along the downwind end. Following the wind event, momentum generated by the wind is great and equilibrium is overshot causing the lake to rock back and forth (Ji and Jen, 2006). At the downwind end, where the water level is elevated, the resultant pressure gradient causes water to flow towards deeper parts of the lake. In large lakes, the Coriolis force causes these oscillations to rotate clockwise in the northern hemisphere around the lake basin (Wetzel, 2001). Patterns in upwelling and downwelling are marked by corresponding changes in the thermal structure of the lake. The nearshore zone is exposed to cold, hypolimnetic water during periods of upwelling, whereas downwelling events expose the zone to warm, epilimnetic water. Seiches occur as a result of steady or extreme wind events, and have a significant impact on biological processes within the nearshore as well as the lateral nearshore-offshore transfer of materials and water.

Upwelling events could provide a substantial source of nutrients to the nearshore zone and result in increased primary productivity within the nearshore. In some lakes, increases in productivity following the introduction of hypolimnetic nutrients as a result of upwelling events are well known (Hecky et al., 1996). Evidence suggests upwelling is vital to the metabolic dynamics of meromictic lakes, where seasonal mixing is incomplete (Corman et al., 2010). The importance of upwelling events as a potential source of nutrients in the Great Lakes is not as well understood. Lesht et al. (2002) suggest a phytoplankton bloom that accounted for approximately 25% of Lake Michigan's annual offshore primary production was a result of a significant upwelling event. In Lake Superior, Heinen and McManus (2004) show that roughly 50% of the total phosphorus input to the water column originates in the hypolimnion, and is introduced via resuspension or upwelling events. Although the benthic flux of nutrients during these events in Lake Superior is quite large, nutrient reintroduction from these events may not be important to

the spatial variation in plankton biomass (Megard et al., 1997). Although not addressed here, clearly more research is needed to determine the importance of upwelling events as a potential nutrient source for nearshore ecosystems of the Great Lakes.

Discharge from surrounding rivers may also significantly alter the thermal structure and hydrodynamics of the nearshore. For example, Rao and Schwab (2007) discuss the influence of warm Niagara River inflow on the nearshore thermal structure of Lake Ontario. The resultant surface plume from Niagara River inflow extends from the river mouth in excess of 10 km, after which it mixes with lake water (Murthy et al., 1986). The warmer, less dense inflowing water develops a thermal front as it enters Lake Ontario. The resultant density gradient depends on the time of year, and therefore, the difference between the density of the Niagara River and ambient lake water. Strong density gradients may develop as a result of these inflows, and constrain riverine input of nutrients, energy, and sediment to the nearshore. Prevailing wind nearshore circulation patterns also play a role in regulating the lateral transport of riverine input between the nearshore and offshore, as well as along the shoreline. During periods of weak or calm wind conditions, the current in the nearshore zone is generally weak (Csanady, 1972). Therefore, river discharge during these periods tends to hug the shoreline, with limited lateral transfer, leading to nearshore entrapment of nutrients and energy. However, significant nearshore-offshore exchange of nutrients and energy take place during episodic events (Rao and Schwab, 2007).

The unique hydrodynamic patterns of the nearshore zone, and the associated physical transport and dispersal processes are complex. Nearshore hydrodynamics are an important factor in mediating the chemical and biological processes occurring within the nearshore ecosystem. The hydrodynamic patterns within the nearshore also significantly influence the lateral transfer of essential nutrients and materials to offshore ecosystems. Therefore, a thorough

comprehension of the physical processes of the nearshore zone is vital to the understanding of spatiotemporal variability in the chemical and biological dynamics within the nearshore, as well as the whole-lake.

Despite the lack of a definitive, simple, operational definition of the nearshore zone of larges lakes, these zones are integral components of large lake ecosystems. To emphasize their importance, the nearshore zone of Lake Superior contains approximately 90% of its overall species diversity (Vadeboncoeur et al., 2011). Nearshore zones of large lakes provide a variety of energy sources (Vadeboncoeur et al., 2002), a wide range of habitat (Gray, 1997), warmer water (Austin and Colman, 2008), and an abundance of nutrients (Hall et al., 2003; Makarewicz et al., 2012), all of which support increased biodiversity. In some large lakes, many fishes and other organisms are dependent on nearshore energy sources (Hecky and Hesslein, 1995; Bootsma et al., 1996; Vadeboncoeur et al., 2002; Turschak et al., 2014). These nearshore zones are typically more productive and consist of multiple, basal energy sources (i.e. benthic and pelagic primary production, and terrestrial organic matter) in comparison to the open lake. This greater productivity within the nearshore is often associated with nutrient (typically phosphorus) loading due to the proximity of these zones to the surrounding watershed (Vollenweider, 1976; Schindler, 1978). For example, Wawrick and Paul (2004) showed that Mississippi River input of nutrients to the oligotrophic Gulf of Mexico supports increased primary productivity during periods of increased inflow. In oligotrophic systems, like Lake Superior, studies have shown that phosphorus availability regulates autotrophic growth (Guildford and Hecky, 2000; Sterner, 2010), biomass transfer efficiency (San Martin et al., 2006), species composition (Ivanikova et al., 2007), and both vertical and horizontal distribution of phytoplankton biomass (Popovskaya,

2000). Makarewicz et al. (2012) showed how influential river plumes are in modulating nutrient availability in nearshore Lake Ontario.

While the loading of phosphorus to the nearshore zone may promote algal production, dissolved and particulate matter that is introduced in conjunction with nutrients may serve as a potential inhibitor of photosynthetic primary production. In lakes with highly turbid riverine input, phytoplankton and benthic algae in proximity to shore are often light-limited (Karlsson et al., 2009). Although autotrophs may be adversely affected by low light in nearshore, heterotrophic bacteria may be able to utilize these allochthonous subsidies as a metabolic substrate and introduce these subsidies into the food web through "microbial loop" pathways (Azam et al., 1983; Tranvik, 1992; Pomeroy et al., 2007). In fact, allochthonous organic matter has been shown to support 30-60% of bacterial respiration in some small northern temperate lakes (Kritzberg et al., 2004). Although the Great Lakes are substantially larger, these allochthonous subsidies may be of significance in nearshore zones. For example, Biddanda and Cotner (2002) estimated allochthonous inputs from terrestrial origin via rivers could support 10-20% of net community metabolism in southern Lake Michigan. The spatial extent of the nearshore in comparison to the whole-lake belies their importance in supporting the biological communities of the lake ecosystem (Kalff, 2002).

The western region of Lake Superior provides an ideal location to study the effects of riverine input on physical, chemical, and biological processes in the nearshore zone. In comparison to most of Lake Superior, the western region of the lake exhibits much more gradual descending slopes. These shallow, gently sloping plains may provide essential habitat for periphyton communities provided these zones are also well-lit (Vadeboncoeur et al., 2008). There is sufficient evidence to suggest that within the nearshore ecosystem of large lakes

phytoplankton and periphyton are equally important to ecosystem primary productivity (Bootsma et al., 1996l; Yoshii, 1999). Vadeboncoeur et al. (2001) found that in small, Michigan lakes benthic algae accounted for between 50-80% of whole-lake primary production. However, the relative importance of benthic primary production versus phytoplankton production depends on dissolved nutrient concentrations and water clarity. At high nutrient concentrations, high phytoplankton biomass causes corresponding decreases in water clarity which negatively affects periphyton communities (Vadeboncoeur et al., 2001).

Not only does the western region of Lake Superior contain countless tributaries, it also boasts some of the lake's largest, including the St. Louis and Nemadji Rivers. These rivers may serve as a source of both nutrients, which can support increased benthic and pelagic autotrophic production, as well as organic matter, which can support bacterial production. In addition to organic material, suspended sediment, including soil and clay, will also affect the nearshore light regime. Easily erodible red clay found along the shoreline of Lake Superior from Superior, WI to the Apostle Islands, often results in frequent and visible plumes within the nearshore zone. Mouw et al. (2013) illustrated the negative influence light absorption due to CDOM may have on the availability of light to autotrophs in western Lake Superior. Furthermore, Minor et al. (2014) suggested primary producers in this region transitioned from nutrient- to light-limitation following these river plumes. Minor et al. (2014), however, did not examine the changes in community metabolic patterns at the outer edges of these plumes where light availability may have been adequate for autotrophs to photosynthesize. Rather, their results highlighted the lack of autotroph response to riverine nutrient loading in the nearshore zone. By contrast, a previous study (Russ et al., 2004) found that autotrophic production tends to be greater in the western region of Lake Superior than other parts of the lake, highlighting the potential significance of

riverine nutrient loading to this part of the lake, and suggesting that autotrophs can take advantage of these nutrients if light is sufficient.

The extent to which the chemical and metabolic processes of nearshore zones vary in space and time due to riverine input is not well understood in large lakes. According to Yurista et al. (2011), few studies describe the broad, complex relationship between riverine input and the nearshore ecosystem. Rao and Schwab (2007) also emphasize the need for more studies to understand the effects of riverine input on the nearshore water quality of large lakes. The research presented here not only focuses on river loading during the summer but also addresses the nearshore physicochemical and metabolic response to these inputs. The overarching objective of this project was to describe the nearshore ecosystem spatiotemporal response to river plumes. Transport of nutrients and energy from the surrounding watershed via river loading may drive fluctuations in primary production and respiration of large lake ecosystems. That is, episodic river plumes may effectively control the metabolic processes occurring within the nearshore on short-term basis, as well as the lateral transport of nutrients and energy offshore.

In Chapter 2, the physical response as well as nutrient and organic carbon dynamics are illustrated through a time-series, encapsulating a large river plume event in western Lake Superior. The patterns in the physical distribution, both vertical and horizontal, of the plume are first identified and characterized. The distribution and dynamics of nutrient and energy inputs are regulated by plume dispersal and general circulation patterns (Halder et al., 2012). Physical processes often drive biological and chemical processes; therefore, examining the hydrodynamics in conjunction with the chemical and biological processes of this region following a plume affords a holistic understanding of the nearshore ecosystem.

The physical and chemical dynamics of western Lake Superior's nearshore following a plume event reported in this chapter provide a foundation for the following chapter (Chapter 3), which builds on the previous chapter by assessing the nearshore community metabolic response to large river plumes in western Lake Superior. Vertical profiles of dissolved gases, as well as gas flux measurements were used to qualitatively assess spatial and temporal variability in primary production and respiration following a river plume. Significant input of vital nutrients from rivers has been shown to subsidize phytoplankton (Wawrick and Paul, 2004) and benthic algal production (Jassby et al., 1993). However, decreased water clarity may diminish primary production (Minor et al., 2010) while allowing bacterial respiration to dominate (del Giorgio and Peters, 1997). Therefore, it is critical to understand nearshore patterns and fluctuations in primary production and respiration in response to river inflow.

Finally, Chapter 4 serves as summation of the previous chapters. Here, broad conclusions regarding river influence on Great Lakes nearshore ecosystems are drawn from the hydrodynamic, nutrient and energy dynamics, and community metabolism topics of the preceding chapters. These results are put into a broader context by comparison with nutrient and carbon dynamics in Lake Superior at the whole-lake scale, and by comparison with other lakes.

Chapter 2: Physical, Chemical, and Biological Response to a Large Storm Event in the Nearshore Zone of Lake Superior

Introduction

The transport of water from a river to a lake ecosystem can be an important ecological regulator. Riverine loading of particulate and dissolved organic material, as well as nutrients, can have a significant influence on the physical, chemical, and biological processes in the nearshore zone of large lakes. River systems serve as conduits transporting nutrients and energy from the watershed to receiving lake basins. Variations in watershed size (Steinman et al., 2009) and characteristics, such as soil type (Frost et al., 2006) and land-use (Yurista et al., 2011), drive changes in the amount and composition of river input at baseline conditions. Yurista et al. (2011), in particular, illustrated how spatial patterns in Lake Superior nearshore plankton and water quality properties were strongly predicted by variations in adjacent watershed land-use. Loadings of nutrients, organic carbon, and suspended matter may vary significantly from river-to-river. However, few studies have examined the collective influence of multiple rivers on lake ecosystems

Episodic, storm inflow events are capable of providing a substantial fraction of the annual nutrient and organic carbon load. For example, Inamdar et al. (2006) found that large storm events contributed a relatively small fraction of the annual discharge but one-third of the annual input of dissolved organic carbon in certain lakes of New York. In Lake Malawi, McCullough et al. (2007) showed that immediately following a storm event the suspended sediment load of the Linthipe River increased three-fold, and remained relatively high for about a week until returning to pre-storm conditions. The ecological response of these recipient ecosystems to such episodic

events depends to a large degree on the dispersal of the inflowing river water and the associated dissolved and particulate components.

The distribution of river water entering a lake can take various forms depending on the density of the inflowing water relative to the density of the receiving lake water. A river plume may float on the lake surface, may sink to a depth within the water column, or may remain confined to the lake bottom depending on the density of inflow, which is influenced by temperature, salinity, and suspended solids load. If the plume reaches a depth of neutral buoyancy, it will flow through the water column as an intrusion and spread horizontally along a gradient of equal density. The depth and extent of the intrusion is dependent on the density of the inflowing river, lake stratification, and the turbulent mixing between the two water masses (Hogg et al., 2013; Scheu et al., 2015).In large lakes with many inflowing rivers, the mixing between the rivers and the lake can be complex due to multiple river sources with differing loads and densities, as well as lake circulation patterns.

Flow regimes of large lakes can potentially constrain riverine inputs to the nearshore while allowing for minimal lateral transfer to offshore water (Rao & Schwab, 2007). In large lakes, episodic river input often forms a geostrophic alongshore current of turbid, nutrient-rich water, which results in retention of nutrients and energy within the nearshore area. For example, in western Lake Superior summer circulation patterns are typically cyclonic, with nearshore currents running parallel to the shore in a counterclockwise direction (Beletsky et al., 1999; Bennington et al., 2010). Geostrophic balance causes river inflow to be relatively constricted to the nearshore along the southern shoreline of western Lake Superior, as illustrated in satellite imagery (Fig. 2.1). This entrapment of nutrients within the nearshore, along with warmer temperatures, often results in higher species diversity and increased phytoplankton biomass in

comparison to the offshore. Thus, the nearshore and offshore zones of large lakes can be considered distinct, albeit connected, ecosystems. Since few studies focus specifically on the nearshore relative to offshore zones (Niemi et al., 2009; Vadeboncoeur et al., 2011), more research is required to fully understand the spatial and temporal variability in the distribution of nutrients, organic carbon, and phytoplankton within the nearshore zone. More specifically, how do nutrient and organic carbon pools and phytoplankton in the nearshore respond to episodic river inflow events.

The horizontal and vertical dispersal of river inflow plays a critical role in determining the distribution of organic carbon and nutrients delivered to the nearshore (Halder et al., 2012). The mixing of river and lake water, as a function of density and turbulence, may restrict these inputs to specific regions within the water column. This entrainment of nutrients and organic carbon may result in strong chemical gradients that may influence the distribution of lake biota. Most large lake ecosystems are nutrient-poor and, consequently, have sparse phytoplankton communities (Vollenweider et al., 1974; Guildford et al., 2000). In temperate and tropical lakes, the distribution of phytoplankton biomass has been shown to vary in response to nutrient loading from specific regions of the watershed (George & Jones, 1987).

Phytoplankton productivity and biomass is often greater at the edge of the pelagic zone close to the perimeter of the lake (Wetzel, 2001). Here, the availability of essential nutrients, such as dissolved phosphorus, is greater and light is sufficient to allow for increased primary production, due to a shallow mixed layer. The depth of the euphotic zone in Lake Superior (25 m inshore and 29 m offshore) suggests light penetration is sufficient enough throughout the lake to support phytoplankton growth within the mixed layer, between 10 and 15.m (Nalewajko et al., 1981). Thus, at the edges of surface, river plumes, where water clarity remains high,

phytoplankton may be able to efficiently utilize increased dissolved phosphorus concentrations. In large lakes, this horizontal variability in phytoplankton biomass becomes even more apparent. For example, Popovskaya (2000) suggested greater phytoplankton biomass near the Selenga Delta in Lake Baikal was a result of warmer, nutrient-rich, river input. In Lake Superior, Auer and Bub (2004) reported high spatial variability in phytoplankton biomass along the Keweenaw Peninsula which seems to reflect the impact of point-source riverine nutrient loading.

Nutrient influx is not the only variable controlling the distribution of phytoplankton communities. As the transition between the well-lit water of the epilimnion and darker, deeper water, the thermocline plays a vital role in determining the biological properties of the water column in Lake Superior (Barbiero and Tuchman, 2004). During stratified periods, the presence of a deep chlorophyll maximum is a persistent phenomenon in many large lake ecosystems (Padisák et al., 1997; Salonen et al., 1999; Barbiero and Tuchman, 2001, Barbiero and Tuchman, 2004; Fietz et al., 2005). For example, Barbiero and Tuchman (2004) found consistent deep chlorophyll maxima in stratified regions of Lake Superior at depths ranging from 23-35m. Although light is a necessity for phytoplankton to photosynthesize, under extremely high light intensities phytoplankton communities may be photoinhibited by the excess light (Peterson et al., 1987). In large, nutrient-poor lakes, phytoplankton biomass may be greater in deeper water where there is an adequate nutrient pool as well as near-optimal light intensity.

Episodic influxes of nutrients may reduce the depth of phytoplankton biomass in large lakes in response to decreased light intensity caused by suspended particulate matter. It is important to note, however, that river loading of suspended particulate matter does not always equate to high loading of nutrients. For example, rivers, such as the Nemadji and Iron Rivers, within the red clay plain of western region of Lake Superior do not provide a significant source

of nutrients. Although red clay does not contribute a large quantity of nutrients, it may serve to transport nutrients contributed from sources outside of the red clay plain. A large portion of the St. Louis and Bois Brule River watersheds lie outside of the plain, and, therefore, may contribute a significant amount of nutrients during episodic events (USEPA 1979).

The western region of Lake Superior may be disproportionately affected by these inflows due to the dominance of shallow waters, high tributary loading, and easily erodible shoreline. Measuring the physical and chemical dynamics of this region following an episodic inflow event provides insight as to how the distribution of phytoplankton and the nutrient and organic carbon within the nearshore ecosystem responds to such an event.

There are several hypotheses I address in this chapter: 1) in addition to surface riverine inflow, subsurface intrusions are a dominant occurrence in this region, 2) the flowpath of river inflow results in distinct layers or regions of increased concentrations of nutrients and organic carbon within the nearshore zone, and 3) phytoplankton response to river loading is determined by both nutrient input and water clarity. The objectives of this chapter are three-fold: 1) provide a representation of the dispersal of an episodic river inflow, 2) quantify the dynamics of the total phosphorus and organic carbon in the nearshore before, during, and after such an event, and 3) determine how phytoplankton responded to such an event.

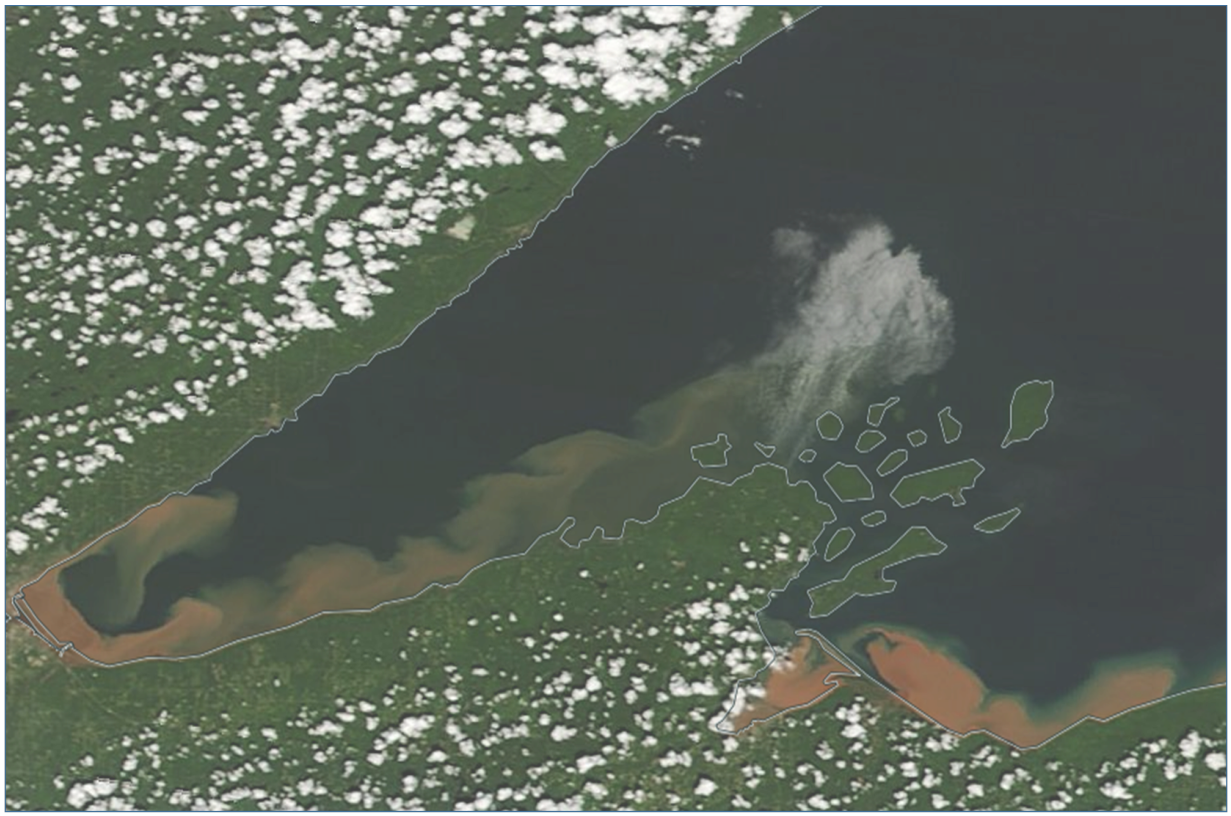

Figure 2.1: MODIS Aqua satellite true color image of western Lake Superior on July 16, 2016, illustrating the resultant surface plume following the southern shoreline after a major rain event on July 13, 2016. Accessed on November 21, 2016 from https://worldview.earthdata.nasa.gov/

Methods

Sampling Frequency & Spatial Coverage

The fieldwork in western Lake Superior to determine the influence of river inflows on the nearshore ecosystem was conducted on multiple trips using the National Park Service *Vessel Grebe* and a third party (Good Earth Outfitters, LLC; Cpt. Mike Garnich) vessel out of Cornucopia, WI. Specific dates of each trip are described in Table 2.1.Sampling began in June 2016 and continued until October 2016.

During the course of fieldwork, a major storm event in this region resulted in over 20 cm of precipitation falling on the lake and surrounding watershed on July 12, 2016, and produced a 500-year flood event in the subsequent days. In the days following the storm, a significant surface river plume within the western region of Lake Superior developed (see Fig. 2.1). The distribution of sampling trips encapsulated this event, thereby, providing a time-series (before, during, and after) analysis as to river inflow dynamics and the nearshore ecosystem chemical and biological response.

Each sampling trip included one day of river sampling and one day of nearshore-offshore transect sampling. A spatial representation of the nearshore-offshore transect, as well as the rivers sampled is shown in Fig. 2.2. The location of the nearshore-offshore transect, as well as each river, was chosen for specific reasons. In western Lake Superior, water typically circulates in a cyclonic pattern during the summer (Beletsky et al., 1999; Bennington et al., 2010) often resulting in geostrophic currents traveling parallel to shore along the southern shoreline. These current patterns force riverine input to the northeast along the shoreline. Upon reaching the Apostle Islands archipelago, riverine inputs of nutrients and energy are deflected towards deeper, offshore waters (Anderson et al., 2015).

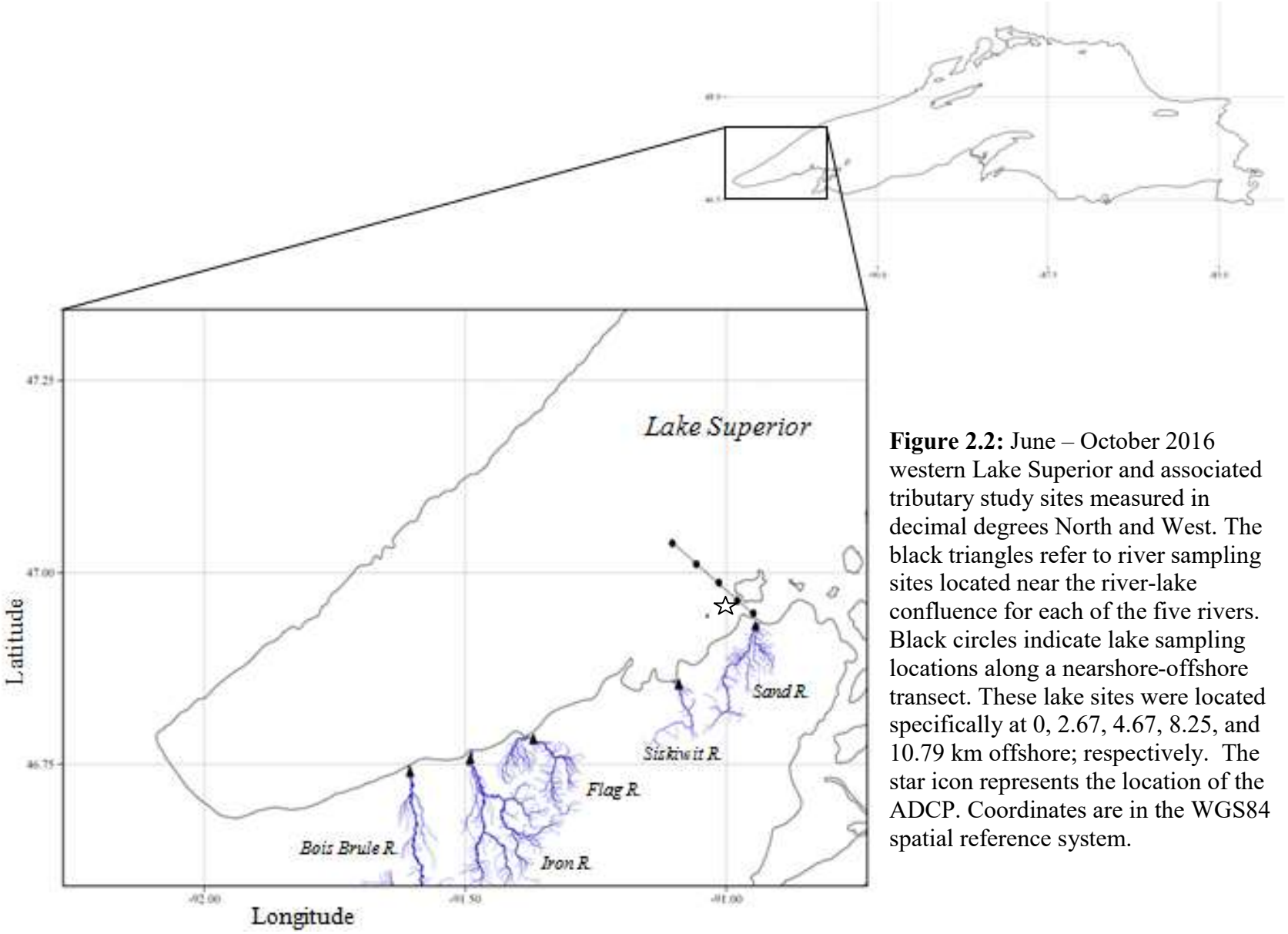

Figure 2.2: June – October 2016 western Lake Superior and associated tributary study sites measured in decimal degrees North and West. The black triangles refer to river sampling sites located near the river-lake confluence for each of the five rivers. Black circles indicate lake sampling locations along a nearshore-offshore transect. These lake sites were located specifically at 0, 2.67, 4.67, 8.25, and 10.79 km offshore; respectively. The star icon represents the location of the ADCP. Coordinates are in the WGS84 spatial reference system.

According to Yurista and Kelly (2009), river water inputs from many of the tributaries that line the shoreline of Lake Superior can be detected between 0.5-2.0 km from shore through the analysis of specific conductivity values. This suggests the impacts of these tributaries could be significant quite a distance from the river-lake interface. However, not every tributary had neighboring identifiable patches in the nearshore zone of Lake Superior. The difference in discharge among tributaries is primarily determined by spatial differences in rainfall and, more importantly, the relative size of the watershed.

The spatial coverage in river and lake sampling in this study served to holistically address the influence a multitude of rivers had on the entire nearshore ecosystem of western Lake Superior following the episodic storm event. The Bois Brule, Iron, Flag, Siskiwit, and Sand Rivers were chosen to quantify nutrient and energy input along the southern shoreline in this region of the lake. These five rivers were among the largest inflowing rivers along the southern shoreline, in terms of watershed and mean discharge.

The area of Lake Superior to be studied was determined based on the hydrodynamic patterns of nearshore zones described by Rao and Schwab (2007), and an analysis of past satellite imagery of river plumes. The location of the nearshore-offshore transect was chosen to assess the nearshore biogeochemical response at the furthest extent of riverine input, as well as whether or not a strong nearshore-offshore metabolic gradient in response develops. The nearshore-offshore transect spanned approximately 11 km, extending from Sand Point towards offshore water. The furthest point offshore was considered as the beginning of offshore waters. Five sampling stations were monitored throughout the 2016 field sampling season along the nearshore-offshore transect. Along each transect, vertical profiles were conducted and water samples were collected at discrete depths. The vertical resolution of the profiles, as well as the

discrete water sample collections are shown in Figure 2.3. The vertical profiles were conducted using a YSI ExoSonde capable of measuring pH, turbidity, specific conductivity, dissolved O_2 (both mg L^{-1} and % saturation), and chlorophyll *a* fluorescence. Prior to each sampling trip, the sonde was calibrated and upon return a post-calibration was performed to account for any drift in sensor measurements. Over the course of the 2016 field season, there was no measurable drift for each sensor.

Table 2.1: Geographic coordinates for each tributary and Lake Superior sampling site; including specific dates of 2016 the site was sampled. The spatial reference system used was WGS84.

	Site	Coordinates	June	July	August	September	October
Rivers							
	Bois Brule	46° 44.177N 91° 36.097W	21	6,15,27	16	22	26
	Iron	48° 44.811N 91° 29.156W	21	6,15,27	16	22	26
	Flag	46° 46.897N 91° 22.351W	21	6,15,27	16	22	26
	Siskiwit	46° 57.262N 91° 05.495W	21	6,15,27	16	22	26
	Sand	46° 57.965N 90° 57.376W	21	6,15,27	16	22	26
Nearshore-Offshore							
	10.79 km	47° 01.426N 91° 03.823W	23	7,20,28	17	21	25
	8.25 km	47° 00.427N 91° 02.705W	23	7,20,28	17	21	25
	4.67 km	46° 58.948N 91° 00.644W	23	7,20,28	17	21	25
	2.67 km	46° 58.346N 90°59.255W	23	7,20,28	17	21	25
	0 km	46° 57.437N 90° 57.650W	23	7,20,28	17	21	25

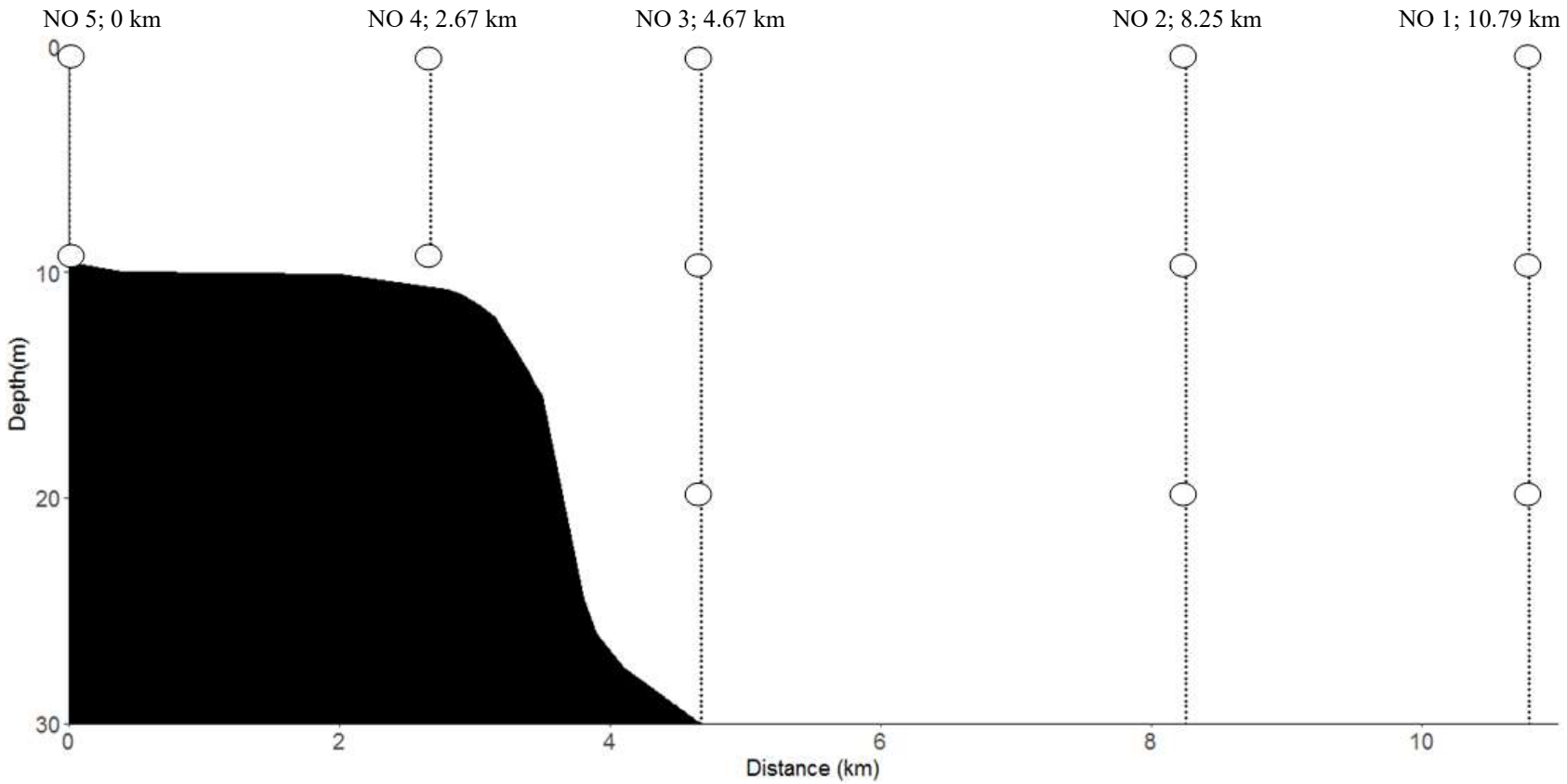

Figure 2.3: Distribution of sonde vertical profiles (0.25 m vertical depth resolution) and discrete water samples (open circles) along the nearshore-offshore transect. The black polygon represents the bottom of the sonde profile along the nearshore-offshore continuum. Each individual depth profile is labeled by site identification and distance offshore. Sites NO 2, NO 3, NO 4, and NO 5 are designated as nearshore Lake Superior, whereas site NO 1 is representative of the beginning of offshore waters.

Horizontal Distribution of River Inflow

Lake hydrodynamic patterns play a critical role in the horizontal distribution of chemical and biological species, and processes. Therefore, knowing where and how much inflowing river water ends up in large lakes is vital to our understanding of how rivers influence these ecosystems. The instantaneous discharge for each of the five rivers was quantified during each sampling trip (see Table 2.1). Discharge was calculated by dividing the river channel into ten contiguous cross sections. Within each subsections, the area was obtained by measuring the width and depth. A flow meter was used to determine instantaneous velocity for each subsection at mid-depth when the depth of the channel was less than 1 m. Two measurements of discharge were taken and averaged if the depth was greater than 1 m. The discharge in each subsection was determined by multiplying the subsection area by the measured velocity. The total, instantaneous discharge was then calculated by summing the discharge of each subsection.

A flow meter (Sigma Sport BC1200) was used to determine instantaneous discharge of each tributary on sampling days. To verify the accuracy of the flow meter, a paired t-test was used to test for differences in discharge of the Bois Brule River between the flow meter and the USGS station for the entire field season. There were no significant differences between the discharges determined by both methods when they were analyzed together ($t_6 = -0.14$, $p = 0.891$). Therefore, the flow meter was an adequate means for quantifying river discharge for all of the rivers sampled.

The discharge of the Bois Brule River was continuously monitored throughout the 2016 field sampling season by the USGS. The discharge of the other four rivers was measured only during sampling trips (see Table 2.1). Due to the inconsistent measurements, indirect discharge estimates were required to fill in the discharge data gaps of the Iron, Flag, Siskiwit, and Sand

Rivers. To obtain continuous discharge data for the Iron, Flag, Siskiwit, and Sand Rivers, the watershed-area ratios between these individual rivers and the Bois Brule River were used following a modified approach of Ries (2007). The equation used to estimate discharge data for the Iron, Flag, Siskiwit, and Sand Rivers is shown below.

$$Q_E = (A_E/A_{Brule}) * Q_{Brule} \quad (1)$$

where Q_E is the estimated discharge, (A_E/A_{Brule}) is the watershed-area ratio between one of the four rivers and the Bois Brule River, and finally, Q_{Brule} is the discharge of the Bois Brule River as determined by the USGS gauge station. To justify the practicality of determining continuous discharge estimates of the Iron, Flag, Siskiwit, and Sand Rivers using this method, a paired t-test was used to test for differences between the discharge estimated using watershed-area ratios and discharge measured using the flow meter. There were no significant differences between the discharges determined by both methods ($t = 0.02$, $p = 0.981$). Therefore, the estimation method using watershed-area ratios was a satisfactory means of quantifying continuous river discharge for the Iron, Flag, Siskiwit, and Sand Rivers.

The relationships between the estimated discharge, based on watershed-area ratios, and measured discharge are shown in Fig. 2.4. Although the relationship is strong, there are some deviations from a 1:1 relationship. This is most likely due to differences in watershed soil type and slope, both of which significantly influence the runoff, and subsequently river discharge to the lake (Ries, 2007). Some variability within the relationship may be due to spatial differences in rainfall over the duration of the storm.

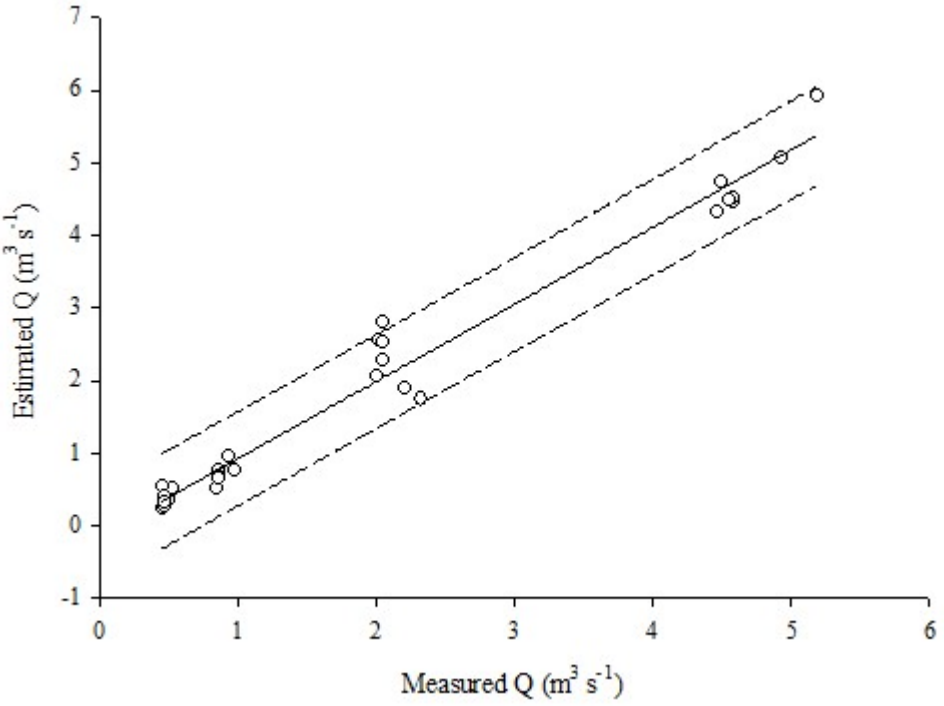

Figure 2.4: Linear relationship between measured discharge and estimated discharge based on watershed-area ratios for all tributaries. The solid black line represents the overall trend of the data set; the correlation coefficient, $r^2 = 0.98$, for the trendline suggests a strong relationship between the measured and estimated discharge. The dotted lines refer to the 95% confidence interval for the data set.

In the western region of Lake Superior, significant riverine plumes are noticeably visible on satellite imagery. As a result of the easily erodible red clay plain that dominates the watershed, these inflows are characterized as very turbid, reddish-brown surface plumes (Stortz et la., 1976; see Fig. 2.1). The distinct differences in water mass color made it possible to use remote sensing to determine surface plume extent and duration. For the purposes of this study, remote sensing was used to provide a time-series visualization of Lake Superior surface dynamics in response to episodic inflow.

MODIS Aqua Level 2 image with 1 km spatial resolution were selected between July 5 (Julian day 187) 2016 and August 16 (Julian day 229) 2016 from NASA's Ocean Color database (https://oceancolor.gsfc.nasa.gov/data/aqua/). More specifically, images were downloaded for the following days, which were largely cloud-free: July 5th, July 12th, July 16th, July 18th, July 25th, and August 16th. Specific swaths were selected, with a zenith angle of 45^{o} or less, pertaining directly to the western region of Lake Superior between 46.5^{o} – 47.75^{o} latitude and 90.25^{o} – 92.25^{o} longitude. For simplicity, Level 2 images were chosen because they had already been atmospherically corrected and geolocated. Mouw et al. (2013) showed that the standard atmospheric correction used by NASA is the best option for Great Lakes imagery. The downloaded MODIS Aqua images were processed and analyzed using R (Version 3.3.1) and QGIS (Version 2.18.9) software.

The distribution of the surface plume was estimated using the remote sensing surface reflectance (R_{rs}) at 645 nm. Turbid water reflects proportionately more light at longer wavelengths, while clearer water reflects less. Therefore, a longer wavelength band such as 555-670 nm provides the greatest distinction between clear, offshore Lake Superior water and highly turbid riverine input. At the edges of this wavelength spectrum, however, there are chlorophyll *a*

reflectance peaks in the blue-green region, as well as the red-near infrared region. For these reasons, R_{rs} 645 nm provides the ideal compromise, permitting the use of satellite imagery to monitor surface plume dispersal with minimal error due to chlorophyll *a* reflectance.

The processing of each individual MODIS Aqua satellite image followed the methods used by Nezlin & DiGiacomo (2005), with some differences. Based on a literature review and personal communication (Brice Grunert, Michigan Technological University), the method used by Nezlin & DiGiacomo (2005) provides the most simplistic approach for the purposes of this project. Using R, the pixels of each resulting image of R_{rs} 645 nm were interpolated on a regular grid of 1 km resolution. Prior to interpolation, the 1 km x 1 km grid was clipped using an ESRI shapefile of the surrounding watershed so as to only interpolate surface reflectance data for the lake surface. To quantitatively estimate plume area over time, the regions containing missing data (likely due to cloud cover) were replaced with estimated R_{rs} 645 nm data obtained by averaging the surrounding grid nodes.

This procedure was repeated until all the grid nodes were devoid of missing data. To interpolate between grid nodes, the resultant grid was interpolated using a bivariate spline interpolation technique performed using R equipped with the "akima" package. The resultant product was then saved as a raster file for import into QGIS for further spatial analysis of plume area and dynamics.

Based on a review of available satellite imagery from 2005 to 2015 (Brenda Moraska Lafrancois and Shania Leask, National Park Service, pers. comm.) and a literature review of Lake Superior current patterns, flow parallel to shore appears to be the predominant current pattern within the nearshore of western Lake Superior. Hydrodynamic modeling conducted by Beletsky et al. (1999) and Bennington et al. (2010) shows counterclockwise current patterns for

the western region of Lake Superior during the summer. Along the southern shoreline, flow in geostrophic equilibrium develops traveling northeast, parallel to the shore. However, Bennington et al. (2010) also highlight the potential for complete reversal in current patterns following episodic storm events. To determine if this average counterclockwise pattern in current persisted during the study periods, vertical current profiles were conducted over the course of the 2016 sampling season through the use of an Acoustic Doppler Current Profiler (SonTek Argonaut® - XR). The ADCP was located close to the western edge of the Apostle Islands archipelago, near the southwestern corner of Sand Island (see Fig. 2.2).

Vertical Distribution of River Inflow

Although satellite imagery can be useful in examining river plumes propagating along the surface, it does not address subsurface riverine intrusions. Intrusions of greater density than recipient lake water plunge beneath the surface and propagate through the water column as density currents. The fate and dispersal of these intrusions depends on several factors, including stratification, the strength of the inflows, and density differences between the inflow and the lake. Following episodic storm events, these inflows may be strong enough to result in significant intrusions stretching far into the lake. Vertical profiles of temperature and specific conductivity were used to address subsurface inflow dynamics.

Electrical conductance normalized to 25^{o}C (EC_{25}) has been shown to be a useful tracer of differing water masses, provided the difference in conductance between them is considerable (George & Jones, 1987; Yurista and Kelly, 2009). For this region of Lake Superior, conductance differences between tributaries and Lake Superior are likely large enough to merit using this tracer technique. Paired t-tests were used to test for differences between the average EC_{25} of

Lake Superior and five tributaries, the Bois Brule, Iron, Flag, Siskiwit, and Sand Rivers. There were significant differences between the EC_{25} of the lake and the tributaries when these five tributaries were analyzed individually ($t_6 = 4.77$, $p = 0.003$; $t_6 = 9.19$, $p = 9.37 \times 10^{-5}$, $t_6 = 13.92$, $p = 8.56 \times 10^{-6}$, $t_6 = 3.04$, $p = 0.023$, $t_6 = 31.04$, $p = 7.43 \times 10^{-8}$; respectively) and together ($t_{34} = 10.69$, $p = 2.08 \times 10^{-12}$).Throughout the sampling period offshore Lake Superior water at 30 m was consistently close to 99 μS cm^{-1}. In comparison, the conductivity for each of the rivers was always well above 120 μS cm^{-1}, averaging around 168 μS cm^{-1}, suggesting that conductivity can provide a useful tracer of subsurface intrusions in western Lake Superior. Upon validation of using EC_{25} as a tracer, binary two-component mixed models, using average Lake Superior and river EC_{25} as endmembers, were determined to estimate the relative proportion of river water present at each depth increment, *Z*, using the following equation:

$$(Z_{EC_{25}} - \overline{Lake_{EC_{25}}}) / (\overline{River_{EC_{25}}} - Z_{EC_{25}}) \quad (2)$$

The greatest advantage of using EC_{25} to trace subsurface river intrusions is in its ability to maximize data resolution while minimizing cost.

Density differences primarily regulate where these intrusions occur. Water temperature and density are directly related. Slight increases in water temperature of Lake Superior result in proportional decreases in water density. Therefore, the depth and strength of stratification plays a critical role in determining the influence river intrusions have on the biogeochemistry of nearshore Lake Superior. This temperature-density relationship allows for the use of temperature profiles as a form of validation of potential riverine input (i.e. spikes in EC_{25}) propagating along gradients of equal density. From the temperature profiles and the river temperature data for each sampling trip, density profiles were calculated with contour lines showing density gradients

certain rivers propagate along using R (Version 3.3.1). For each river and the lake, density corrections were made to account for suspended sediment load following the approach outlined by McCullough et al. (2007).

Although differences in EC_{25} between Lake Superior and surrounding rivers suggests EC_{25} may be the most useful waterbody tracer, turbidity differences within Lake Superior may also be indicative of river subsurface intrusions. The red clay plain of western Lake Superior's watershed results in strong differences in turbidity between the lake (0.31 NTU ± 0.03 NTU, n = 120) and its tributaries (6.65 NTU ± 4.29 NTU, n = 30). Turbidity is a measure of water clarity, more specifically how variable the passage of light through the water column is in response to suspended material concentrations. Vertical profiles of turbidity were conducted at each lake sampling site to examine changes in water column clarity in response to an episodic river plume. Turbidity can often increase dramatically both during and following an episodic storm event. Highly turbid inflow can have a significant impact on recipient ecosystems. Episodic river plumes in western Lake Superior typically introduce an abundance of red clay complexes to the nearshore. These complexes contribute to the turbidity, and play a vital role in regulating the amount of light available to nearshore autotrophic communities.

The turbidity of the western Lake Superior water column is primarily due to suspended solids, either as a result of riverine inflow or lake sediment resuspension. For total suspended solids (TSS; hereafter) analysis, a pre-determined amount of river and lake water samples were filtered through pre-weighed 0.7 μm Whatman GF/F filters. The retentate for each sample was stored in a dessicator until further analysis. In the lab, the retentate was dried at 105^{o}C in an oven for approximately 2 hours to remove as much residual water as possible. The weight of the remaining residue was measured on a microbalance (Sartorius MSE3.6P Cubis Micro Complete

Balance) to the nearest 0.01 of a gram, which was used to determine the mass of TSS per volume of sample.

The relationship between TSS and turbidity for western Lake Superior is shown in Figure 2.5. The strong relationship between TSS and turbidity of Lake Superior and its tributaries suggests turbidity in this region of the lake is mainly due to the TSS load of the inflowing tributaries. Therefore, turbidity may be an indicator of river water presence along a nearshore-offshore transect. An analysis of the turbidity profiles is needed to justify this assessment.

Although the turbidity probe was calibrated prior to each sampling trip, to validate these turbidity profiles, at each lake sampling site the Secchi depth was also recorded. The method to determine Secchi depth followed the protocol set by the EPA and USGS (Green et al., 2015; USEPA 2009). Based on Figure 2.6, increases in average water column turbidity corresponded to decreases in Secchi depth; however, a few data points fall outside the 95% confidence interval. This suggests some variability in the relationship between Secchi depth and turbidity, which is most likely an artifact of human error in the estimation of Secchi depth or the particle size of suspended sediment. Therefore, turbidity profiles were useful in assessing water column clarity on each sampling trip.

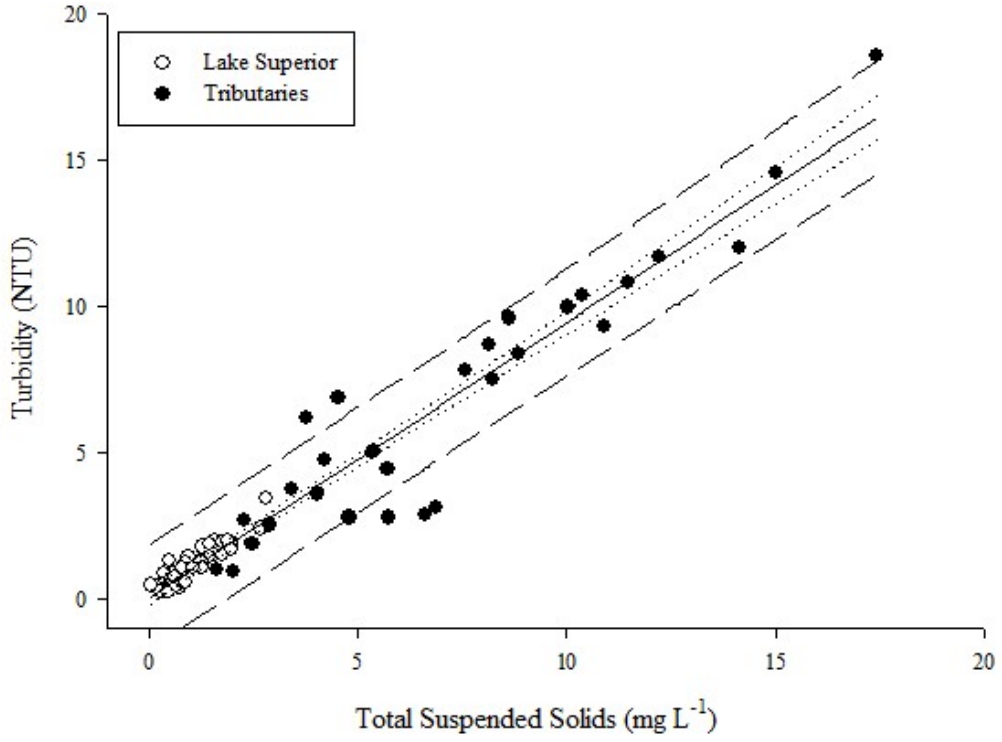

Figure 2.5: Linear relationship between total suspended solids (TSS) and turbidity. The solid black line represents the overall trend of the data set; the correlation coefficient, $r^2 = 0.97$, for the trendline suggests a strong relationship between TSS and turbidity. The dotted lines refer to the 95% confidence interval for the data set, whereas the dashed line represents the 90% confidence interval.

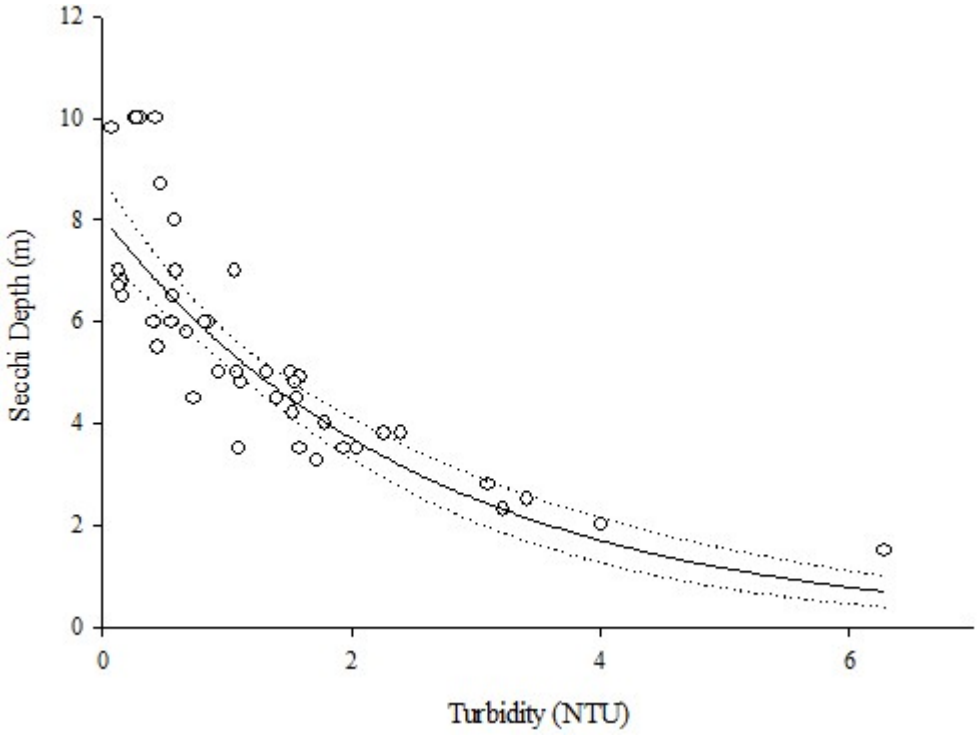

Figure 2.6: Exponential decay relationship between Secchi depth and turbidity. The solid black line represents the overall trend of the data set; the correlation coefficient, $r^2 = 0.88$, for the trendline suggests a strong relationship between Secchi depth and turbidity. The dotted lines refer to the 95% confidence interval for the data set.

Total Phosphorus & Organic Carbon Dynamics

Episodic river inflows typically introduce nutrient and organic carbon-laden water to receiving basins. The differences in density between the two water masses (i.e. river and lake) may effectively create distinct chemical gradients of phosphorus and organic carbon within the water column. These gradients persist until sufficient physical drivers are able to thoroughly mix the two water masses. The entrainment of these inputs to specific depths may drive the distribution of organisms capable of utilizing the nutrient and energy subsidies.

All river water samples were collected for total dissolved phosphorus and dissolved organic carbon using 4 L acid-washed Nalgene® sample bottles. Each of these river water samples was collected at mid-depth near the center of the river. Prior to collection, each of the sample bottles underwent a triplicate rinse of river water to remove any potential contamination and assure that the sample was pure river water. The river discharge data was used to determine the total instantaneous loading of phosphorus and organic carbon to Lake Superior on each sampling day.

To assess the influence rivers have on nearshore chemical dynamics, Lake Superior water samples were collected along the nearshore-offshore transect. Similar to the river samples, these lake water samples were collected for total dissolved phosphorus and dissolved organic carbon. Lake water samples were collected using a 5 L Niskin sampler at the surface, 10 m, and 20 m (when the depth was greater than 10 m), and subsequently transferred to their respective 4 L acid-washed Nalgene® sample bottles. Upon collection both river and lake water samples were stored on ice to slow biological activity until they could be filtered in the lab.

The total phosphorus pools analyzed were total dissolved phosphorus (TDP; hereafter), soluble reactive phosphorus (SRP; hereafter), and particulate phosphorus (PP; hereafter).

Phosphorus is an essential nutrient for organisms in aquatic systems. In Lake Superior, phytoplankton communities are typically phosphorus-limited (Sterner, 2010). Therefore, any influx of phosphorus to the lake may have significant ecological ramifications. These subcategories are essential to understanding phosphorus dynamics in the nearshore zone. The only readily available form of phosphorus phytoplankton can use is orthophosphate. However, certain phytoplankton with the enzyme alkaline phosphatase can break bonds in dissolved organic phosphorus, releasing phosphate which then becomes available for uptake.

For phosphorus, defined water sample volumes were filtered through pre-combusted 0.7µm Whatman GF/F filters. The filtrate was used for the SRP and TDP analysis. Filtrate was saved in 250 mL acid-washed Nalgene® sample bottles. The analysis of SRP and TDP were conducted following the colorimetric methods of Stainton et al. (1977). High intensity UV photo-oxidation converts dissolved organic phosphorus compounds to phosphate, enabling TDP concentrations to be quantified. Therefore, prior to analysis with the molybdate blue method, TDP samples were UV photo-oxidized (La Jolla Scientific Co. UV Photo-oxidation Unit) for 2 hours. The PP filter samples were combusted at 550^{o}C (Thermo Scientific Thermolyne Muffle Furnace) to remove all organic material. Subsequently, 2 mL of 1 N hydrochloric acid (HCl) and 10 mL of de-ionized water was added, and then heated at 105^{o}C for 2 hours to suspend all phosphorus in solution.

All colorimetric determination of phosphorus concentrations were performed on a UV-visible spectrophotometer (Varian Cary 50 Scan).A 10 cm quartz cuvette was used for SRP and TDP analysis, whereas a 1 cm cuvette was used for PP analysis. The absorbance was measured at a wavelength of 885 nm, which is the wavelength of greatest absorption by the antimony-phosphomolydate complex produced using the method described by Stainton et al. (1977).

The total organic carbon pools that were analyzed were as follows: dissolved organic carbon (DOC; hereafter) and particulate organic carbon (POC; hereafter). For DOC, 25 ml of filtered water samples (pre-combusted 0.7 μm Whatman GF/F filters) were transferred to amber glass aliquots for DOC analysis. The 25 ml subsample was acidified to a pH of less than 2 by adding 2-3 drops of1 N hydrochloric acid (HCl). This process transforms all of the dissolved inorganic carbon to CO_2 which can be purged from the sample by carbon-free gas prior to OC analysis. DOC samples were measured using the combustion catalytic oxidation method on a total organic carbon analyzer (Shimadzu Total Organic Carbon 5000 analyzer equipped with an ASI-5000 auto sampler). The TOC analyzer uses an infrared detector to quantify the OC concentration in the sample (after oxidation to CO_2) and has a detection limit of approximately 0.1 mg L^{-1} (Pat Anderson, University of Wisconsin-Milwaukee, pers. comm.).

For POC analysis, defined water sample volumes were filtered through a 0.7μm Whatman GF/F filter. The retentate was placed in a Petri dish and stored in a dessicator until it could be analyzed. Measurements of POC concentrations were performed on an elemental analyzer (Costech Instruments ECS 4010 CHNSO Analyzer). After every 12^{th} sample, an acetanilide control was run to ensure instrument calibration. A standard curve of pre-weighed acetanilide controls was used to convert the millivolt (mV) spikes in CO_2 for each sample to total POC mass. Subsequently, the volume of water sample filtered was used to determine the total POC concentrations.

Spatiotemporal changes in the vertical distribution of dissolved nutrients and organic carbon were compared for all stations along the nearshore – offshore transects to assess whether or not horizontal gradients developed in response to episodic riverine inflow. A three-way ANOVA with depth (i.e. the surface, 10 m, and 20 m), distance offshore, and sampling date as

factors was used to compare mean differences between SRP, TDP, PP, DOC, and POC concentrations. An alpha value of 0.01 was used to reduce the probability of incorrectly rejecting the null hypothesis and, thereby, increase the power of the statistical comparison. Post hoc comparisons were performed using Tukey HSD. All statistical analyses were performed in R (Version 3.3.1).

Phytoplankton Spatial Variability

The spatial distribution of phytoplankton in response to river discharge was determined using vertical profiles and discrete water samples. Vertical profiles of chlorophyll *a* fluorescence (Chl*a*; hereafter) were used to provide increased vertical and horizontal resolution of changes in phytoplankton biomass. Chl*a* has long been used as quick and easy-to-measure surrogate of phytoplankton biomass (Richards and Thompson, 1952; Dillon and Rigler, 1974).However, in some oligotrophic lakes, Chl*a* fluorescence-derived concentrations tend to overestimate total phytoplankton biomass (Kasprzak et al., 2008).

To validate the use of Chl*a* fluorescence profiles, lake water samples were collected at discrete depths along each transect (see Fig. 2.3), and a 400 ml sub-sample was filtered through a 0.7µm Whatman GF/F filter. The filters were then wrapped in aluminum foil and frozen to be stored until analysis. In the lab, the Chl*a* filters were mixed with 10 mL of an extraction solvent (680 mL methanol, 27 mL acetone, and 5 mL DI water) in a centrifuge tube and placed in the freezer for 24 hours, wrapped in aluminum foil to allow for the complete extraction of Chl*a*. After 24 hours, the samples were then spun in a centrifuge (Damon IEC HN-SII) at 3,000 to 4,000 rpm for 5 minutes. Using a pipette, 5 mL of the supernatant from the centrifuge tube was transferred to a quartz fluorometer tube, and analyzed on a calibrated fluorometer (Turner

Designs). Following the initial reading, the sample was acidified with 2 drops of 4 N HCl to correct for any fluorescence due to phaeophytin.

The Chl*a* fluorescence-derived concentration obtained through laboratory analysis were used to verify concentrations determined based on vertical fluorescence profiles. It is important to note that discrete water samples were collected, and vertical profiles performed within an hour of each other during the day (8 – 10 am CDT) for each sampling trip. Values of Chl*a* fluorescence at depths along the vertical profile were matched with corresponding discrete water samples. A simple Deming regression was used to compare the two methods. The regression analysis resulted in a strong positive, linear relationship (Figure 2.7). The strong relationship between laboratory-derived Chl*a* concentration and vertical profile Chl*a* concentration supported the use of vertical profiles to estimate Chl*a* fluorescence-derived concentration within the lake. Temporal variability in mean Chl*a* concentration was values were analyzed using paired t-tests. Again, an alpha value of 0.01 was used to provide more statistical power. All statistical analyses were performed in R (Version 3.3.1).

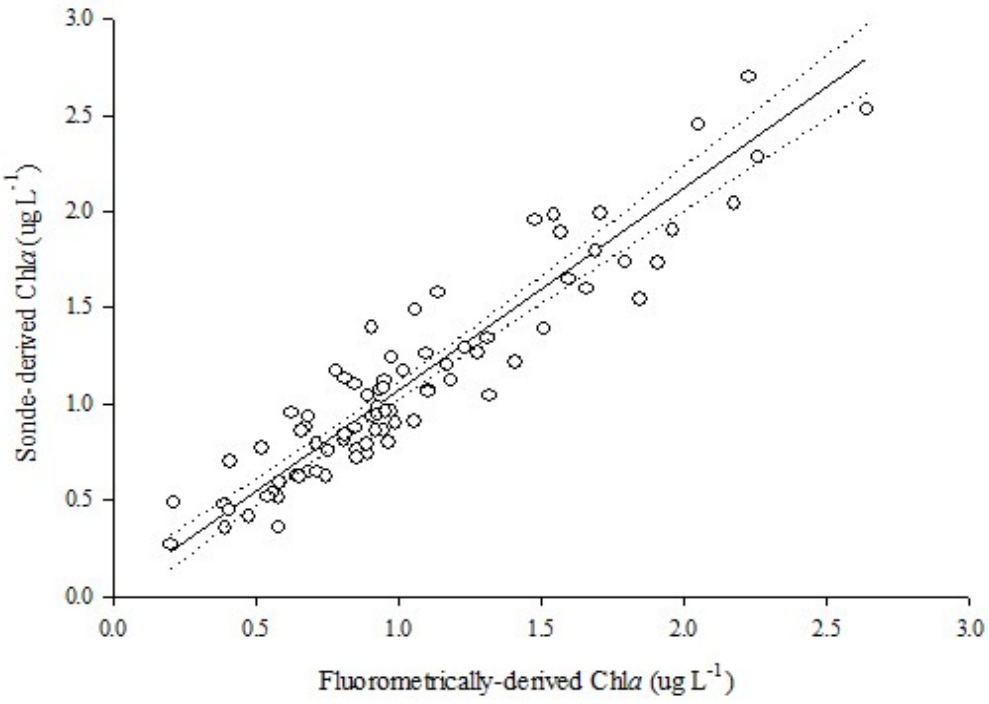

Figure 2.7: Comparison of two different methods for determining chlorophyll *a* (Chl*a*) concentration using a Deming regression. The slope is 1.05; the intercept 0.02; and the correlation coefficient, $r^2 = 0.93$.These results indicate significant correlation between the sonde and fluorometer methods for Chl*a* determination.

Autotrophic primary production and associated phytoplankton growth are dependent on nutrient availability and an optimal light environment. Therefore, understanding the phytoplankton response to episodic river plumes cannot be complete without describing changes in the light environment. Turbidity data of the epilimnion was used to determine variations within the depth of the euphotic zone following a substantial river plume event. The light extinction coefficient, k_T (m^{-1}), was estimated through the following relationship from Brown (1984):

$$k_T = 0.05 * \text{Turbidity (NTU)} \quad (3)$$

A low coefficient was used to avoid overestimating the effect of turbidity. The depth of 1% light penetration is defined as the euphotic zone and can then be related to the light extinction coefficient as such:

$$Z_{\text{euphotic}} = \frac{-\ln(0.01)}{k_T} \rightarrow \frac{4.6}{k_T} \quad (4)$$

Results

Horizontal Distribution of River Inflow

Hydrograph peaks in river discharge were sharp and occurred immediately following the storm event on July 12th (Fig. 2.8). This short lag time between spikes in rainfall and corresponding peaks in discharge suggests the discharge of rivers in this region was extremely sensitive to this episodic rainfall event. Peaks in discharge for each river were approximately 3 times greater than the average baseline conditions (Bois Brule = 15.4 $m^3 s^{-1}$, Iron = 15.8 $m^3 s^{-1}$, Flag = 7.8 $m^3 s^{-1}$, Siskiwit = 3.0 $m^3 s^{-1}$, and Sand = 1.6 $m^3 s^{-1}$; respectively). Each hydrograph had recession limbs less steep than the corresponding rising limb, and returned to baseline flow

conditions about 6 days after the storm event. The magnitude of discharge from each river in response to the July 12, 2016 storm event suggests the influence of river inflow on nearshore Lake Superior may be uncharacteristically stronger than usual following the storm event.

The optical properties of the lake surface of western Lake Superior changed substantially following the major storm event. A surface plume developed along the southern shoreline of western Lake Superior following the July 12, 2016 storm event. During the subsequent days, the plume was transformed by in-lake mixing and eventually dissipated. Fig.2.9 illustrates a time-lapse depiction of the surface plume dynamics from July 12th to August 16th of 2016.

Immediately following the major storm event on July 12th the plume covered approximately 352 km^2. On July 16th, only four days later, the surface plume increased substantially to cover over 2,736 km^2, and encompassed the entire nearshore area along the southern shoreline of western Lake Superior. Along the surface, the plume spread horizontally to reach its greatest extent, over 12 km offshore (Fig. 2.9; B). At this time, the surface plume had also begun to move through the Apostle Islands archipelago. Over the next week, the plume decreased slightly in total area (2,470 km^2), and developed a counterclockwise gyre in proximity to the Duluth-Superior harbor (Fig. 2.9; C). On July 18^{th,} the plume extended further into the Apostle Islands archipelago, and even reached Outer Island (i.e. the furthest island offshore). About two weeks after the storm event, the surface plume had begun to recede, and decreased in total area to approximately 1,944 km^2. By July 25th, the plume had traveled entirely through the Apostle Islands and was now visible to the east of Madeline Island (i.e. the furthest island to the east). Finally, about a month later on August 16th, the surface plume had all but dissipated, and the plume boundary could no longer be discerned through the use of R_{rs}645 nm.

Beletsky et al. (1999) and Bennington et al. (2010) used hydrodynamic modeling to describe the general circulation pattern of western Lake Superior during the summer months. Based on these models, general circulation patterns in this region are typically counterclockwise, and travel northeastward along the southern shoreline towards the Apostle Islands archipelago. Figure 2.10 illustrates a pattern in measured nearshore circulation during the present study similar to that observed by Beletsky et al. (1999) and Bennington et al. (2010). Between June 8 and July 30, 2016 mean current patterns typically flowed to the northeast, and parallel to the adjacent shoreline. During this period, mean current traveled to the northeast 41 days out of the total 54 days. Along the southern shoreline of western Lake Superior, mean current peaked at the surface (17.2 cm s^{-1}) and decreased accordingly as depth increased (2 m = 10.3 cm s^{-1}; 3 m = 9.7 cm s^{-1}; 4 m = 9.0 cm s^{-1}; 5 m = 8.6 cm s^{-1}; 6 m = 8.3 cm s^{-1}; 7 m = 7.7 cm s^{-1}; 8 m = 7.2 cm s^{-1}; 9 m = 6.3 cm s^{-1}). Currents in this region, however, were bimodal suggesting they were strongly influenced by changes in wind patterns. Variability over daily and hourly time scales existed, and all current roses (Fig. 2.10) exhibited some spread in velocity and direction. Following the storm event on July 12th, current velocity increased by about 2 cm s^{-1} at each depth in comparison to the long-term average and traveled parallel to the shore towards the Apostle Islands for approximately 2 weeks until wind shifts resulted in changes in current direction. This suggests either episodic winds during the storm transferred increased momentum to the lake or the storm surge of river inflow influenced the nearshore current.

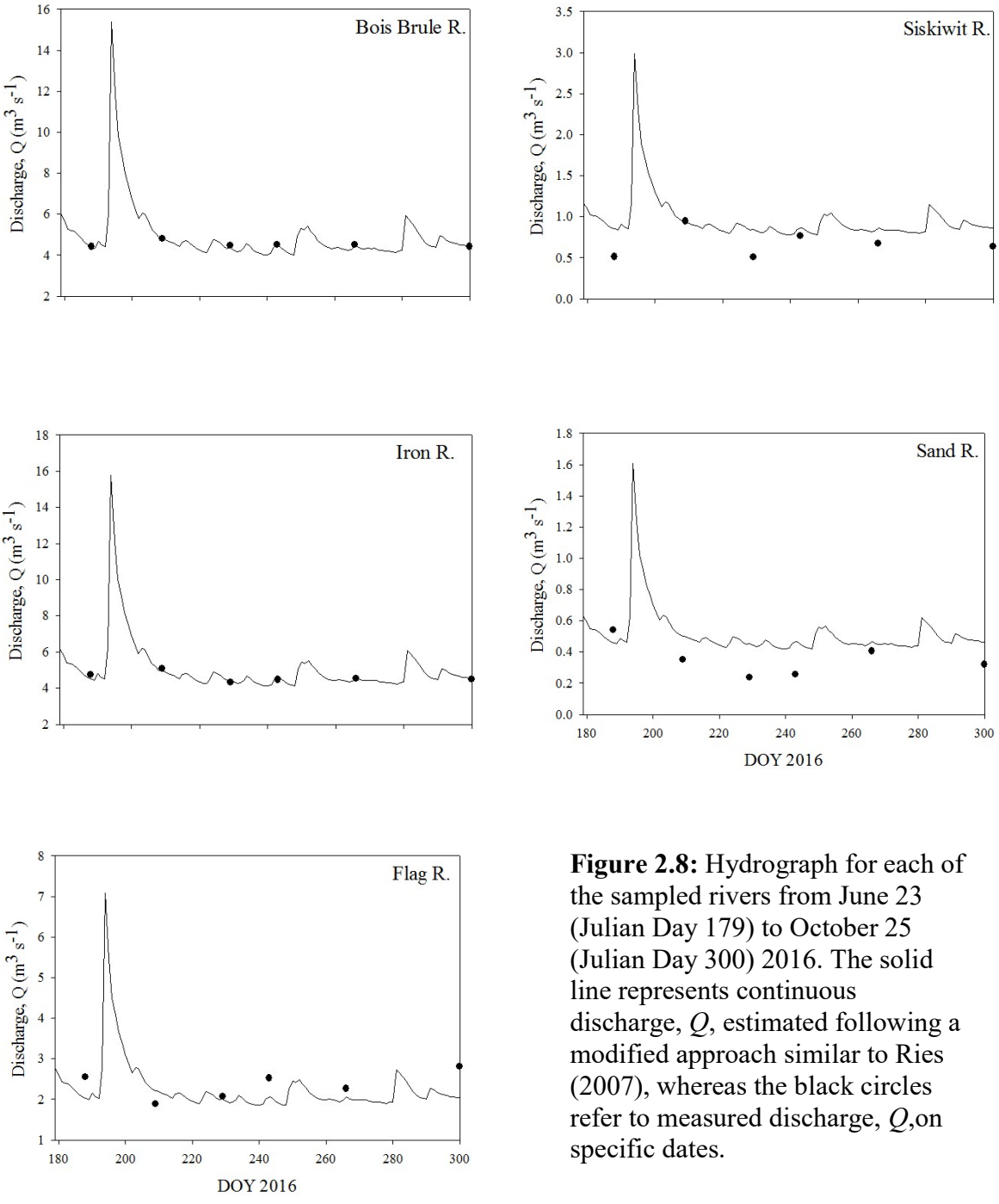

Figure 2.8: Hydrograph for each of the sampled rivers from June 23 (Julian Day 179) to October 25 (Julian Day 300) 2016. The solid line represents continuous discharge, *Q*, estimated following a modified approach similar to Ries (2007), whereas the black circles refer to measured discharge, *Q*,on specific dates.

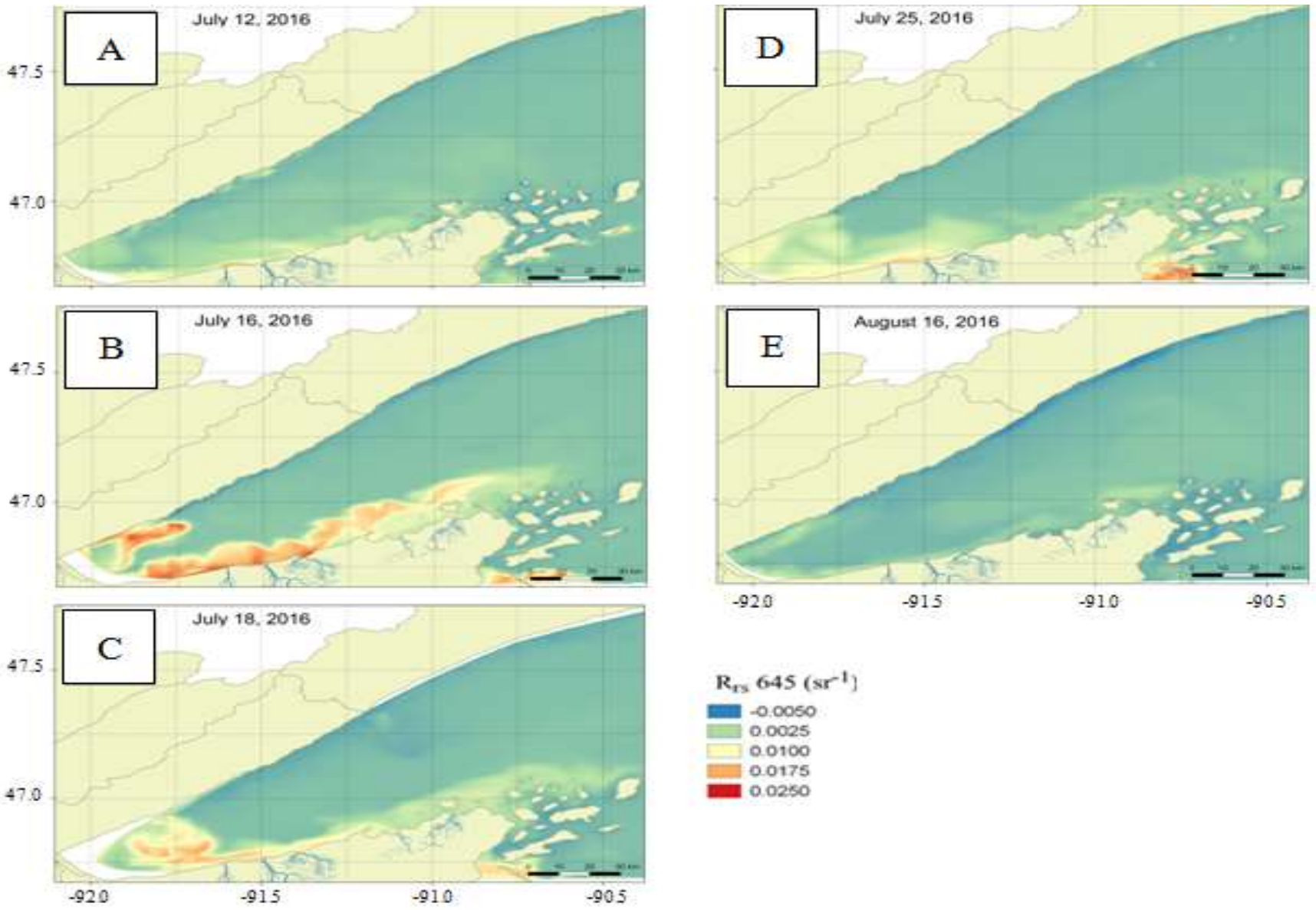
A
July 12, 2016
B
July 16, 2016
C
July 18, 2016
D
July 25, 2016
E
August 16, 2016
47.5
47.0
-92.0
-91.5
-91.0
-90.5
R_{rs} 645 (sr^{-1})
-0.0050
0.0025
0.0100
0.0175
0.0250

Figure 2.9: Time-lapse R_{rs} 645 nm images of an episodic, surface plume developing as a result of a major storm event that occurred on July 12th; (A) July 12th, (B) July 16th, (C) July 18th, (D) July 25th, and (E) August 16th, which was about a month after the storm. The location of the five rivers monitored over the course of the 2016 field sampling season area shown along the southern shoreline. Spatial extent of the plume was measured in decimal degrees North and West. Each image was rectified using the WGS84 spatial reference system.

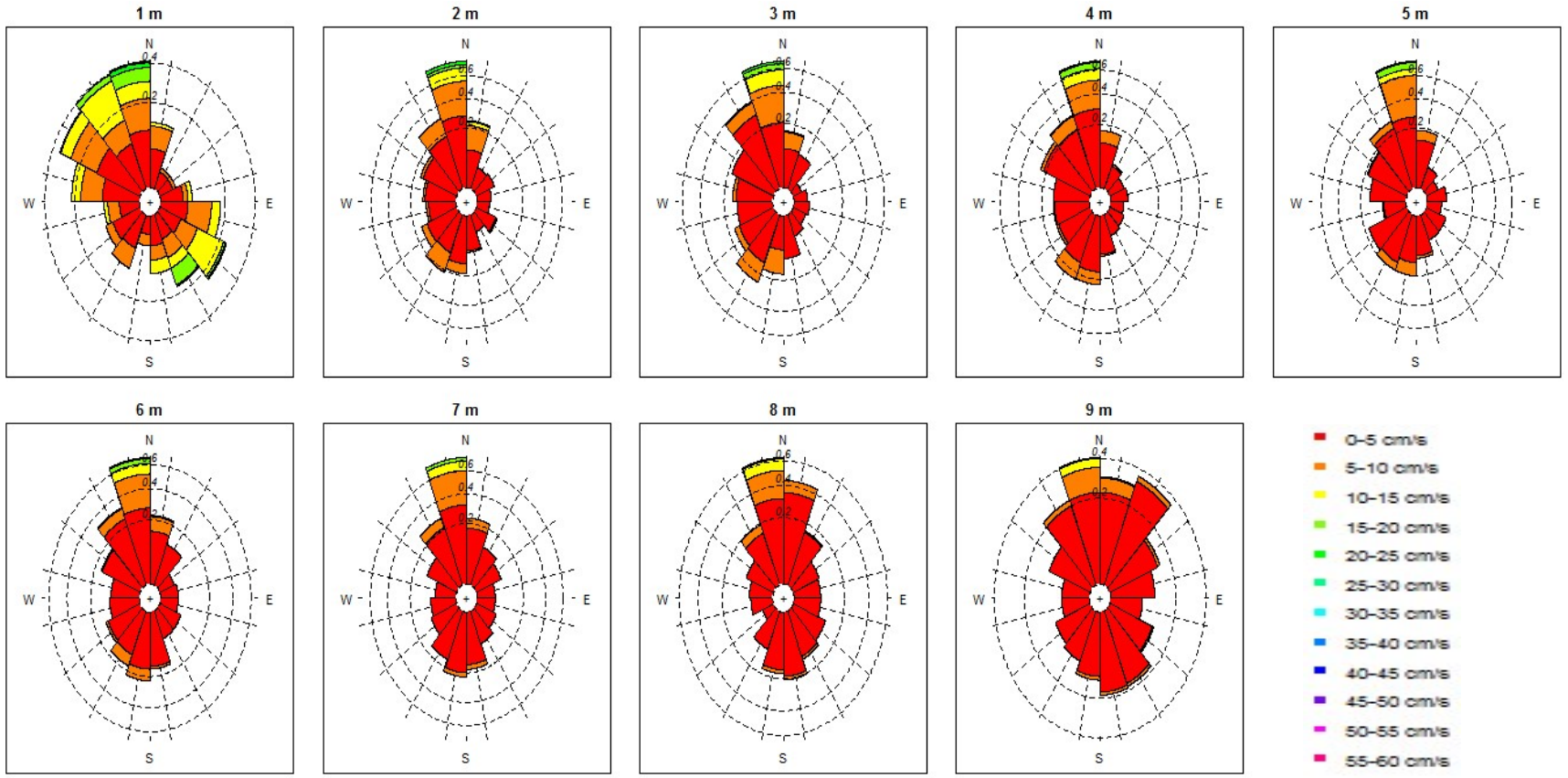

Figure 2.10: Depth-incremented horizontal current velocities and directionality, measured with a 0.75 MHz ADCP over the 2016 field sampling season. Each current rose plot corresponds to discrete depths (between 1 to 9 m) within the water column. Bar direction indicates the direction towards which current flows. The overall length of each bar represents the total number of days (June 8 – July 30, 2016) that average flow was in that direction. Color of the bar indicates the current velocity. Current in one direction may have many colors, indicating the total number of days that average flow was both in that direction and with that velocity. The ADCP was deployed at 10 m in depth near the southwestern corner of Sand Island, Apostle Islands, WI from June – August 2016. Specific coordinates (WGS84) for the ADCP location are as follows: 46^{o} 58.346 N; 90^{o} 59.255 W.

Vertical Distribution of River Inflow

Using temperature, EC_{25}, turbidity, and density profiles, the distribution of subsurface riverine intrusions were illustrated through time in Figures 2.3-4 to 2.3-9. On June 23, 2016 (Fig. 2.11), the water column along the nearshore-offshore transect was relatively homogenous with regard to temperature, EC_{25}, turbidity, and density (7.5 ^{o}C ± 1.4 ^{o}C, 99.3 µS cm^{-1} ± 0.08 µS cm^{-1}, 0.5 NTU ± 0.3 NTU, 999.9 kg m^{-3} ± 0.08 kg m^{-3}, n = 278; respectively). At this time, thermal stratification had yet to set in. The upper reaches of the water column had begun to warm, however. This is illustrated by the slightly higher temperatures in the upper 10 – 12 m (8.9 ^{o}C ± 0.8 ^{o}C) in comparison to deeper, offshore water (6.4 ^{o}C ± 0.7 ^{o}C).The water column was also denser (999.9 kg m^{-3} ± 0.1 kg m^{-3}) in comparison to the sampled tributaries (998.6 kg m^{-3} ± 0.4 kg m^{-3}) suggesting any significant riverine inflow would be constrained primarily to the surface of the lake (Fig. 2.11; D). Despite the potential for river inflow to propagate along the surface, the lack of spikes in EC_{25} and turbidity implies that no substantial river inflow had reached the Apostle Islands archipelago.

About two weeks later on July 7, 2016 (Fig. 2.12), the beginning of thermal stratification set in, and a weak thermocline began to develop around 5 m. In terms of EC_{25} and turbidity, the water column was still relatively constant, albeit with a slight increase in turbidity at the sites closest to shore. Between 0 and 2.67 km offshore, turbidity (1.78 NTU ± 0.2 NTU) approximately doubled that of offshore waters (0.75 NTU ± 0.2 NTU). Since there was not an accompanying spike in EC_{25}, the rise in water column turbidity within this area may have resulted from a minor, sediment resuspension event rather than riverine inflow. The density profile mirrored that of temperature; warmer, less dense water was situated near the surface and denser water within the hypolimnion. Although there was no significant riverine inflow as shown

by the EC_{25} profile, horizontal density gradients developed where dense (>998.4 kg m^{-3}) river intrusions, such as the Flag (999.3 kg m^{-3}) and Siskiwit Rivers (998.6 kg m^{-3}) could have potentially propagated along. This was one week prior to the major storm event.

On July 28, 2016 (Fig. 2.13), two weeks after the major storm event, stratification had become a little deeper (between 6 – 8 m) and subsurface river intrusions were clearly visible. The EC_{25} of the entire nearshore and the upper 15 m of the water column offshore were elevated, greater than 102.8 µS cm^{-1} (Fig. 2.13; C) suggesting substantial river inflow both at the surface and within the epilimnion. The greatest spikes in EC_{25} (110.6 µS cm^{-1} ± 2.5µS cm^{-1}) occurred along the thermocline. The density profile (Fig. 2.13; D) illustrates the horizontal density gradient and the pycnocline that the Flag (999.2 kg m^{-3}), Sand (998.9 kg m^{-3}), and Siskiwit Rivers (998.9 kg m^{-3}) traversed along. The magnitude of the EC_{25} spikes were variable along the nearshore-offshore transect, which suggests the presence of several neutrally buoyant inflowing rivers. Close to the shoreline, spikes in EC_{25} (109.9 µS cm^{-1}± 1.2 µS cm^{-1}) were apparent between 4 – 7 m. At 4 km offshore, EC_{25} increased substantially (112.6 µS cm^{-1}± 2.7 µS cm^{-1}) between 6 – 9 m in comparison to the rest of the water column. Additionally, river presence was evident between 9 – 11 m over 10 km from shore.

Turbidity profiles (Fig. 2.13; B) also corroborated the appearance of significant riverine intrusions as shown in EC_{25} profiles. Prior to the appearance of subsurface riverine intrusions, turbidity of Lake Superior typically averaged 0.5 NTU ± 0.3 NTU. On July 28th, the epilimnion, which extended to around 10 m in depth, showed decreased water clarity (1.82 NTU ± 0.8 NTU) relative to typical Lake Superior turbidity. The turbidity within entire water column between 0 and 2.67 km offshore rose dramatically to 2.37 NTU ± 0.7 NTU. Although the entire water column between 0 and 2.67 km offshore became much more turbid, spikes in turbidity further

offshore (2.21 NTU ± 0.8 NTU) appear relatively confined to the surface (between 1 – 3 m).The apparent disconnect between spikes in EC_{25} (at the metalimnion) and turbidity (at the surface) suggests the presence of multiple inflowing rivers with differing buoyancies and suspended sediment loads. The distribution of horizontal density gradients of equal density to that of select tributaries validates this assumption (Fig. 2.13; D). Along the surface, less dense rivers such as the Bois Brule (997.9 kg m^{-3}), Iron (997.8 kg m^{-3}), and St. Louis (997.2 kg m^{-3}) propagate horizontally across the lake.

On August 17, 2016 (Fig. 2.14) about a month after the storm event, subsurface remnants of river intrusions were still present. At this time, stratification had completely set in and the thermocline had become established around 10 – 20 m. Within the epilimnion, EC_{25} was still elevated (104.7 µS cm^{-1}± 1.9 µS cm^{-1}). Spikes in EC_{25} were still apparent along the thermocline, although the magnitude had diminished (109.6µS cm^{-1}± 2.3 µS cm^{-1}), particularly between 0 and 2.67 km offshore. Again, vertical density profiles attribute spikes in EC_{25} along the thermocline to dense, subsurface river inflow. The calculated density for the Bois Brule (998.6 kg m^{-3}), Flag (999.4 kg m^{-3}), Siskiwit (998.9 kg m^{-3}), and Sand (999.1 kg m^{-3}) Rivers suggests remnants from these rivers achieve neutral buoyancy near the thermocline. The horizontal dispersal of river intrusions along the thermocline was also validated by accompanying decreases in water clarity (Fig. 2.14; B). Areas along the nearshore-offshore transect with high EC_{25} show associated spikes in turbidity (2.38 NTU ± 1.1 NTU).

About a month later (Fig. 2.15) thermal stratification had begun to break down and remnants of the initial river intrusions were still present along the thermocline. Along the thermocline, EC_{25} remained slightly higher (103.3 µS cm^{-1}± 0.5 µS cm^{-1}) in comparison to the rest of the Lake Superior water column (99.3 µS cm^{-1} ± 0.08 µS cm^{-1}; Fig. 2.15; C). By now

much of the original river input had dissipated and thoroughly mixed with ambient Lake Superior water. The water clarity in this region had returned to pre-episodic inflow conditions (Fig. 2.15; B). The turbidity for the entire profiled area averaged 0.42 NTU (± 0.2 NTU, n = 434) suggesting most of the suspended solid load introduced by the rivers had either settled out of the water column or been advected and diffused throughout the lake.

In October, thermal stratification had completely broken down, and the water column had become relatively isothermal with a mean temperature of 9.8 ^{o}C ± 0.5 ^{o}C (Fig. 2.16; A). The isothermic conditions of the water column resulted in the density of this region of Lake Superior remaining relatively constant (999.7 kg m^{-3} ± 0.03 kg m^{-3}; Fig. 2.16; D). The dense ambient water of Lake Superior suggests any significant riverine input would be constrained to the lake surface. The St. Louis, Bois Brule, Iron, Flag, Siskiwit, and Sand Rivers are all warmer than the lake at this time, and therefore, less dense. The ubiquitous EC_{25} (99.3µS cm^{-1} ± 0.2µS cm^{-1}) and turbidity (0.43 NTU ± 0.2 NTU) vertical profiles suggests very little to no significant river influence on the nearshore zone.

Spatiotemporal changes in subsurface river intrusions were further described by the variability in the relative proportion of river water within Lake Superior (Fig. 2.17). On June 23rd, the presence of river water within this area of Lake Superior was minimal, and accounted for only 0.39% ± 0.3% of the total volume. About two weeks later on July 7th, approximately 0.54% ± 0.29% of water along the nearshore-offshore transect was of riverine origin. Prior to the major storm event, the water column was relatively homogenous. Two weeks following the storm event, river water accounted for a significantly greater percentage of the total water volume (4.2% ± 3.2% on July 28th). The surface mixed layer contained a large proportion of river water in comparison to the hypolimnion (5.6% ± 3.4% and 0.63% ± 0.2%; respectively).

Spikes in river water were prevalent along the thermocline between 0 – 10.79 km offshore (12.3% ± 3.8%). On August 17th, about a month after the initial storm event, the surface mixed layer still contained a large proportion of riverine water (4.4% ± 3.7%), and water of riverine origin made up a relatively large proportion of the total volume along the thermocline (12.6% ± 2.8%). In September, the mean proportion of river water began to decrease (1.8% ± 1.6%), although remnants were still present along the thermocline (7.0% ± 0.7%). Finally, on October 25th, Lake Superior returned to pre-storm conditions. At this time, river water contributed very little to the water column (0.4% ± 0.2%).

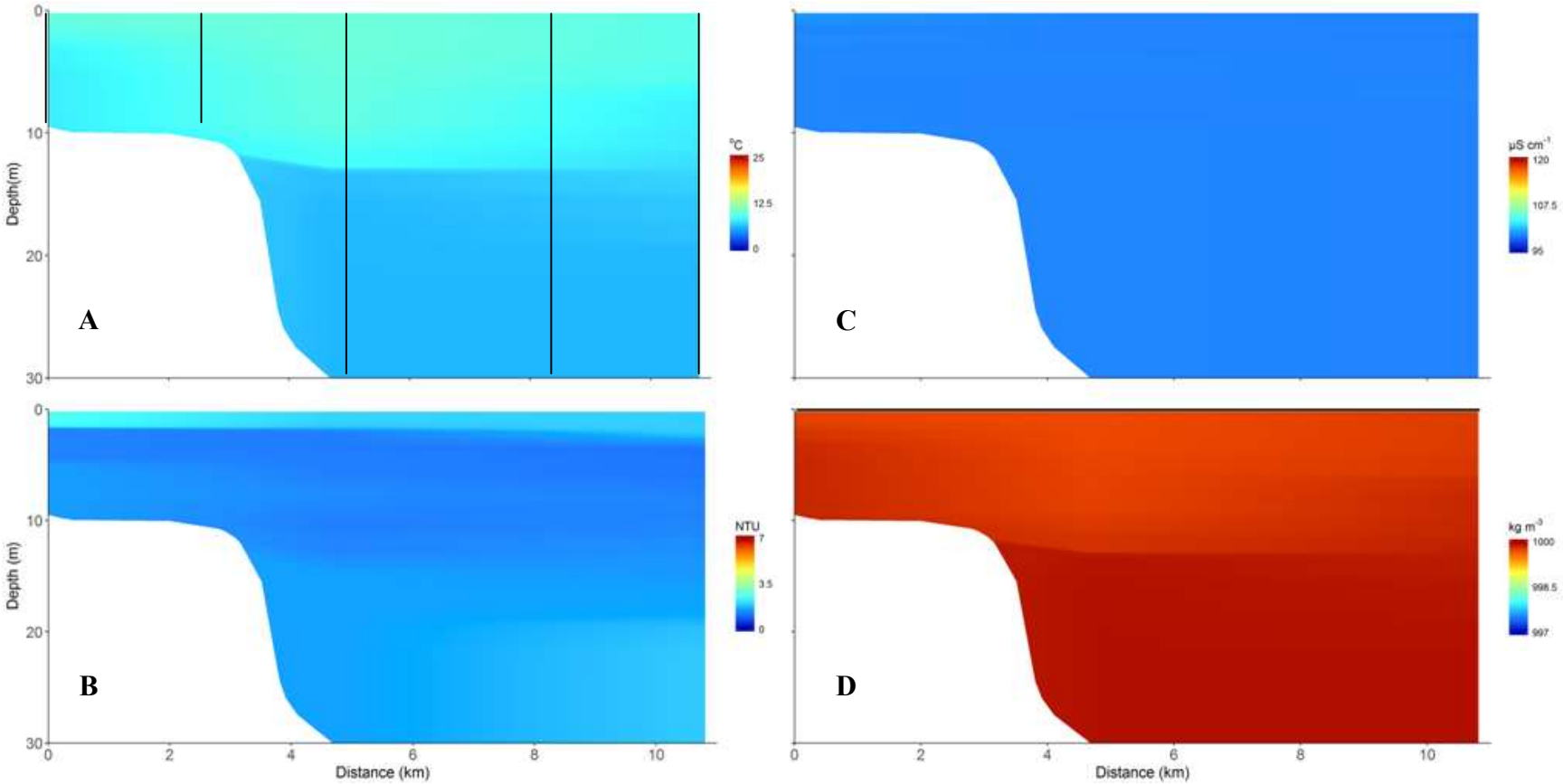

Figure 2.11: Vertical structure of (A) temperature (^{o}C), (B) turbidity (NTU), (C) EC_{25} (µS cm^{-1}), and (D) density (kg m^{-3}) on June 23, 2016. The horizontal density gradients of Lake Superior equal to the density of specific study rivers are illustrated by the solid black line in panel D. The horizontal axis is expressed as distance along the nearshore-offshore transect to the southwest of the Apostle Islands archipelago. The vertical black lines represent the location of vertical sonde profiles.

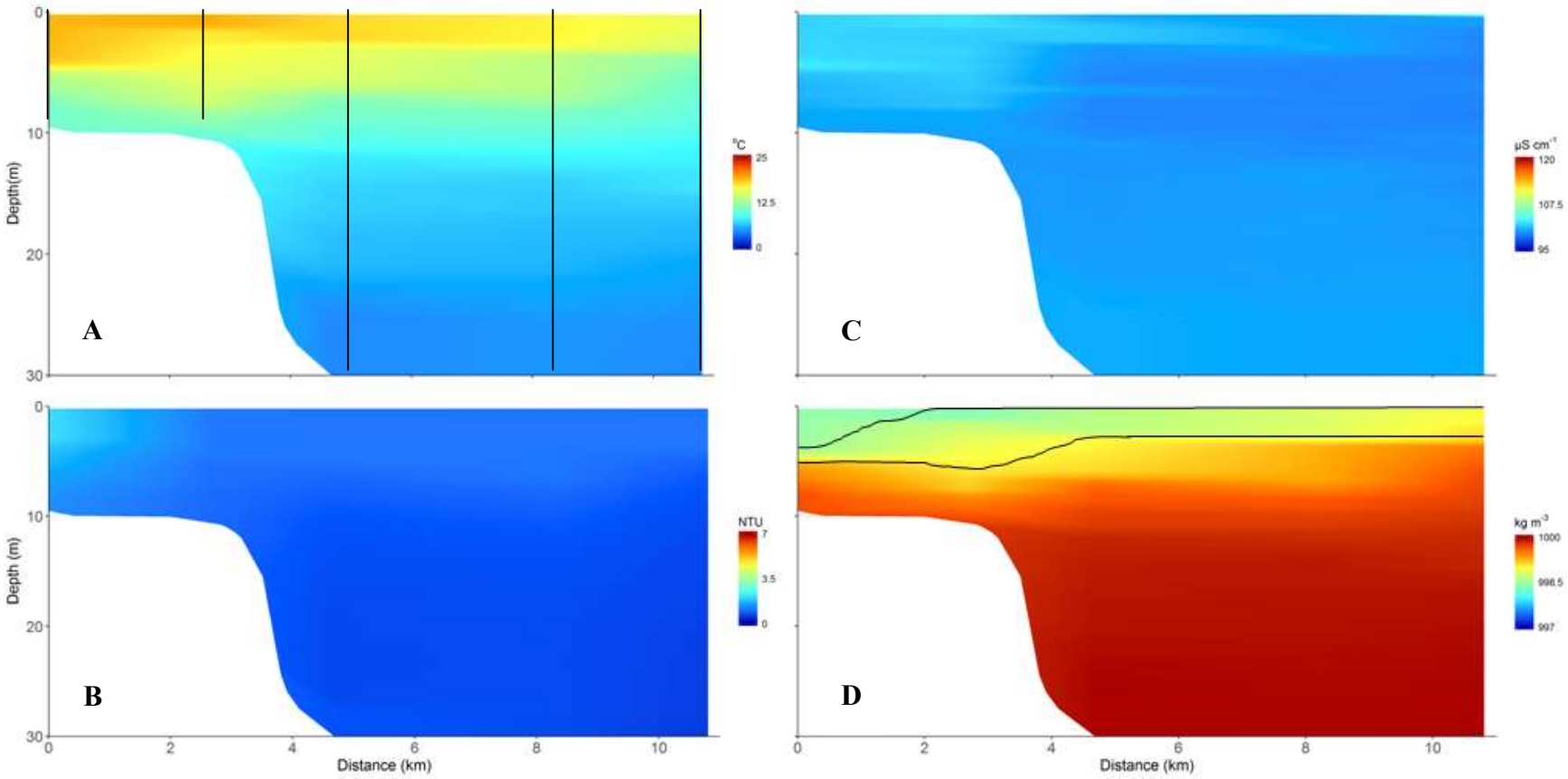

Figure 2.12: Vertical structure of (A) temperature (°C), (B) turbidity (NTU), (C) EC_{25} (μS cm^{-1}), and (D) density (kg m^{-3}) on July 7, 2016. The horizontal density gradients of Lake Superior equal to the density of specific study rivers are illustrated by the solid black lines in panel D. The horizontal axis is expressed as distance along the nearshore-offshore transect to the southwest of the Apostle Islands archipelago. The vertical black lines represent the location of vertical sonde profiles.

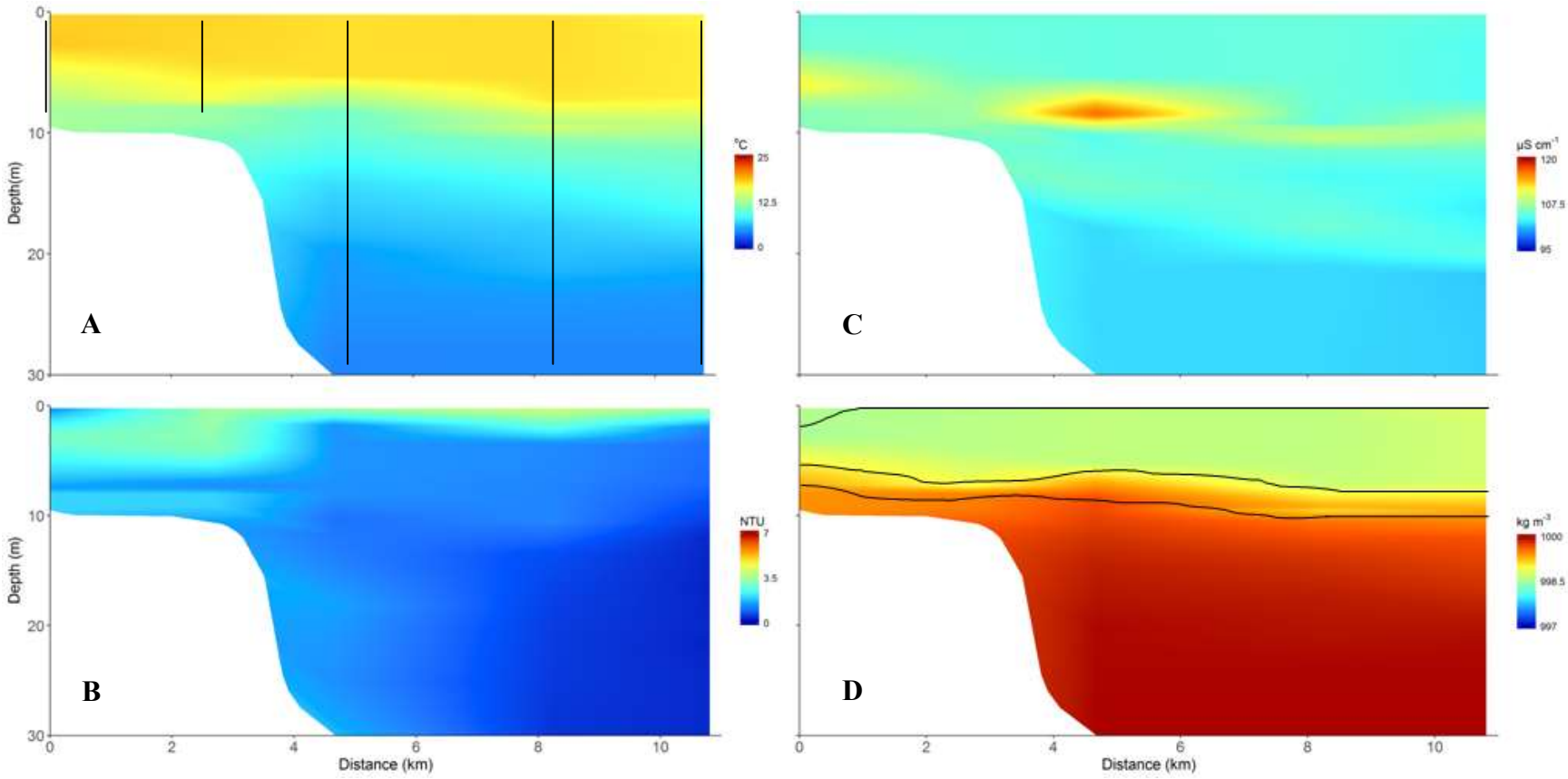

Figure 2.13: Vertical structure of (A) temperature (^{o}C), (B) turbidity (NTU), (C) EC_{25} (µS cm^{-1}), and (D) density (kg m^{-3}) on July 28, 2016. The horizontal density gradients of Lake Superior equal to the density of specific study rivers are illustrated by the solid black lines in panel D. The horizontal axis is expressed as distance along the nearshore-offshore transect to the southwest of the Apostle Islands archipelago. The vertical black lines represent the location of vertical sonde profiles.

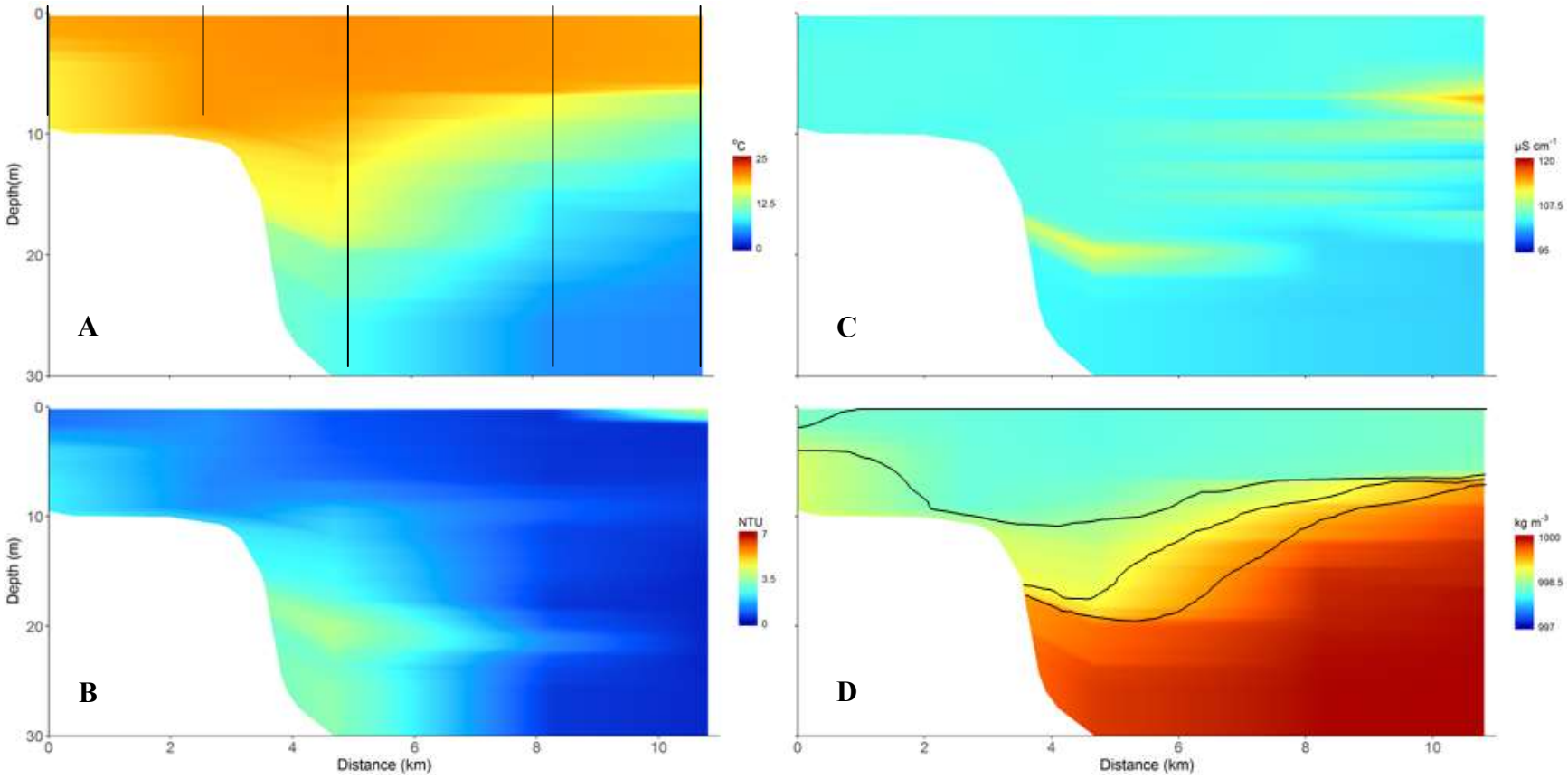

Figure 2.14: Vertical structure of (A) temperature (^{o}C), (B) turbidity (NTU), (C) EC_{25} (µS cm^{-1}), and (D) density (kg m^{-3}) on August 17, 2016. The horizontal density gradients of Lake Superior equal to the density of specific study rivers are illustrated by the solid black lines in panel D. The horizontal axis is expressed as distance along the nearshore-offshore transect to the southwest of the Apostle Islands archipelago. The vertical black lines represent the location of vertical sonde profiles.

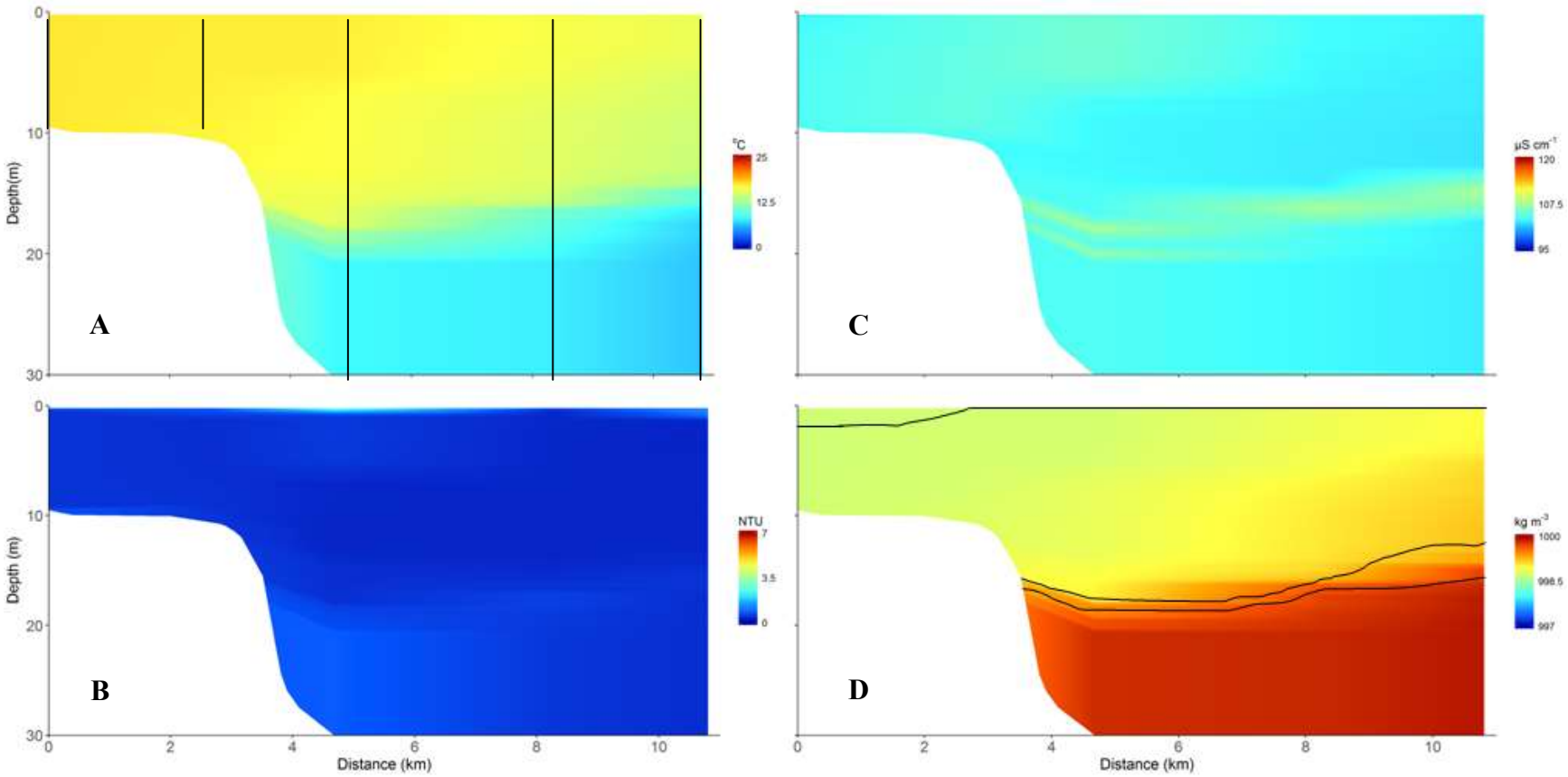

Figure 2.15: Vertical structure of (A) temperature (^{o}C), (B) turbidity (NTU), (C) EC_{25} (µS cm^{-1}), and (D) density (kg m^{-3}) on September 21, 2016. The horizontal density gradients of Lake Superior equal to the density of specific study rivers are illustrated by the solid black lines in panel D. The horizontal axis is expressed as distance along the nearshore-offshore transect to the southwest of the Apostle Islands archipelago. The vertical black lines represent the location of vertical sonde profiles.

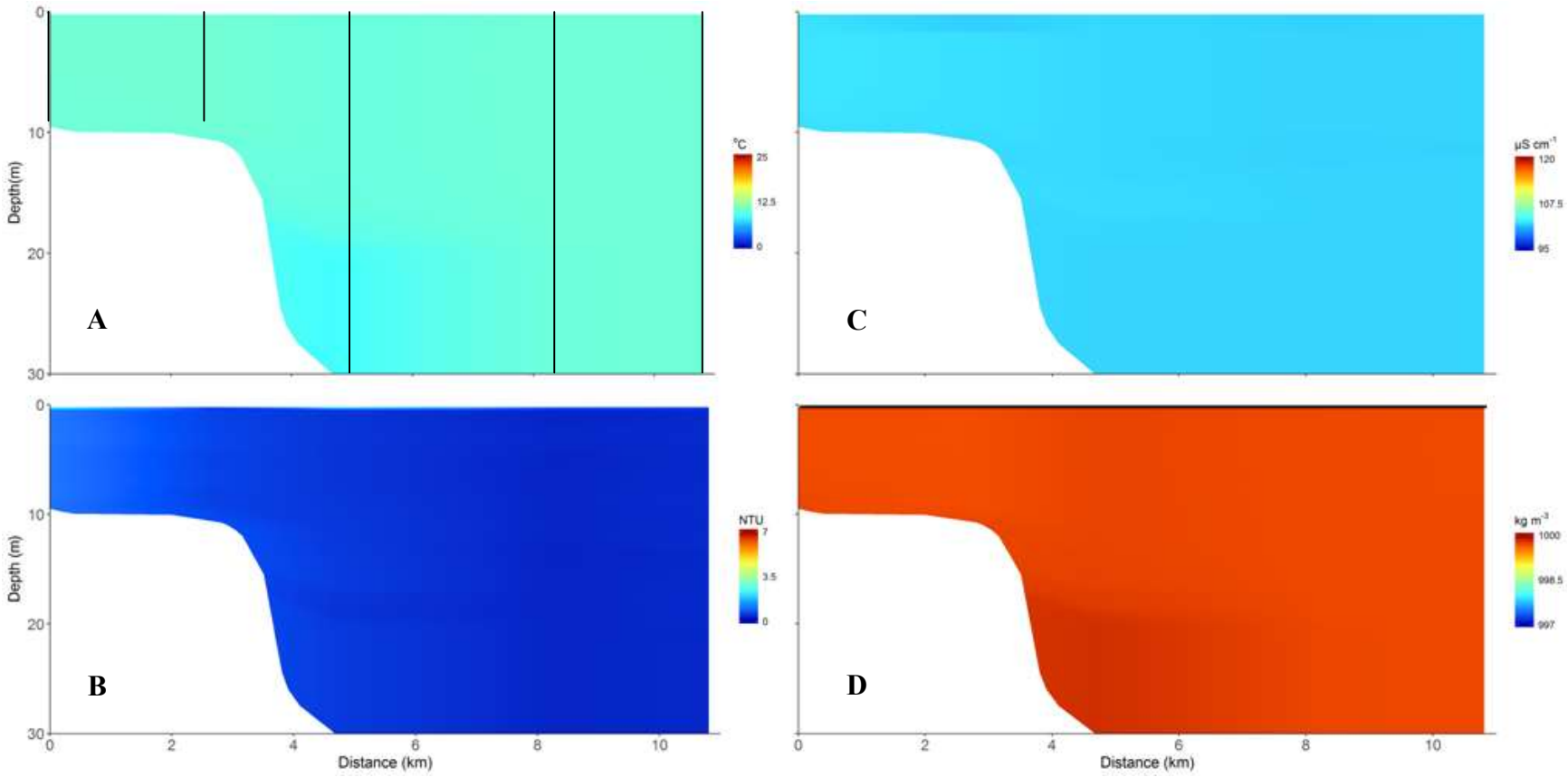

Figure 2.16: Vertical structure of (A) temperature (^{o}C), (B) turbidity (NTU), (C) EC_{25} (µS cm^{-1}), and (D) density (kg m^{-3}) on October 25, 2016. The horizontal density gradients of Lake Superior equal to the density of specific study rivers are illustrated by the solid black line in panel D. The horizontal axis is expressed as distance along the nearshore-offshore transect to the southwest of the Apostle Islands archipelago. The vertical black lines represent the location of vertical sonde profiles.

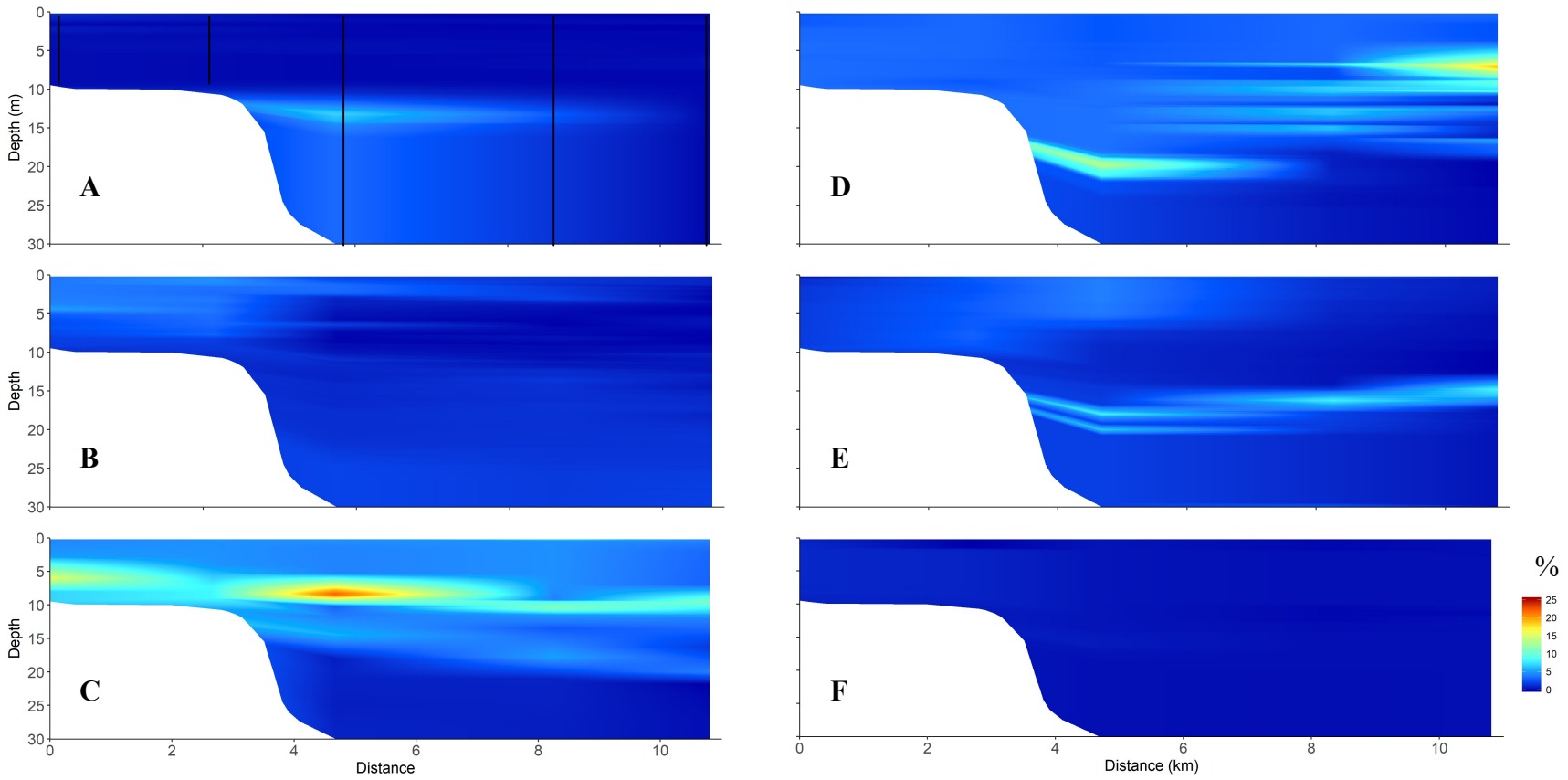

Figure 2.17: Two component binary mixing model illustrating the relative proportion of river water within the water column along a nearshore-offshore transect. Mean offshore, hypolimnetic EC_{25} and mean river EC_{25} were used as the two endmembers for calculating the proportion of river to lake water. Each plot represents a specific date: (A) June 23, (B) July 7, (C) July 28, (D) August 17, (E) September 21, and (F) October 25. The vertical black lines represent the location of vertical sonde profiles.

Total Phosphorus & Organic Carbon Dynamics

Following the major storm event, daily tributary loadings of total phosphorus and organic carbon increased substantially on July 15th. Table 2.2 illustrates the loadings for the Bois Brule, Iron, Flag, Siskiwit, and Sand Rivers over the course of the 2016 field sampling season. On July 15th, the daily SRP loading almost doubled for the Bois Brule (4.9 kg day^{-1}), Iron (7.5 kg day^{-1}), Flag (3.2 kg day^{-1}), Siskiwit (2.2 kg day^{-1}), and Sand (0.3 kg day^{-1}) Rivers, and returned to baseflow conditions approximately two weeks later. A similar pattern emerged for daily TDP loadings of each river (Brule: 7.5 kg day^{-1}, Iron: 11.9kg day^{-1}, Flag: 4.4kg day^{-1}, Siskiwit: 3.8 kg day^{-1}, Sand: 0.5 kg day^{-1}). The loading of SRP on July 15th accounted for approximately two-thirds of the TDP load in each individual river, which suggests a large fraction of TDP loading was available for all phytoplankton. For each tributary, the magnitude of the increase in PP loading following the storm event was larger relative to that of SRP and TDP (Brule: 22.8 kg day^{-1}, Iron: 37.3 kg day^{-1}, Flag: 10.5 kg day^{-1}, Siskiwit: 3.1 kg day^{-1}, Sand: 3.9 kg day^{-1}).

Following the July 12th storm, instantaneous DOC loadings also increased to a much larger degree than either SRP or TDP. Relative to mean baseline loading conditions, the DOC loading of the Sand River approximately tripled after the storm event (368 kg day^{-1}). The DOC loading for both the Bois Brule and the Iron River increased to about four times the average baseline level (6,929 kg day^{-1}and 5,872 kg day^{-1}; respectively). The Flag and Siskiwit River daily DOC loading increased to an even greater degree following the storm event (1,615 kg day^{-1}and 1,270 kg m^{-1}; respectively). After the storm, loadings of POC increased as well (Brule: 837 kg day^{-1}, Iron: 1,095 kg day^{-1}, Flag: 409 kg day^{-1}, Siskiwit: 174 kg day^{-1}, Sand: 120 kg day^{-1}); however, DOC loadings to the nearshore zone were still greater. Clearly, following an episodic

storm event, a greater amount of total organic carbon enters nearshore Lake Superior in comparison to total phosphorus.

The concentrations of SRP, TDP, and DOC exhibited very different spatial and temporal patterns of variation along the nearshore-offshore transect (Fig. 2.18 through Fig. 2.20). Over the 2016 field sampling season, SRP, TDP, and DOC concentrations ranged between 0.16 – 1.83 μg L^{-1}, 0.37 – 1.95 μg L^{-1}, and 0.57 – 3.91 mg L^{-1}; respectively. The particulate fractions, PP and POC, ranged between 1.41 – 4.80 μg L^{-1} and 0.08 – 0.24 mg L^{-1}; respectively. Interestingly, over the course of the summer PP and POC showed no statistically significant increase or decrease ($p>>0.01$). In early summer and fall, concentrations of SRP, TDP, and DOC showed little to no variation along the nearshore-offshore transect regardless of depth and distance offshore. By contrast, the distribution of these nutrients and organic carbon fractions showed definitive spatiotemporal trends in the month following the July 12th storm event.

On July 28th, SRP concentrations increased significantly (1.30 μg L^{-1}± 0.12 μg L^{-1}), and TDP concentrations followed a similar trend (1.62 μg L^{-1}± 0.23 μg L^{-1}). With respect to all other sampling days, the increases in dissolved phosphorus concentrations were statistically significant for each fraction, SRP ($F_{5,10}$= 28.3, p = 4.2x10^{-9}) and TDP ($F_{5,10}$ = 17.4, p = 6.7x10^{-8}). Dissolved phosphorus concentrations within the nearshore at 10 m in depth were slightly higher (SRP: 1.51 μg L^{-1}± 0.25μg $L^{-1}$and TDP: 1.79 μg L^{-1}± 0.14μg L^{-1}) relative to the lake surface and 20 m in depth. These increases were not statistically significant (a = 0.01), however, the probability (0.015) was only marginally higher than a, which suggests the increase was substantial.

The mean concentration of DOC on July 28th increased significantly (2.43 mg L^{-1} ± 0.99 mg L^{-1}). In comparison with the other sampling days, the periodic increase in DOC on July 28th was statistically significant ($F_{5,10}$= 14.8, p = 4.9x10^{-5}). Between July 28th and August 17th,

average whole-water column SRP and TDP decreased to a lesser extent that that of DOC (-0.55 μg L^{-1}, -0.59 μg L^{-1}, and -0.92 mg L^{-1}; respectively).

About a month after the initial storm event, the mean SRP and TDP concentration decreased, relative to July 28th (0.56 μg L^{-1} ± 0.09 μg L^{-1}, 0.59 μg L^{-1} ± 0.07 μg L^{-1}; respectively) along the nearshore-offshore transect. SRP and TDP mean concentrations on August 17thwere not statistically greater than mean pre-storm and fall concentrations ($p >> 0.01$ for both). However, SRP and TDP concentrations followed a distinctive nearshore-offshore spatial trend. Mean concentrations of SRP and TDP were significantly higher between 0 and 2.67 km offshore (1.12μg L^{-1} ± 0.14 μg L^{-1}, 1.38μg L^{-1} ± 0.31 μg L^{-1}; respectively) and exhibited a decreasing trend toward offshore waters (0.65μg L^{-1} ± 0.24 μg L^{-1}, 0.89μg L^{-1} ± 0.19 μg L^{-1}; respectively). The difference in SRP and TDP between the nearshore and offshore zones was statistically different on August 17th ($F_{2,10} = 8.49$, $p = 2.1x10^{-3}$; $F_{2,10} = 7.18$, $p = 9.2x10^{-3}$; respectively). The nearshore-offshore spatial differences in SRP and TDP on August 17th are illustrated in Fig. 2.18 and Fig. 2.19. On August 17th, the DOC concentration within the water column along this nearshore-offshore transect was relatively uniform (1.51 mg L^{-1} ± 0.23 mg L^{-1}), and there were no significant spatial or temporal differences ($p >> 0.01$). Between August 17th and September 21st, average whole-water column SRP and TDP decreased to a greater extent than that of DOC (-0.46 μg L^{-1}, -0.51 μg L^{-1}, and -0.20 mg L^{-1}; respectively).

The resultant horizontal and vertical SRP, TDP, and DOC gradients in response to episodic inflow are more clearly visualized in Fig. 2.18 through Fig. 2.20. However, it must be noted that there is substantial interpolation between the surface, 10 m, and the 20 m in depth introducing the potential for either an overestimation or underestimation of SRP, TDP, and DOC between these depths. From these contour plots, it is apparent that although the majority of the

surface plume dissipated about two weeks after the storm event concentrations of dissolved phosphorus within the nearshore zone remained higher for a longer period of time than DOC.

Table 2.2: Instantaneously measured total phosphorus (SRP, TDP, and PP fractions) and total organic carbon (DOC and POC fractions) loadings in kg day^{-1} for each sampled tributary in 2016.

Rivers	Date 2016	SRP Load (kg day^{-1})	TDP Load (kg day^{-1})	PP Load (kg day^{-1})	DOC Load (kg day^{-1})	POC Load (kg day^{-1})
Bois Brule	June 22	3.5	7.9	5.5	3528.8	261.4
	July 6	2.8	7.3	8.8	1668.6	283.2
	July 15	4.9	7.5	22.8	6929.2	873.3
	July 27	3.2	6.7	6.6	2113.3	266.5
	August 16	2.2	3.9	5.2	1524.1	134.6
	September 22	1.9	4.7	6.1	1477.1	222.3
	October 26	2.3	4.3	2.2	1291.9	92.5
Iron	June 22	3.2	9.7	7.7	3432.1	228.2
	July 6	4.7	5.9	7.7	1474.9	230.9
	July 15	7.5	11.9	37.3	5872.4	1095.8
	July 27	1.2	3.7	5.5	1772.3	169.8
	August 16	2.0	3.7	4.4	1154.3	92.5
	September 22	1.9	5.6	4.6	1679.1	163.1
	October 26	3.0	4.5	2.7	1074.8	80.9
Flag	June 22	1.8	2.6	2.1	729.8	56.9
	July 6	2.0	2.4	1.5	268.8	49.7
	July 15	3.2	3.4	10.5	1615.3	409.0
	July 27	1.0	2.3	2.0	249.0	67.9
	August 16	2.0	2.1	1.6	241.4	205.9
	September 22	1.6	2.9	1.7	467.9	54.6
	October 26	1.1	1.6	1.1	162.5	35.7
Siskiwit	June 22	0.7	1.8	0.9	356.7	30.2
	July 6	0.4	0.9	0.8	150.8	26.4
	July 15	2.2	1.8	3.1	1270.7	174.0
	July 27	0.7	1.0	1.3	397.7	58.8
	August 16	0.6	0.8	0.8	344.0	20.8
	September 22	0.8	1.4	0.6	427.0	22.7
	October 26	0.7	0.9	0.6	165.0	15.6
Sand	June 22	0.3	0.7	0.5	264.1	18.6
	July 6	0.3	0.5	0.6	76.2	9.7
	July 15	0.3	0.5	3.9	381.6	119.7
	July 27	0.1	0.1	0.7	192.8	23.1
	August 16	0.1	0.1	0.7	34.4	20.3
	September 22	0.1	0.3	0.2	234.7	7.5
	October 26	0.2	0.2	0.3	160.1	8.1

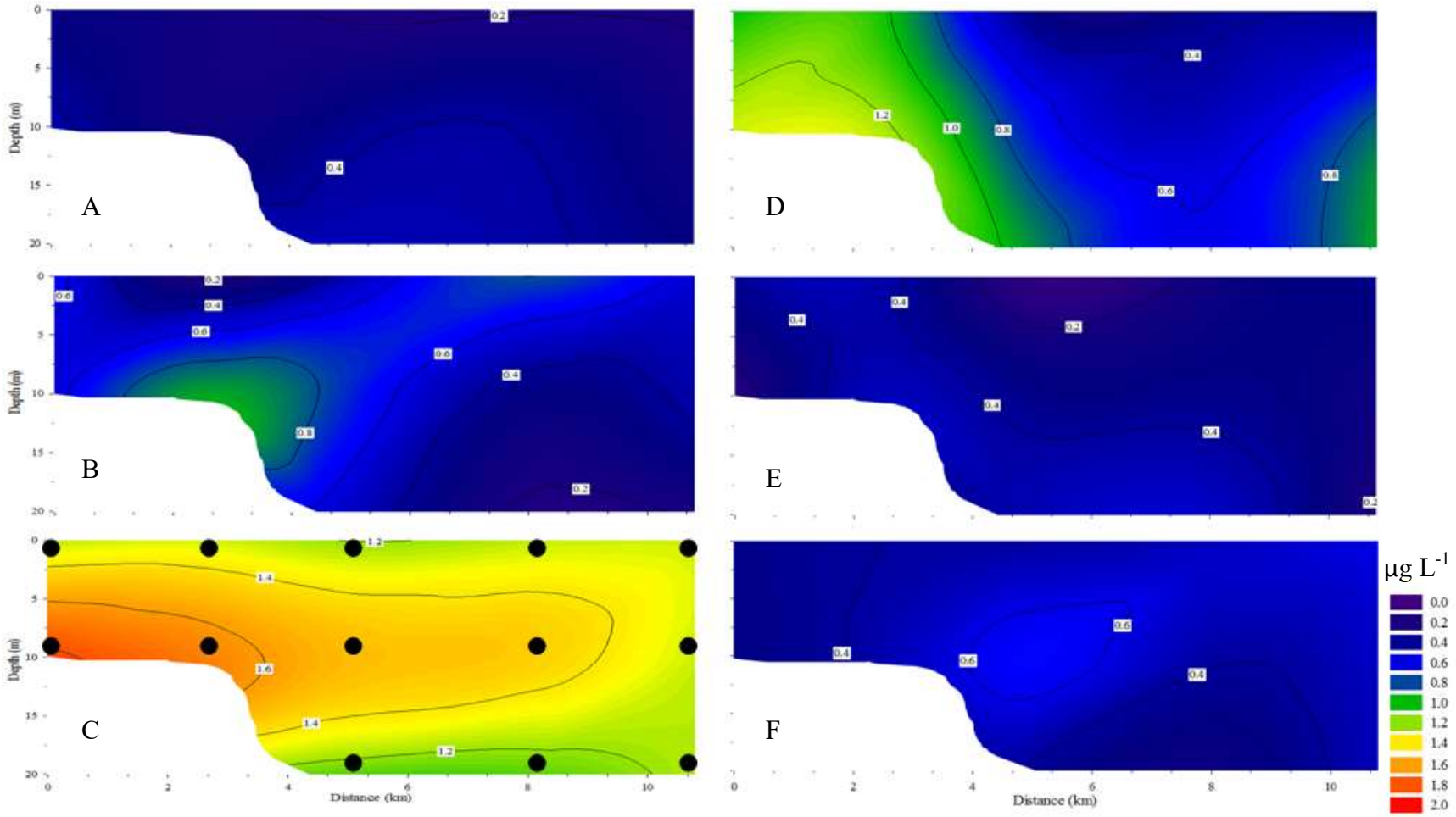

Figure 2.18: Colored contour plots showing the vertical and horizontal distribution of SRP over time; (A) June 23rd, (B) July 7th, (C) July 28th, (D) August 17th, (E) September 21st, and (F) October 25th. Cooler colors (i.e. blue and purple) represent areas of relatively low concentrations. The black dots on panel C represent location and depth of discrete water samples. Concentration units are µg L^{-1}.

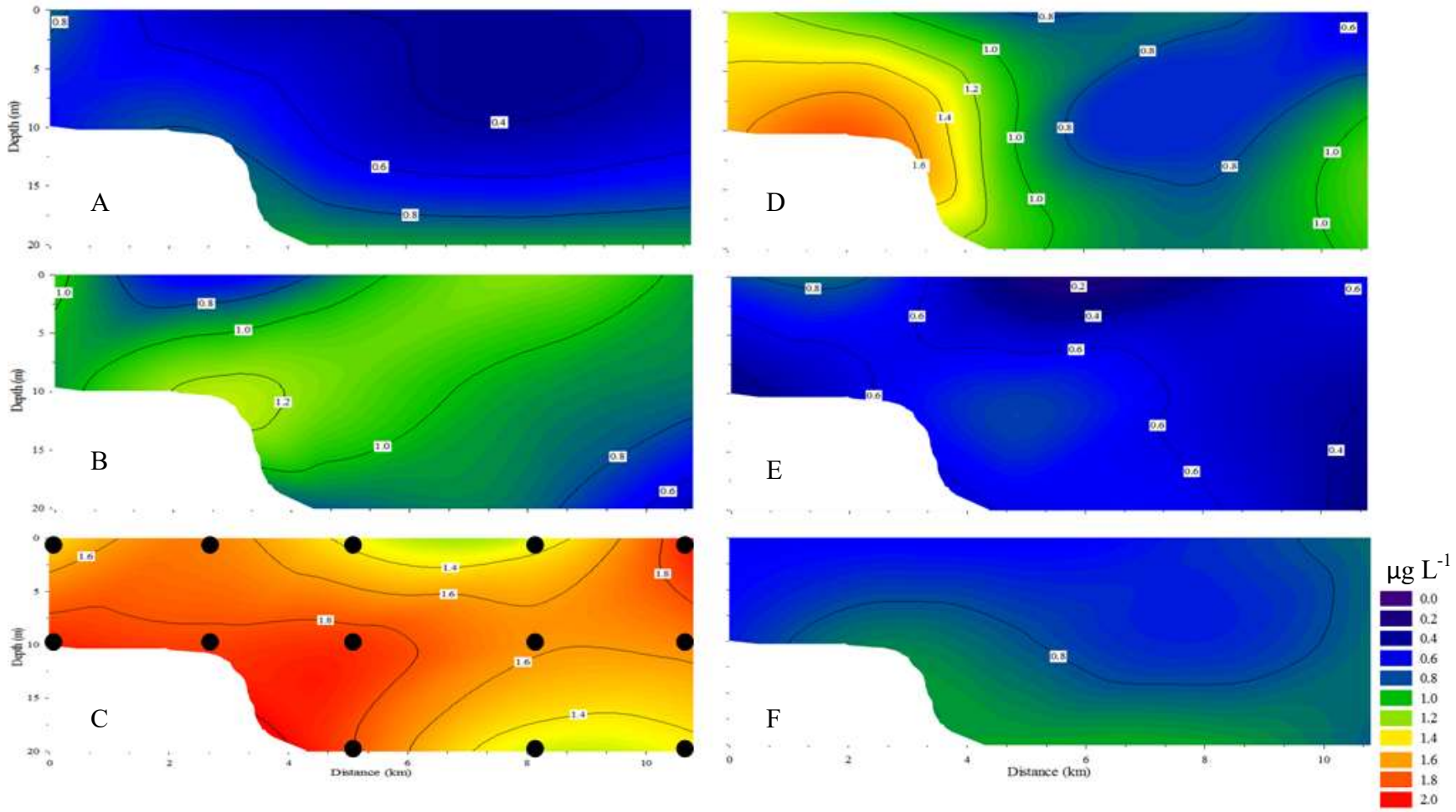

Figure 2.19: Colored contour plots showing the vertical and horizontal distribution of TDP over time; (A) June 23rd, (B) July 7th, (C) July 28th, (D) August 17th, (E) September 21st, and (F) October 25th. Cooler colors (i.e. blue and purple) represent areas of relatively low concentrations. The black dots on panel C represent location and depth of discrete water samples. Concentration units are µg L^{-1}.

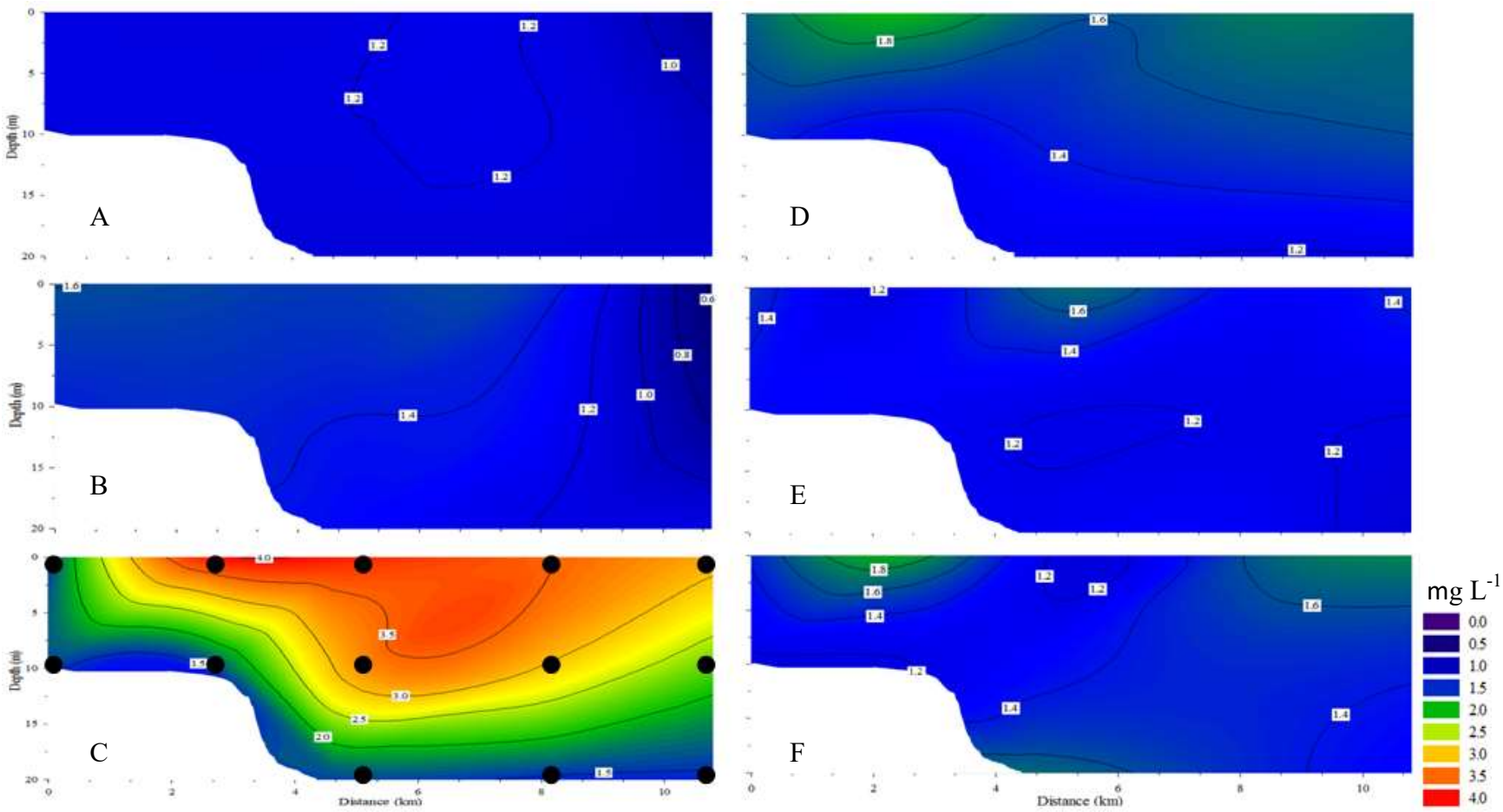

Figure 2.20: Colored contour plots showing the vertical and horizontal distribution of DOC over time; (A) June 23rd, (B) July 7th, (C) July 28th, (D) August 17th, (E) September 21st, and (F) October 25th. Cooler colors (i.e. blue and purple) represent areas of relatively low concentrations. The black dots on panel C represent location and depth of discrete water samples. Concentration units are mg L^{-1}.

Phytoplankton Spatial & Temporal Variability

Along the nearshore-offshore transect, mean Chl*a* fluorescence-derived concentrations increased in the month following the episodic storm event on July 12th (Fig. 2.21).The mean Chl*a* concentration on July 28th for this nearshore-offshore cross section (1.91 μg L^{-1} ± 0.04 μg L^{-1}) was statistically greater than any of the other sampling days ($F_{5,20}$ = 110.5 , p < 2.2 x 10^{-16}). On August 18th, Chl*a* concentrations decreased slightly (1.60 μg L^{-1} ± 0.07μg L^{-1}). Mean Chl*a* concentrations on August 18th were comparable to that of June 23rd (1.47 μg L^{-1} ± 0.45 μg L^{-1}), and were, therefore, not statistically different (p >> 0.01). Although Chl*a* concentrations on August 18th were not statistically different from those on June 23rd, they were much greater than July 7th, September 21st, and October 25th (1.21 μg L^{-1} ± 0.04 μg L^{-1}, 1.20 μg L^{-1} ± 0.02 μg L^{-1}, 1.25 μg L^{-1} ± 0.03 μg L^{-1}; respectively). These differences between August 18th and July 7th, September 21st, and October 25th were statistically significant ($F_{5,20}$ = 92.4, p < 2 x 10^{-16}; $F_{5,20}$ = 96.7, p < 2 x 10^{-16}; $F_{5,20}$ = 89.2, p < 2 x 10^{-16}; respectively).

Not only did Chl*a* concentrations vary temporally, they also varied spatially in response to the episodic storm event. The spatial variability in chl*a* concentrations are illustrated in Fig. 2.21 and Fig. 2.22. Early in the summer on June 23rd, the Chl*a* concentration of the upper 5 m of the water column was relatively low (0.59 μg L^{-1} ± 0.34 μg L^{-1}). Below 5 m, concentrations rose slightly (1.44 μg L^{-1} ± 0.35 μg L^{-1}) and were uniform throughout the nearshore-offshore transect.

Later in the summer on July 7th, mean Chl*a* within the water column decreased (1.21 μg L^{-1} ± 0.04 μg L^{-1}). A spike in Chl*a*, however, was apparent between 0 and 2.67 km offshore below 3 m (2.78μg L^{-1} ± 0.7 μg L^{-1}). On July 28th, following the storm event, mean Chl*a* increased significantly throughout the nearshore-offshore cross-section (1.91 μg L^{-1} ± 0.04 μg L^{-1}). Chl*a* increased within the entire water column between 0 and 2.67 km offshore (2.0 μg L^{-1} ±

0.6 μg L^{-1}), along the 10 m isobath (1.86 μg L^{-1} ± 0.47 μg L^{-1}), and at the furthest point offshore around 20 m (3.17 μg L^{-1} ± 0.75 μg L^{-1}).

On August 17th, Chl*a* concentrations decreased within the nearshore but remained high at the furthest points offshore (8.25 – 10.79 km). Within the nearshore on August 17th, the mean chl*a* concentration was1.20 μg L^{-1} ± 0.34 μg L^{-1}, and represented a significant drop in comparison to July 7th and July 28th. Further offshore, Chl*a* remained relatively high, especially between 8.25 to10.79 km offshore. At these distances offshore, mean Chl*a* was elevated between 5 to 20 m in depth (2.80 μg L^{-1} ± 0.5 μg L^{-1}). Similar to July 28th, the largest offshore spike in chl*a* between 5 to 20 m appears to be situated close to the pycnocline, which was at about 10 m (Fig. 2.14; A and D). Finally, on September 21st and October 25th the mean Chl*a* concentration along the nearshore-offshore transect decreased substantially (1.20 μg L^{-1} ± 0.02 μg L^{-1}, 1.25 μg L^{-1} ± 0.03 μg L^{-1}; respectively). There were no spikes in Chl*a* on these fall sampling days suggesting the water column along this cross-section was relatively uniform.

Estimates of euphotic depth based on turbidity vertical profiles show significant variation in depth of 1% light penetration following the major storm event (Fig. 2.26). On July 28th, the euphotic depth decreased, and averaged about 2 m across the entire nearshore zone. The ratio between the depth of the euphotic zone and epilimnion was considerably below 1 (0.3). The euphotic depth began to increase in the month following the storm event. This was evident by the increase in Z_{euph}:Z_{epi} ratio, which increased to 0.7 and eventually rose to 0.9 by September. Close to shore, the euphotic depth ranged between 5 and 6 m, and the depth of the euphotic zone increased further offshore reaching a maximum of around 9 m 8.25 km offshore. Over 10 km offshore, the water surface was slightly turbid which resulted in a slight decrease in euphotic depth. In the fall, the estimated euphotic depth was consistently greater than 9 m in depth. The

ratio was significantly depressed in October, most likely due to increased depth of the epilimnion as a result of cooler water temperature and increased mixing.

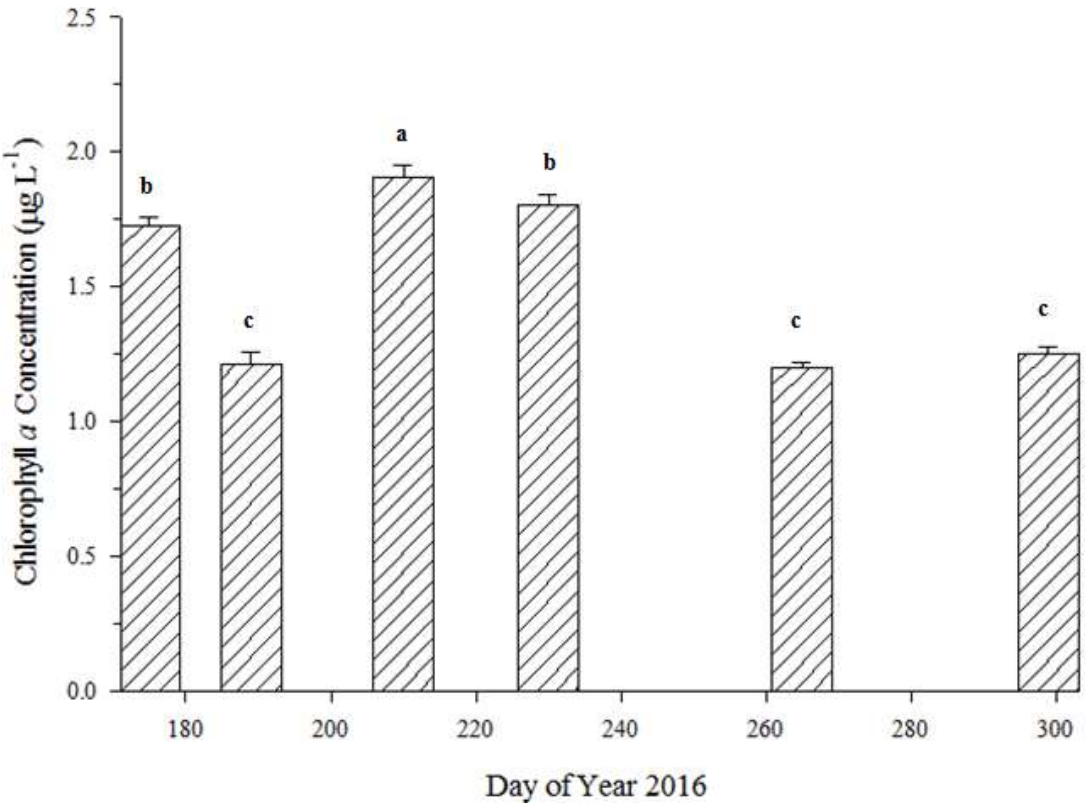

Figure 2.21: Daily mean Chl*a* fluorescence-derived concentrations for the entire nearshore-offshore transect on each sampling day with error bars. The letters indicate statistical differences between dates.

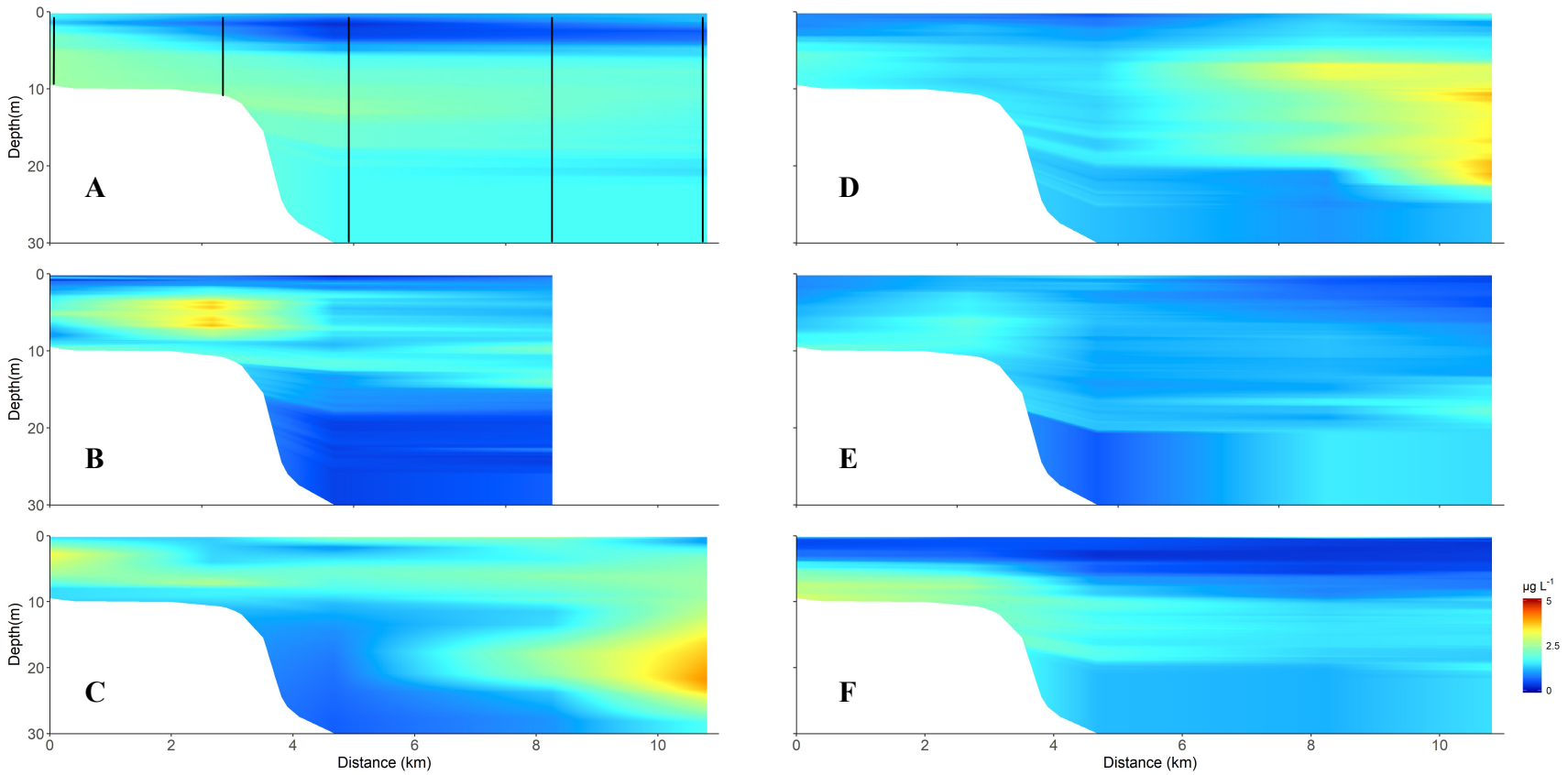

Figure 2.22: Chl*a* fluorescence-derived concentration spatial variability along the nearshore-offshore transect for each sampling day; (A) June 23, (B) July 7, (C) July 28, (D) August 17, (E) September 21, and (F) October 25 of 2016. Chl*a* concentrations are in µg L^{-1}, and range from 0 to from µg L^{-1}. The vertical black lines represent the location of vertical Chl*a* fluorescence profiles. It is important to note that on July 7, 2016 no Chl*a* fluorescence data was able to be obtained at the furthest location offshore.

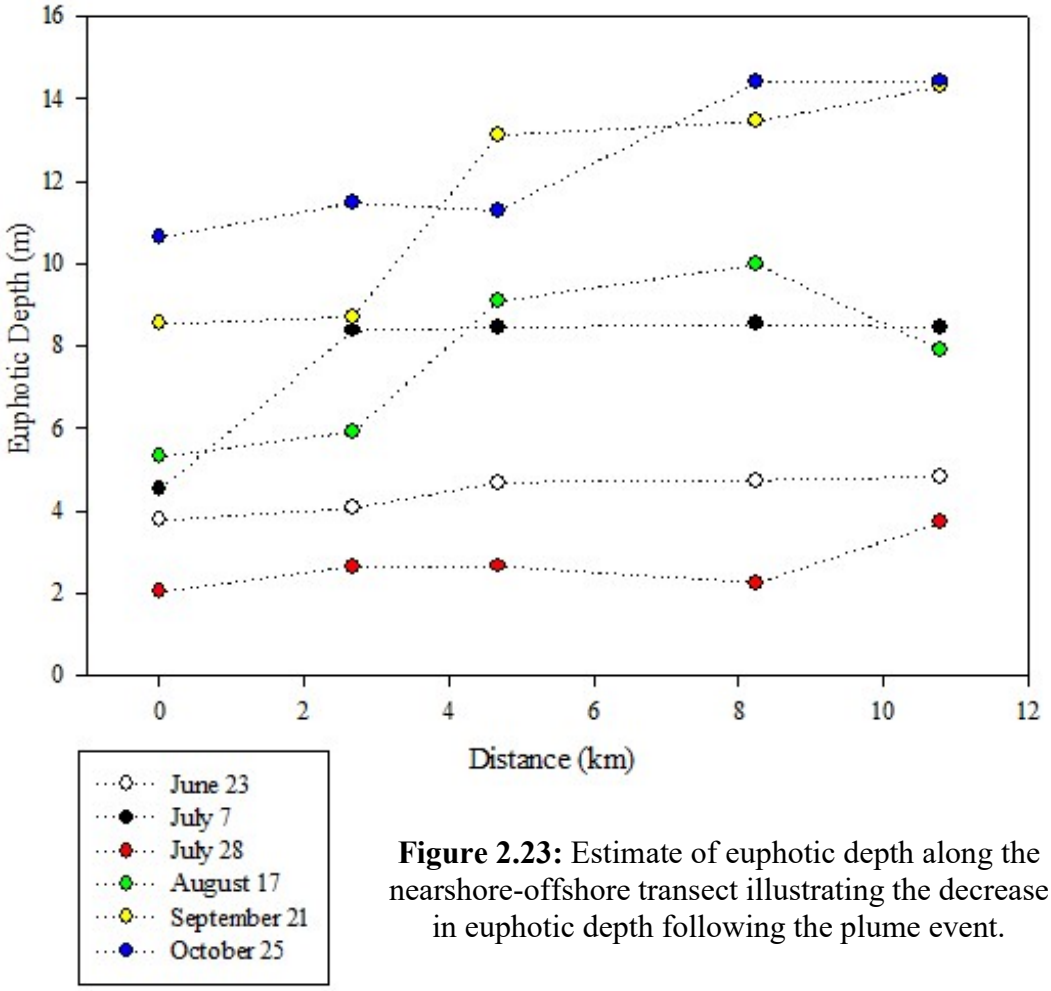

Figure 2.23: Estimate of euphotic depth along the nearshore-offshore transect illustrating the decrease in euphotic depth following the plume event.

Table 2.3: The depth of the euphotic zone (Z_{euph}), epilimnion (Z_{epi}), and the ratio between the two depths averaged along the nearshore-offshore transect for each sampling date. Estimates of depths (m) are based upon temperature and turbidity vertical profiles.

Date	Z_{euph}	Z_{epi}	Z_{euph}:Z_{epi}
June 23 2016	4.0	12.0	0.3
July 7 2016	7.3	5.0	1.5
July 28 2016	2.2	8.0	0.3
August 17 2016	7.6	10.6	0.7
September 21 2016	11.4	13.0	0.9
October 25 2016	12.4	30+	0.4

Discussion

Although mean wind speed was high during the storm on July 12th (10.5 m s^{-1}; NDBC buoy 45028), the lack of increased whole water column turbidity and shallow depth of the thermocline two weeks after the storm suggests that the surface plume was most likely a result of tributary discharge rather than a significant resuspension event. Surface plumes driven by resuspension events are a common occurrence in southern Lake Michigan following episodic wind events in the early spring (Lou et al., 2000; Eadie et al., 2002). The wind events that drive the Lake Michigan resuspension plumes, however, are significantly larger (> 15 m s^{-1}) than what occurred on July 12th in western Lake Superior. Despite the variability in current velocity and direction, mean nearshore current supports the horizontal spread of riverine input along the surface shown in Figure 2.9. The mean nearshore current illustrated in Figure 2.10 suggests river

subsurface interflow follows a similar pattern, and so the physical, chemical, and biological changes within the nearshore may reflect the maturation of the episodic tributary plume.

Episodic storm events, such as was seen on July 12, 2016, and the accompanying river loading of nutrients, organic carbon, and water are important drivers of spatial and temporal heterogeneity within the nearshore zone of western Lake Superior. Following the storm event, the discharge of all tributaries in the area increased significantly. In some cases, discharge tripled baseline flow conditions. The short lag time between the end of rainfall and the subsequent spike in discharge indicates that rivers in this region are highly susceptible to episodic runoff events. The short response time between episodic discharge and the appearance of a surface plume also suggests watersheds in this region are relatively impervious and have little storage. The surrounding watershed of western Lake Superior consists of predominantly red clay (US EPA, 1979), which is significantly less permeable in comparison to other soil types (Mesri and Olson, 1971). The impermeability of soil in this region forces water to flow overland quickly resulting in large fluctuations in river discharge.

The magnitude of tributary influence following the storm event is highlighted by both horizontal and vertical patterns within the nearshore zone. Prior to the storm event, nearshore waters of Lake Superior were relatively uniform as evident in the satellite imagery and vertical profiles of EC_{25} and turbidity. On July 7th, there were no spikes in EC_{25} or turbidity within the water column suggesting there was no significant riverine input to the region. Furthermore on July 12th, immediately following the storm, the surface water of western Lake Superior was still relatively clear. However, there was evidence of increased turbidity at the surface near the river-lake confluence of larger rivers, such as the St. Louis, Bois Brule, and Iron, which suggests the beginning of surface plumes. Four days later, the resultant surface plume reached its full extent

(over 2,700 km^2 and extending over 12 km offshore). The surface plume slowly began to dissipate as evident by the decreasing overall area on July 18th and July 25th. By July 25th, much of the surface plume had dissipated in comparison to the week immediately following the storm event.

Despite the breakdown of the surface plume over time prior to July 25th, the plume was still apparent, and covered more than 800 km^2 of the nearshore zone of western Lake Superior. Within the Apostle Islands archipelago, the surface water was still relatively turbid. Below the surface, vertical profiles of EC_{25} and turbidity on July 28th suggest the presence of significant riverine subsurface intrusions near the Apostle Islands archipelago. Vertical current profiles suggest these subsurface intrusions flowed northeastward, and were relatively constrained to the nearshore zone. The flowpath of subsurface intrusions are dependent on turbulent mixing and density gradients. Increases in turbidity were constrained to the surface, whereas spikes in EC_{25} appeared to propagate horizontally along the thermocline as intrusions of neutral buoyancy. This suggests the presence of multiple inflowing rivers to the region. The less dense, larger rivers, the St. Louis, Bois Brule, and Iron Rivers, were constrained to the surface, whereas the denser Flag, Siskiwit, and Sand Rivers reached neutral buoyancy along the thermocline. The larger rivers drain larger watersheds, and as such have greater average discharge and associated sediment loads relative to the smaller rivers suggesting larger rivers account for the increased turbidity seen at the surface. It is important to note that although spikes in EC_{25} occurred near the thermocline, EC_{25} was also slightly elevated at the surface. The difference in magnitude of EC_{25} between the surface and thermocline suggests that by the time river water from the larger rivers reached the Apostle Islands it had mixed to some degree with ambient Lake Superior water.

External, episodic loadings of phosphorus and organic carbon have been shown to significantly influence the distribution of phytoplankton (Popovskaya, 2000) as well as community metabolic processes (Hanson et al., 2003; Smith & Prairie, 2004). Understanding the impact of storm events on phosphorus and organic carbon dynamics requires the consideration of the flowpath of inflowing rivers, as well as the area of a lake that is affected. As described above, the flowpath of river inflows are variable and dependent on density gradients within the receiving lake. Vertical density gradients, combined with time-dependent changes in the depth of nutrients and organic carbon brought in from tributaries, creates the contingency for the formation of distinct layers with differing chemical compositions. These layers may allow for the development of chemical and productivity gradients, as has been observed in fjords and coastal waters (Alldredge et al., 2001; McManus et al., 2003). In freshwater lakes, MacIntyre et al. (2006) showed that distinct chemical layers developing in response to storm events may be a common occurrence. Whether the distinct nutrient layer corresponds to increases in phytoplankton biomass is dependent on the magnitude of the nutrient layer and optimal light intensity. Based upon the increase in phosphorus and a literature review of phosphorus-limited phytoplankton growth in Lake Superior (Sterner et al., 2004), I thought Chl*a* concentrations would increased following the episodic plume event.

About two weeks after the storm event, the entire water column extending from nearshore to offshore was elevated in terms of dissolved phosphorus. At 10 m in depth, a distinct layer of elevated SRP and TDP concentrations formed across the nearshore zone (Fig. 2.18 and Fig. 2.19). The development of a distinct layer of SRP and TDP at 10 m corresponded to the depth of the pycnocline on July 28th (Fig. 2.13; D). Increases in Chl*a* were also apparent along 10 m in depth (Fig. 2.22; C) suggesting there was an increase in phytoplankton biomass along the

horizontal layer of greater SRP and TDP concentrations. The elevated Chl*a* along this depth gradient appears to follow the lower bound of the pycnocline (Fig. 2.13; A and D). In fact, the entire nearshore water column was elevated in terms of Chl*a* concentration on July 28th (Fig. 2.21). These increases in Chl*a* occurred despite the decreased water clarity at the surface on July 28th. Spikes in chl*a* also occurred deeper offshore (> 11 km) near 20 m in depth. According to Barbiero and Tuchman (2004), deep chlorophyll maxima develop between 23 – 35 m in Lake Superior. The elevated Chl*a* concentrations at 20 m almost 11 km offshore suggest the establishment of a deep chlorophyll maximum at a shallower depth in this region. On July 28th, DOC was higher, on average, at the surface than at 10 m in depth. This suggests either much of the DOC at 10 m was sequestered or metabolized out of the water column or loading of DOC from rivers propagating along the thermocline was much less than that of SRP or TDP. The tributary loadings in Table 2.2, however, suggest the latter is not the case.

A month later, SRP and TDP within the nearshore zone were still relatively high (SRP: 0.8 μg L^{-1}± 0.28 μg L^{-1}& TDP: 1.03 μg L^{-1}± 0.26 μg L^{-1}) in comparison to early summer and fall. At a depth of 10 m, SRP and TDP were still higher relative to the surface and 20 m in depth, however, the magnitude decreased in comparison to July 28th. Within 2 km of the shoreline, a vertical gradient in SRP and TDP appeared to develop on August 17th. Within 5 km of shore, concentrations of SRP and TDP remained elevated and decreased with distance offshore. The development of a vertical nutrient gradient at about 5 km offshore suggests some of the excess phosphorus had either been sequestered out of the water column or utilized by phytoplankton. An area of increased Chl*a* appeared between 6 and 11 km offshore, and between 5 and 20 m in depth suggesting there may be a relationship between depleted region of SRP and TDP offshore and the spike in Chl*a*.

On August 17th, DOC, however, decreased to pre-storm concentrations suggesting the excess DOC was removed from the water column relatively quickly. The presence of elevated SRP and TDP a month after the storm event and the corresponding return of DOC to pre-storm levels suggests a much quicker removal of DOC from the ambient water in comparison to dissolved phosphorus. The time-dependent asynchrony between apparent loss of DOC in comparison to that of SRP and TDP points to a net shift in nearshore metabolism to heterotrophy. Prairie et al. (2002) and Hanson et al. (2003) describe a similar pattern in temperate lakes across the US; however, these lakes only became heterotrophic when DOC was greater than 6 mg L^{-1}. Therefore, although DOC doubled following the storm event and appeared to be lost quicker, relative to SRP and TDP, these concentrations were much less than 6 mg L^{-1}, which suggests the nearshore may not shift toward net heterotrophy.

As nutrient and organic matter loading increases, the euphotic depth typically becomes more compressed in response to either increased algal biomass concentration or more turbid surface water. Remote sensing and vertical turbidity profiles suggest the latter drove decreases in estimated euphotic depth following the storm event. Increases in Chl*a* fluorescence on July 28th indicate increased phytoplankton biomass in response to nutrient influx; however, the significantly decreased water clarity and euphotic depth suggest these increases in Chl*a* fluorescence may be an artifact of phytoplankton shade adaptation. Barbiero and Tuchman (2004) concluded that this shade adaptation in Lake Superior phytoplankton within the deep chlorophyll maximum resulted in increased Chl*a* fluorescence. Barbiero and Tuchman (2004) used POC concentrations to determine depths of increased algal biomass in offshore waters of Lake Superior. Although the high tributary loading of POC makes using POC as a proxy for algal biomass difficult, the fact that there were no significant spatial and temporal differences in

POC within the nearshore suggests little to no change in phytoplankton biomass following the plume event. Therefore, estimates of phytoplankton biomass in this study must be taken with a grain of salt because of the very turbid riverine input.

The breakdown of organic matter by heterotrophic bacteria can occur under low light conditions, whereas the phytoplankton uptake of dissolved nutrients and subsequent production of organic matter cannot. The decreased euphotic depth and associated high surface turbidity, and therefore, less than optimal light conditions, points to a lack of phytoplankton response within the nearshore. However, further offshore, where the euphotic depth increases and light intensity is optimal, the influence of increased river loadings of nutrients may be expressed at the confluence between nearshore and offshore zones, and within the pelagic zone. Between august 17th and September 21st, the surface water cleared and euphotic depth increased, and on average more SRP and TDP left the system in comparison to DOC. This suggests an increased uptake of dissolved phosphorus under more optimal light conditions. Therefore, the interplay of light and nutrient availability drives the phytoplankton and metabolic response of the nearshore zone following a significant surface plume event.

Overall, these results show that rivers in western Lake Superior are highly influential in determining the distribution of SRP, TDP, and DOC. Although the storm occurred on July 12th, the impact of the rivers was apparent over a month later. The spatial variability of these nutrient and organic carbon fractions is dependent on the flowpath of incoming rivers. The persistence of observable distinct chemical layers suggests strong thermal stratification and low turbulent mixing within the nearshore zone of Lake Superior between July 2016 and August 2016. Although overall phytoplankton biomass did not appear to vary significantly in response the

influx of nutrients, the presence of a large nutrient pool and associated decreases over time suggest the potential for increased primary productivity within the nearshore.

Chapter 3: Metabolic Response of the Nearshore Zone of Lake Superior to an Episodic Inflow Event

Introduction

The complexity and dynamics of food webs and biogeochemical cycling in lakes are directly linked to the metabolic processes of primary production and respiration. For example, external inputs and internal cycling of phosphorus and other nutrients play a strong role in regulating phytoplankton production. Likewise, respiration by heterotrophs is accompanied by nutrient regeneration, and can also indirectly influence nutrient cycles by regulating redox conditions. Photosynthesis utilizes light energy to generate chemical energy and convert inorganic carbon to biomass. This conversion of energy provides a basal energy source for aquatic food webs (Falkowski & Raven, 2013). Respiration, which is associated with oxygen consumption and the release of inorganic carbon, is a catabolic process through which organisms break down organic compounds to generate energy. This process represents the largest sink of organic matter in aquatic ecosystems (del Giorgio & Williams, 2005).Lake metabolic balances represent the difference between primary production (CO_2 consumption) and respiration (CO_2 production). The balance between the metabolic processes of gross primary production (GPP) and respiration (R) represents net ecosystem production (NEP):

$$\mathrm{NEP} = \mathrm{GPP} - \mathrm{R}$$

The combined production, synthesis, and breakdown of organic matter by all organisms within an ecosystem can be summed to quantify the community metabolism of that ecosystem. Net ecosystem production can be used to define lake trophic classification, with positive values corresponding to autotrophy and negative values to heterotrophy. The sign of net ecosystem production indicates whether or not the aquatic ecosystem is a sink or source of atmospheric

CO_2. In a metabolically balanced, closed system, all organic matter generated through primary production is metabolized through respiration and the two processes are equal. In natural systems, however, this is rarely the case.

Understanding the community metabolic response of aquatic ecosystems to significant environmental variations has been of great interest to ecologists. In particular, nearshore ecosystems of large lakes are more readily impacted by environmental variations in land-cover (Yurista et al., 2011; Homer et al., 2015), climate patterns (Christensen et al., 2003; Austin and Coleman, 2007), and human activities (Allan et al., 2013; Chu et al., 2014). These variables influence riverine input of nutrients and energy (in the form of organic carbon), as well as the forms and proportions of these materials (Gilbert, 2012).

Both phytoplankton and periphyton communities are heavily dependent on nutrient availability and, as such, nutrient abundance is often a limiting factor in their ability to generate organic matter (Schindler and Nighswinder, 1970; Schindler, 1978; Vadeboncoeur et al., 2008). Within aquatic systems, nutrient availability is ultimately determined by external inputs. For example, nutrient-rich river inflow has been shown to support elevated primary production levels in the Gulf of Mexico near the interface between the Mississippi and Atchafalaya Rivers and the Gulf (Lohrenz et al., 1990; Rabalais et al., 1996; Lohrenz et al., 1997). However, internal recycling of nutrients, specifically phosphorus, often modulates whole-lake primary productivity in these ecosystems, and internal processing of nutrients and organic carbon can play a large role in determining whether a system is net heterotrophic or autotrophic. Hence it is important to understand how externally-derived nutrients and organic carbon are processed within lakes in order to predict how lakes will respond to changes in external loading.

Episodic inflow and eroded soils entering lake ecosystems via rivers contain a large amount of essential substances for nearshore biota, such as organic carbon and nutrients (including phosphorus and nitrogen). While organic carbon primarily serves as an energy source for bacteria (Tranvik, 1992; del Giorgio et al., 1997; Kritzberg et al., 2004), nutrients can support both bacteria and autotroph communities. The effects of nutrient subsidies will depend on the availability of light which is regulated by suspended matter and colored dissolved organic matter (CDOM) concentrations introduced along with the river inflow (Bocaniov et al., 2013). In particular, CDOM creates a much darker aquatic environment by directly absorbing photosynthetically available light (Mouw et al., 2013). Therefore, on an areal basis, inputs of CDOM may reduce primary productivity due to the low light conditions (Minor et al., 2014; Thrane et al., 2014) and heterotrophic bacterial respiration increases (Jansson et al., 2000), resulting in net heterotrophy. At the edges of these turbid inflows, however, nutrient as well as light availability may be sufficient to increase primary production rates. Therefore, metabolic gradients (i.e. high respiration-low productivity to moderate respiration-high productivity), may exist at the outer edges of river plumes.

Rates of planktonic respiration tend to covary with rates of primary production (del Giorgio & Peters, 1994). However, heterotrophic bacterial respiration may vary in response to fluctuations in the concentration and quality of the organic carbon pool (Tranvik, 1992; del Giorgio et al., 1997). Aquatic ecosystems often receive organic carbon from multiple sources, including, autotrophic production and allochthonous subsidies. The different sources may contribute to apparent uncoupling between community respiration and primary production rates.

In many low productivity ecosystems, respiration exceeds photosynthesis in response to allochthonous inputs of organic carbon. Typically, these subsidies are the result of increased

river loading or ground water influxes (Russ et al., 2004).The increase in allochthonous organic carbon subsidies drives community respiration and results in CO_2 supersaturation. Cole et al. (1994) showed patterns of persistent CO_2 supersaturation in many temperate and tropical lakes. For example, Lake Superior has been repeatedly shown to be a net source of CO_2 to the atmosphere (Cotner et al., 2004; Urban et al., 2004; Atilla et al., 2011).These patterns suggest external inputs of organic matter considerably subsidize aquatic food webs driving these ecosystems towards net heterotrophy.

Although organic carbon of planktonic origin may be easily metabolized, inputs of DOC from the terrestrial landscape are considered to be refractory (Tranvik, 1992). However, a number of studies have shown that a portion of terrestrially-derived DOC is labile to microbial remineralization (Tranvik, 1992; del Giorgio et al., 1997; Kritzberg et al., 2004). In smaller lakes, since the loading of allochthonous organic carbon typically outweighs the generation due to primary production, respiration of even a small portion may have significant impacts on the community metabolic balance and food web productivity. The ratio of watershed to surface area for Lake Superior, 1.55, suggests the lake, as a whole, is far less impacted by its watershed in comparison to small lakes (Cotner et al., 2004). However, the nearshore area of Lake Superior is relatively small in comparison and is in close proximity to the watershed. Therefore, the nearshore area may be more readily influenced by allochthonous loadings of organic carbon and nutrients. Interestingly, contrary to the perception that Lake Superior as a whole is a net source of CO_2 to the atmosphere (Cotner et al., 2004; Urban et al., 2004; Atilla et al., 2011), Russ et al. (2004) showed that during the spring and summer the western region of the lake shifts slightly towards net autotrophy. This suggests that river inputs have a much stronger effect on primary production than respiration in this area of Lake Superior.

In this chapter, I address three specific hypotheses: 1) River discharge promotes net heterotrophy within the nearshore ecosystem of western Lake Superior, 2) the variability in pCO_2 at the surface within the nearshore is controlled by biological factors following the influx of dissolved nutrients and organic carbon, and 3) episodic inflow events generate strong metabolic (i.e. primary production - respiration) spatial gradients. The objectives of this study were three-fold: 1) generate vertical profiles of O_2 and CO_2, which are the primary dissolved gases reflecting metabolic processes, 2) determine whether vertical changes in the partial pCO_2 correspond to areas of increased algal biomass and distinct gradients of dissolved nutrient and organic carbon, and 3) quantify the net CO_2 and O_2 lake-atmosphere flux.

Methods

Sampling Frequency & Spatial Coverage

The sampling frequency and spatial coverage for determining the community metabolic response were the same as previously stated in Chapter 2 (see page 19).

Spatiotemporal Variability in pCO_2 & O_2 % Saturation

The availability of equipment used to reliably measure free-water dissolved gases, such as O_2 and CO_2, affords a comprehensive analysis of spatiotemporal changes in the Lake Superior nearshore community metabolism. In measuring community metabolism, free-water measurements of dissolved gases directly influenced by metabolic processes have considerable advantages over incubation methods. Incubation approaches to measuring community primary production and respiration suffer from problems in scale (Chen et al., 2000). Although incubation measurements may be more accurate, ecosystem heterogeneity makes scaling from

incubation chambers/bottles to whole system highly uncertain due to the propagation of error when accounting for errors in individual methods (Van de Bogert et al., 2007). In comparison, free-water measurements of dissolved gasses provide an integrative measure of net ecosystem metabolism with high vertical and horizontal resolution. Vertical profiles of free-water CO_2 may provide a more sensitive approach to assessing spatial and temporal differences in community metabolism. Relative to dissolved O_2, concentrations of CO_2 are much lower suggesting small variations may be more easily detectable and apparent.

Spatiotemporal patterns in nearshore Lake Superior pCO_2 profiles were validated through comparisons with the corresponding O_2 percent saturation profiles. In aquatic systems, O_2 percent saturation refers to the ratio of dissolved O_2 concentration in water to the saturated dissolved O_2 concentration at a given temperature and pressure. Changes in the relative influence of photosynthesis and respiration are reflected in corresponding changes in O_2 percent saturation, however, the influence of metabolic process on the saturation of O_2 is often masked by variations in temperature (Eveleth et al., 2014). For example, increases in primary production rates often result in associated supersaturation of O_2. In contrast, undersaturation of O_2 is often indicative of greater respiration rate and pCO_2 responds inversely. It is important to note that temperature significantly affects the solubility of gases, and so temperature changes need to be taken into account when interpreting the causes of pCO_2 and % O_2 fluctuations.

Vertical profiles were conducted (see Figure 2.3) to measure dissolved O_2 % saturation, temperature, and pH and the response of these variables to river plume dynamics. Vertical profiles of aqueous CO_2 concentration ($[CO_{2(aq)}]$; hereafter) were generated through a direct calculation method, considering variables such as pH, alkalinity, temperature, atmospheric

pressure, and ionic strength. If two variables within the inorganic carbon system are known, all the remaining variables can be calculated according to the equilibrium reactions (Millero, 2007).

$$CO_{2(g)} \leftrightarrow CO_{2(aq)}$$
$$CO_{2(aq)} + H_2O \leftrightarrow H^+ + HCO_3^-$$
$$HCO_3^- \leftrightarrow H^+ + CO_3^{2-}$$

The relative concentrations of $[HCO_3^-]$, $[CO_3^{2-}]$, and $[CO_{2(aq)}]$, as well as $[OH^-]$ and $[H^+]$, comprise the carbonate alkalinity of the aquatic system. In many natural freshwater systems, total alkalinity predominantly consists of bicarbonate (HCO_3^-) and carbonate (CO_3^{2-}).Therefore, the carbonate alkalinity of western Lake Superior was used as a proxy for total alkalinity.

The carbonate alkalinity for western Lake Superior was determined through the use of gas chromatography. Lake water samples were collected at three depths (surface, 10 m, and 20 m) during each trip. In the field, 120 mL glass serum bottles were filled with a tube placed at the bottom, and flushed with at least twice the volume of the bottle to avoid gas exchange with the atmosphere. Upon collection, the samples were sealed with rubber stoppers and stored on ice for transport. In the lab, $[CO_{2(aq)}]$ within the sample was first determined by replacing ¼ of the sample with N_2 headspace. After shaking the sample to equilibrate $[CO_{2(aq)}]$ with the gas headspace, 50 µL of gas sample was injected into a gas chromatograph (SRI Instruments Model 8610C). To analyze total dissolved inorganic carbon (DIC; hereafter), samples were acidified using concentrated phosphoric acid (H_2PO_4) to convert all DIC to CO_2, and the above procedure was repeated. Concentrations of HCO_3^- and CO_3^{2-} were adjusted iteratively to produce the target pH and alkalinity, and corrected for in situ temperature and ionic strength following (Cole et al., 1994). Carbonate alkalinity was then determined through the use of the following equation:

$$Alk_{carb} = [HCO_3^-] + 2[CO_3^{2-}] + [OH^-] - [H^+] \quad (5)$$

The resultant alkalinity values measured over the course of the field sampling season were averaged to determine a mean Lake Superior alkalinity (852.84 μeq L^{-1} ± 52.88 μeq L^{-1}, n = 162). A literature review for Lake Superior showed similar values in comparison to those obtained through the use of the gas chromatograph (Bootsma & Hecky, 2003; Sterner, 2011; Chapra et al., 2012). The mean alkalinity obtained through this method, coupled with pH and temperature profiles, was used to generate vertical profiles of $[CO_{2(aq)}]$.

$[CO_{2(aq]}]$ was calculated for every ¼ m depth increment. These increments correspond to measurements of temperature and pH, both of which were critical to the determination of $[CO_{2(aq)}]$. The first and second dissociation constants of carbonic acid and bicarbonate, k_1 and k_2, were used to determine in situ $[CO_{2(aq]}]$.

$$k_1 = \frac{[HCO_3^-]*[H^+]}{[CO_{2(aq)}]} \quad (6)$$

$$k_2 = \frac{[CO_3^{2-}]*[H^+]}{[HCO_3^-]} \quad (7)$$

Corrections for k_1 and k_2 were made to account for variations in temperature at each depth increment. Vertical profiles of $[CO_{2(aq)}]$ were solved for algebraically, using a constant alkalinity, pH profile data, and the equations for both dissociation constants. The resultant formula for calculating $[CO_{2(aq)}]$ based on the rearrangement of the dissociation constant equations and the carbonate alkalinity equations is as follows:

$$[CO_{2(aq)}] = \frac{\left(\frac{[H^+]}{k_2}\right) * \left(\frac{(Alk_{carb} - [OH^-])}{\frac{[H^+]}{k_2} + 2}\right) * [H^+]}{k_1} \quad (8)$$

where, Alk_{carb}, refers to the carbonate alkalinity, $[H^+]$, is the concentration of hydrogen ions based on pH data, $[OH^-]$ is the concentration of hydroxide ions based on pH data, and, k_1 and k_2, refer to the temperature-corrected first and second dissociation constants of carbonic acid.

Vertical profiles of $[CO_{2(aq)}]$, in mol L^{-1}, were converted to partial pressures of CO_2 (pCO_2) to account for differences in day-to-day atmospheric pressure, as well as to allow for the determination of flux across the lake – atmosphere interface. The equilibrium between atmospheric and dissolved gases is governed by Henry's Law, which states that at a given temperature, the concentration of a gas that dissolves in a given type and volume of liquid is proportional to the partial pressure of that gas (Sander, 2015).

$$p = k_H * c \quad (9)$$

where, p, is the partial pressure of a gas above the solution, c, is the concentration of the gas within the solution, and k_H, is the Henry's Law constant which has units of mol/(volume* pressure)(e.g. mol m^{-3} Pa^{-1}). The temperature dependency of Henry's constant is given by:

$$k_H = k_H^{\ominus} * \exp[(\frac{-\Delta_{soln}H}{R})*(\frac{1}{T} - \frac{1}{T^{\ominus}})] \quad (10)$$

where, $k_H^{\ominus}$ and $T^{\ominus}$, denotes Henry's constant and standard temperature (298.15 ^oK) and T is in situ temperature (^oK). The enthalpy of the solution for dissolution of specific gases is given by, $\Delta_{soln}H/R$. Values used for enthalpy vary between gases. For CO_2, the value used was for the enthalpy of freshwater 2,393 K (Sander, 2015).

To assess the validity of this approach for determining pCO_2 profiles, the surface water pCO_2 was directly compared to pCO_2 data obtained using a unique field system equipped with an infrared gas analyzer (IRGA) for in situ CO_2 analysis. This field system is more accurate and

provides real-time data, but, it does not allow for high vertical resolution data that could be acquired using sonde-derived pH values using the calculation method described above.

In this field system, the infrared (IR) absorption properties of CO_2 are used to determine the pCO_2. As a gas, CO_2 absorbs IR energy more readily at specific wavelengths, such as 4.24 μm. The pCO_2 in surface water can be determined through the comparison of the difference ratio of IR absorbance at 4.24 μm to a wavelength that is not readily absorbed by CO_2 (i.e. 3.95 μm). The IR absorbance of $CO_{2(g)}$ is measured in an infrared gas analyzer (LiCor LI-820 Gas Analyzer equipped with a CR-10x Data logger). Prior to entering the optical path of the IR analyzer, aqueous $CO_{2(aq)}$ must equilibrate with $CO_{2(g)}$ present in air within a closed-loop. Surface water flows through an equilibrator (MiniModule® 1x5.5 X50 Fiber) where $CO_{2(aq)}$ equilibrates with CO_2 in the gas phase that is moving in the opposite direction of the water, which increases the CO_2 air-water equilibration rate. The $CO_{2(g)}$ then is pumped into the IRGA where pCO_2 is measured. A diagram of the field system is shown in Figure 3.1.

To compare the applicability of the IR gas analysis and the direct calculation methods in determining pCO_2, a Deming regression between the two was performed. Deming regression is an extension of simple linear regression, which is capable of accounting for random measurement errors in the Y dimension as well as the X dimension (Martin, 2000). The relationship between the two methods was both positive and strong, and is shown in Figure 3.2. Therefore, I felt justified in using the direct calculation method to generate pCO_2 vertical profiles. Slight differences between the methods are most likely an artifact of variations in actual, in situ alkalinity. For simplicity, and because alkalinity was only measured at discrete depths, the alkalinity was kept constant (852.84 μeq L^{-1}) during the generation of pCO_2 profiles.

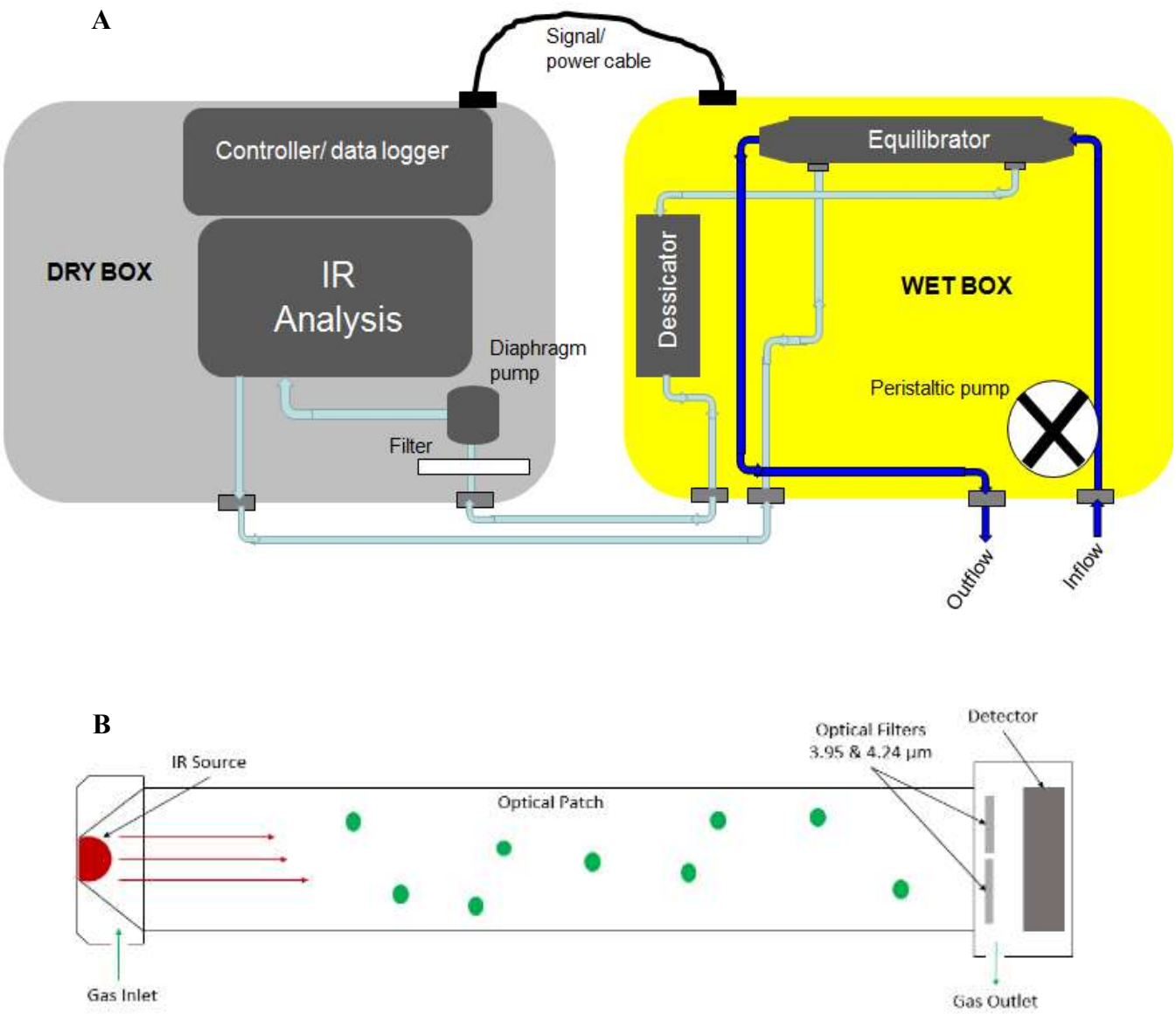

Figure 3.1: General layout of the various components and processes of the CO_2 field system which was developed by Harvey Bootsma, among others. (A) Depiction of the internal components of the field system, as well as the flow of water (dark blue arrows) and of closed-circuit air (light blue arrows). The system is divided into a "wet" and "dry" box. The "wet" box is where the water-air equilibration occurs whereas the "dry" box houses the majority of electrical equipment and is where the actual infrared (IR) analysis occurs. (B) Pictorial representation of the optical path within the IR analyzer. Each of the green dots represents individual CO_2 molecules.

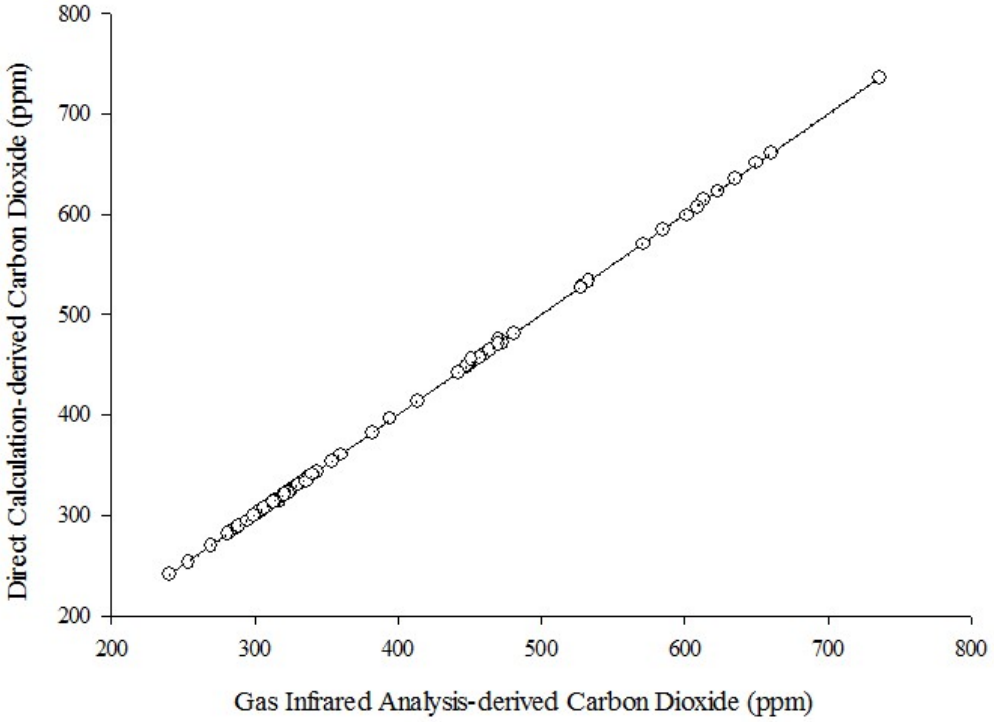

Figure 3.2: Comparison of two different methods for determining CO_2 concentration. A Deming regression of the scatter plot, slope is $1.2x10^{-6}$; the intercept 0.24; and the correlation coefficient, $r^2 = 0.98$ indicated a very strong correlation between the direct calculation and infrared analysis methods for CO_2 determination.

Lake-Atmosphere CO_2 & O_2 Flux

Lake-atmosphere flux of CO_2 was measured on June 23rd, July 7th, July 15th, July 28th, August 17th, September 21st, and October 25th. The biweekly sampling served to encapsulate the lake response to the episodic storm event that occurred on July 12th. The flux of CO_2 and O_2 between the lake surface and the ambient atmosphere has often been used as a means of assessing community metabolism. Comparisons between net CO_2 and O_2 lake-atmosphere flux provide insight into whether or not an aquatic environment is net auto- or heterotrophic at a given time. Gas fluxes are calculated according to Fick's first law of diffusion, while taking into account the thickness of the boundary layer and the molecular diffusion coefficients of each specific gas. A generalized mathematical representation of Fick's first law is shown below:

$$F_{a\text{-}w} = K * \Delta[c] \quad (11)$$

where, $F_{a\text{-}w}$, is the flux at the air-water interface in mole m^{-2} $s^{-1}$and, K, is the bulk transfer coefficient expressed in m s^{-1} (also called the "piston velocity"). The change in concentration of the gas between the water surface and the atmosphere is given by, $\Delta[c]$. The concentration of gas is expressed in mole m^{-3}. The sign and magnitude of the difference in concentration between the air and water determines the thermodynamic force and direction of flux while the transfer coefficient represents the kinetics of the process. Negative values of flux indicate gas being supplied from the atmosphere to the water. The surface water concentrations of O_2 and CO_2 were obtained at each sampling date and site following the methods described in Section 3.2.2. Prior to calculating gas flux, the concentrations of each gas were converted from mole L^{-1}, $[CO_{2(aq)}]$, and mg L^{-1}, $[O_{2(aq)}]$, to mole m^{-3}.

For O_2 flux at the air-water interface, the following equation can be formulated based on Fick's first law of diffusion.

$$Flux_{O_2} = K_{O_2} ([O_2] - [O_2]_{sat}) \quad (12)$$

where, flux is expressed as an amount transferred per area and time, mole m^{-2} s^{-1}, and the concentrations are given in amount per volume, mole m^{-3}. Finally, the transfer coefficient, K O_2, has the dimension of velocity, m s^{-1}. The equilibrium concentration of O_2 is a function of temperature and salinity and is given by the following expression in Benson and Krause (1984):

$$\ln[O_2]_{sat} = \ln[O_2]_{sat}(T) + f(T)*S \quad (13)$$

where, T, refers to temperature (^oK) and, S to salinity. The salinity for Lake Superior was determined to be approximately 0.0436 psu (Chapra et al., 2012), which are the units required for calculation of $[O_2]_{sat}$. The above expression includes a function, ln[O2]sat (T), for the value of saturation at zero salinity, and a temperature function, f (T). These two functions are detailed further in the Appendix A.

The O_2 bulk transfer coefficient is formulated by taking into the effect of wind speed on the kinetics of gas flux, and can be approximated following the approach of Wanninkhof (1992):

$$K_{O_2} = k_{600} * (Sc/600)^{-1/2} \quad (14)$$

where, k_{600}, is the gas transfer velocity for O_2 at 20^oC in freshwater (m s^{-1}). The variable, Sc, is the Schmidt number for oxygen. The Schmidt number for oxygen takes into account temperature (^oC), t, and can be expressed as:

$$Sc = 1953.4 - 120t + 3.9918\ t^2 - 0.050091\ t^3 \quad (15)$$

The gas transfer velocity for O_2, corrected for temperature, k_{600}, can be approximated from the equation derived by Wanninkhof (2009).

$$k_{600} = 0.333*u_{10} + 0.222*u_{10}^2 \quad (16)$$

The wind velocity (m s^{-1}) at 10 m above the water is represented by, u_{10}, which was obtained from the meteorological station on Devils Island.

The CO_2 flux at the air-water interface is determined in a similar manner to O_2, albeit with some small differences. The flux of CO_2 is given by the following expression:

$$Flux_{CO_2} = K_{CO_2} ([CO_2] - K_H * pCO_{2(air)}) \quad (17)$$

where, flux is again expressed in mole m^{-2} s^{-1}. The variable, K CO_2, corresponds to the bulk transfer coefficient of CO_2 in m s^{-1}; k_H, is Henry's constant for CO_2 expressed as mole m^{-3} atm^{-1}; $[CO_2]$, is the concentration of CO_2 in the surface water in mole m^{-3}, and, pCO_2, is the partial pressure of CO_2 in the atmosphere in atm. In the atmosphere, CO_2 is typically measured as a partial pressure. Therefore, Henry's law can be used to convert partial pressure to concentration in mole m^{-3} of CO_2.

The bulk transfer coefficient for CO_2 was calculated using the relationship described in Wanninkhof (1992):

$$K_{CO_2} = k_{600} * (Sc/600)^{-1/2} \quad (18)$$

where, k600, is the gas transfer velocity for CO_2 at 20°C in freshwater (m s^{-1}) and was calculated in the same manner as for O_2. The variable, Sc, is the Schmidt number for carbon dioxide. The Schmidt number for carbon dioxide takes into account temperature (°C), t, and can be expressed as:

$$Sc = 1911.1 - 118.11t + 3.4527\ t^2 - 0.04132t^3 \quad (19)$$

The comparison of flux between CO_2 and O_2 can provide insightful information on the metabolic balance of lake ecosystems. Although air-water flux can only address the metabolic balance of the epilimnion, the dense water below the thermocline of Lake Superior suggests

episodic river inflow may be constrained to the mixed layer. Therefore, the influence of river inflows on lake metabolism is likely reflected in epilimnetic gas concentrations

Temperature-Biological Effect on pCO_2

Although pCO_2 is modulated by metabolic processes, it is also influenced by shifts in temperature. Temperature directly impacts the solubility of a gas. Colder water typically holds more dissolved gases than warmer water. Significant increases or decreases may result in considerable gas exchange at the air-surface water interface regardless of the rate of metabolic processes occurring within the system. To account for temperature differences in ocean surface waters, Takahashi et al. (2002) developed a method for distinguishing the biological effect (i.e. photosynthesis and respiration) from the temperature effect. During the 2016 field sampling season, the range in temperature (9.22 ^{o}C to 20.55 ^{o}C) for the western region of Lake Superior suggests temperature may have an impact on pCO_2 in surface water.

In separating the influence of temperature from all other influences, such as biological factors, the approach outlined by Takahashi et al. (2002) was used. In order to do use this approach, the isochemical effect of temperature on freshwater pCO_2 must first be determined.

$$\partial \ln(pCO_2) / \partial T \quad (20)$$

where, ∂T, is change in temperature (^{o}C) and, $\partial \ln(pCO_2)$, is the change in the natural log of pCO_2 for the 2016 field season. Atilla et al. (2011) used a similar approach to distinguish between the temperature and biological effects on pCO_2 in offshore Lake Superior. They estimated the coefficient for Lake Superior by calculating pCO_2 across ranges of temperatures, total DIC concentrations, and alkalinity representative of the lake. The coefficient they calculated from

equation 19, 0.038 $^{o}C^{-1}$was considered to be constant and independent of temperature, salinity, and alkalinity, and used to correct for the effect of temperature in Lake Superior.

To remove the temperature effect and yield biologically-driven shifts in pCO_2, observed pCO_2 values were normalized to a constant temperature of 15.92 ^{o}C, the mean temperature in this region for the 2016 field season, using the following formula (Takahashi et al., 2002):

$$pCO_2 \text{ at } T_{mean} = pCO_{2(obs)} * \exp[0.038* (T_{mean} - T_{obs})] \quad (21)$$

where, T, is the temperature (^{o}C), and the subscripts "mean" and "obs" indicate the mean over the sampling season and observed value for a given time and location. To assess changes in pCO_2 at the surface primarily driven by changes in temperature, the following formula was used:

$$pCO_2 \text{ at } T_{obs} = pCO_{2(mean)} * \exp[0.038* (T_{obs} - T_{mean})] \quad (22)$$

where mean 2016 values for temperature, T_{mean}, and pCO_2 , $pCO_{2(mean)}$, were 15.92^{o}C and 356.5 ppm; respectively. The resulting values from equation 20 indicate changes in pCO2 that would be expected only based on the warming and cooling trend of Lake Superior over the summer and into the fall, disregarding the biological effect. A regression analysis between the observed pCO_2 and each of its components (biologically- or temperature-driven) was used to assess which component exhibited the most influence over nearshore surface pCO_2variability.

Results

Spatiotemporal Variability in pCO_2 & O_2 % Saturation

pCO_2 and O_2 % saturation exhibited substantial spatial (vertical and horizontal) and temporal variability over the 2016 field sampling season (Fig. 3.3 and Fig. 3.4). During the 2016

field season, atmospheric pCO_2 ranged between 386.0 ppm and 417.2 ppm. On June 23rd, pCO_2 at the surface was undersaturated with respect to the air (311.8 ppm ± 22.0 ppm). Within the epilimnion, pCO_2 ranged between 282.1 ppm and 400.5 ppm, with a mean value of 357.5 ppm. Along the surface, pCO_2 was lower close to shore (282.1 ppm) and increased with distance offshore to a maximum of 400.5 ppm. Near the shoreline, the water column was oversaturated with O_2 (108.6 %) and decreased with distance offshore (100.6%). This pattern in O_2 % saturation inversely mirrored that of pCO_2. Beneath the thermocline, pCO_2 increased as expected due to the colder water and potential organic matter decomposition within the hypolimnion, creating a vertical gradient in pCO_2. Mean pCO_2 within the hypolimnion on June 23rd was 624.8 ppm, and reached a maximum of 815.8 ppm at a depth of 30 m about 11 km offshore. On average, the entire nearshore water column was supersaturated with O_2 (101.7% ± 3.7%) on June 23rd. Although the majority of the nearshore was supersaturated with O_2, at the furthest offshore location below 20 m in depth O_2 was below saturation (95.7%).

A similar spatial pattern in pCO_2 was observed on July 7th. Again, the surface water was undersaturated with respect to the atmosphere, and surface pCO_2 increased further offshore. There was no significant variability in O_2 % saturation on July 7th. The nearshore water column was saturated with O_2 (100.1% ± 0.8%). On July 28th, two weeks after the large storm event, the epilimnion was still undersaturated (332.0 ppm ± 22.1 ppm); however, in contrast to the increasing nearshore-offshore trend exhibited on June 23rd and July 7th, pCO_2 decreased with distance offshore. The epilimnion was supersaturated in O_2 (106.1% ± 1.5%) with a maximum between 0 and 2.67 km offshore (111.8%). Within the nearshore, mean pCO_2 was 351.9 ppm and decreased to a minimum of 302.5 ppm at the furthest extent offshore. Interestingly, close to shore below the thermocline pCO_2 was significantly above saturation (574.9 ppm ± 80.9 ppm). This

spike in pCO_2 below the thermocline corresponded to a substantial decrease in O_2 % saturation (98.1% ± 0.03%). Also, at the furthest extent offshore, pCO_2 was undersaturated below the thermocline (305.5 ppm ± 19.0 ppm). Within this area offshore, supersaturation of O_2 (105.4% ± 0.2%) was also apparent. This region of undersaturation in pCO_2 and supersaturation of O_2 offshore happened to coincide with an area of increased chl*a* (Fig. 2.22; C). A minimum pCO_2 of 278.3 ppm was reached at 20 m in this region.

On August 17th, the surface mixed layer of Lake Superior was undersaturated to a greater extent than on July 28th (235.3 ppm ± 13.4 ppm). Supersaturation of O_2 was also greater in comparison to that of July 28th (108.5 % ± 1.2 %). At the surface, mean pCO_2 was higher close to shore (254.4 ppm) and decreased offshore, reaching a minimum of 218.1 ppm at 8.25 km offshore. In comparison to July 28th, there was no increase in pCO_2 at the bottom within the nearshore zone on August 17th. However, a noticeably decrease in pCO_2 was still present furthest offshore (240.8 ppm ± 40.7 ppm). A corresponding increase in O_2 % saturation was present within the same region offshore (109.0 % ± 0.3 %). On August 17th, this region of undersaturation decreased in depth to encompass the area between 5 and 15 m. In contrast to July 28th, the minimum reached in this area was much lower (189.2 ppm) and occurred at 10 m. Again, this region of undersaturation in pCO_2 appeared to coincide with an increase in chla (Fig. 2.23; A).

The pattern of pCO_2 undersaturation within the epilimnion persisted into September (287.2 ppm ± 35.3 ppm). Supersaturation of O_2 within the epilimnion was clearly observable (102.2 % ± 0.9 %). Again, pCO_2 decreased with distance offshore reaching a minimum of 244.0 ppm at 10.79 km offshore. Within the nearshore zone, pCO_2 in the epilimnion was slightly higher than June 23rd, July 7th, and August 17th but lower than July 28th (317.8 ppm ± 11.0 ppm).

On September 21st, over a month after August 17th, remnants of severe pCO_2 undersaturation at the furthest location offshore were still apparent, however, the range in depth had decreased (5 – 10 m). There was a corresponding increase in O_2 % saturation in the same area offshore (103.6 % ± 0.2 %). Within this region, mean pCO_2 was 272.3 ppm ± 5.6 ppm.

Finally, on October 25th, the entire water column along the nearshore-offshore transect was oversaturated in pCO_2 with respect to the atmosphere (461.1 ppm ± 16.2 ppm). Not only is the water column oversaturated with pCO_2, it is also relatively uniform in terms of pCO_2, which suggests much of the excess pCO_2 that was present in the hypolimnion over the course of the summer has been released. The lack of a thermocline (Fig. 2.3-9) suggests the disappearance of a strong density gradient capable of constraining elevated pCO_2 within the hypolimnion. A similar, albeit inverse pattern was observed in O_2 % saturation on October 25th. The entire water column was undersaturated in O_2 (97.4 % ± 1.5 %) and was relatively uniform.

The temporal shifts in pCO_2 at the surface of nearshore Lake Superior are further illustrated in Fig. 3.5. On average, mean pCO_2 at the surface ranged from between 280 ppm and 360 ppm. However, immediately following the storm event pCO_2 increased significantly. On July 15th, mean pCO_2 at the surface was 467.9 ppm ± 19. 1 ppm, and decreased over the next two weeks to reach a mean of 332.0 ppm ± 22.1 ppm on July 28th. At the surface, pCO_2 continued to decrease in the month following the storm event, eventually reaching a low point of 270.3 ppm ± 24.9 ppm on August 17th. Following the low point on August 17th, pCO_2 at the surface began rise again, and eventually peaked at 455.0 ppm ± 11.4 ppm in October. It is important to note, that on July 15th only surface water samples and pH data were collected because a sonde with pH sensor was not available for profiling.

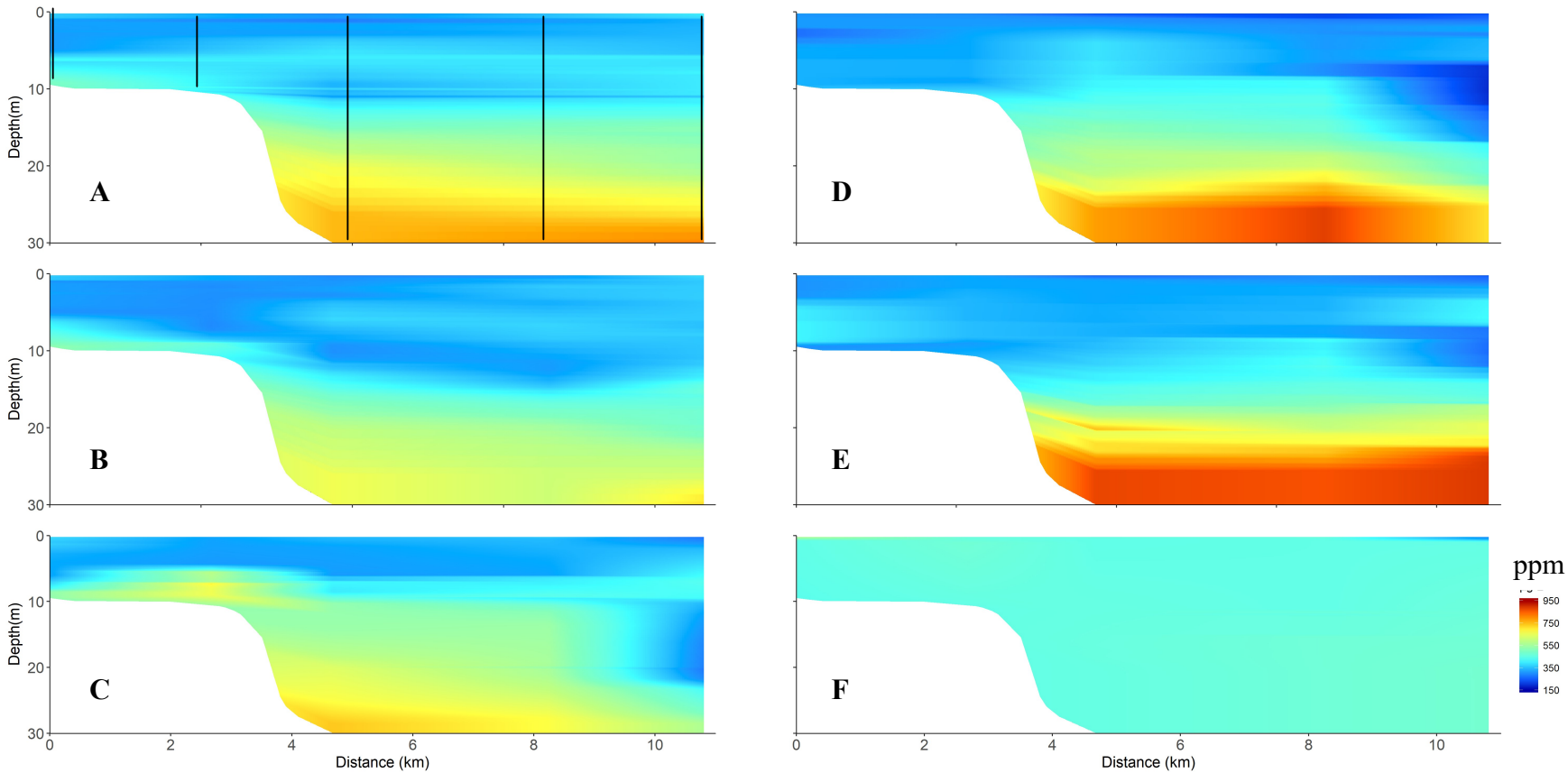

Figure 3.3: Vertical profiles of pCO_2(ppm) for specific sampling days; (A) June 23rd, (B) July 7th, (C) July 28th, (D) August 17th, (E) September 21st, and (F) October 25th. The vertical black lines represent the location of vertical sonde profiles.

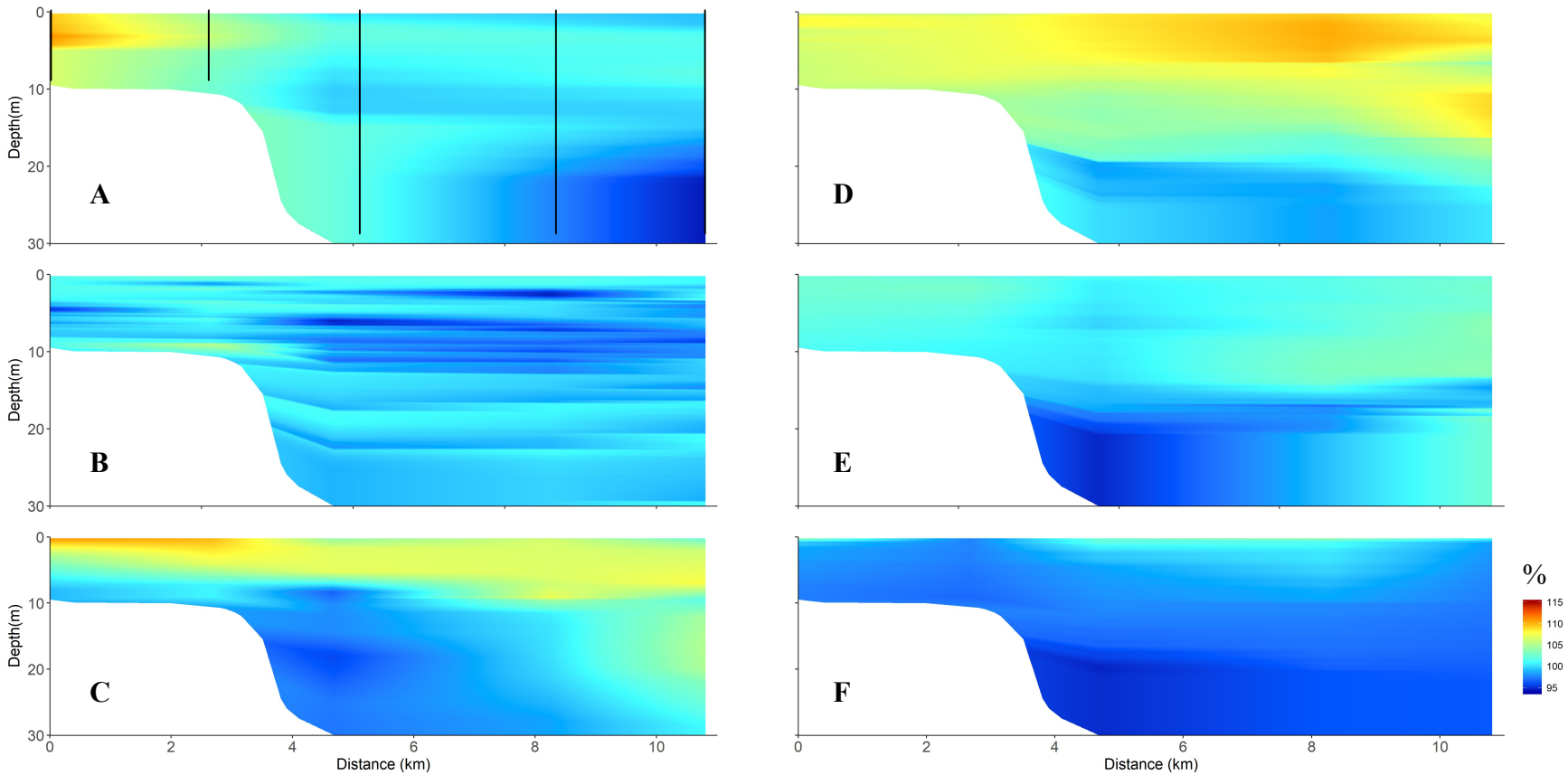

Figure 3.4: Vertical profiles of O_2 percent saturation for specific sampling days; (A) June 23rd, (B) July 7th, (C) July 28th, (D) August 17th, (E) September 21st, and (F) October 25th. The vertical black lines represent the location of vertical sonde profiles.

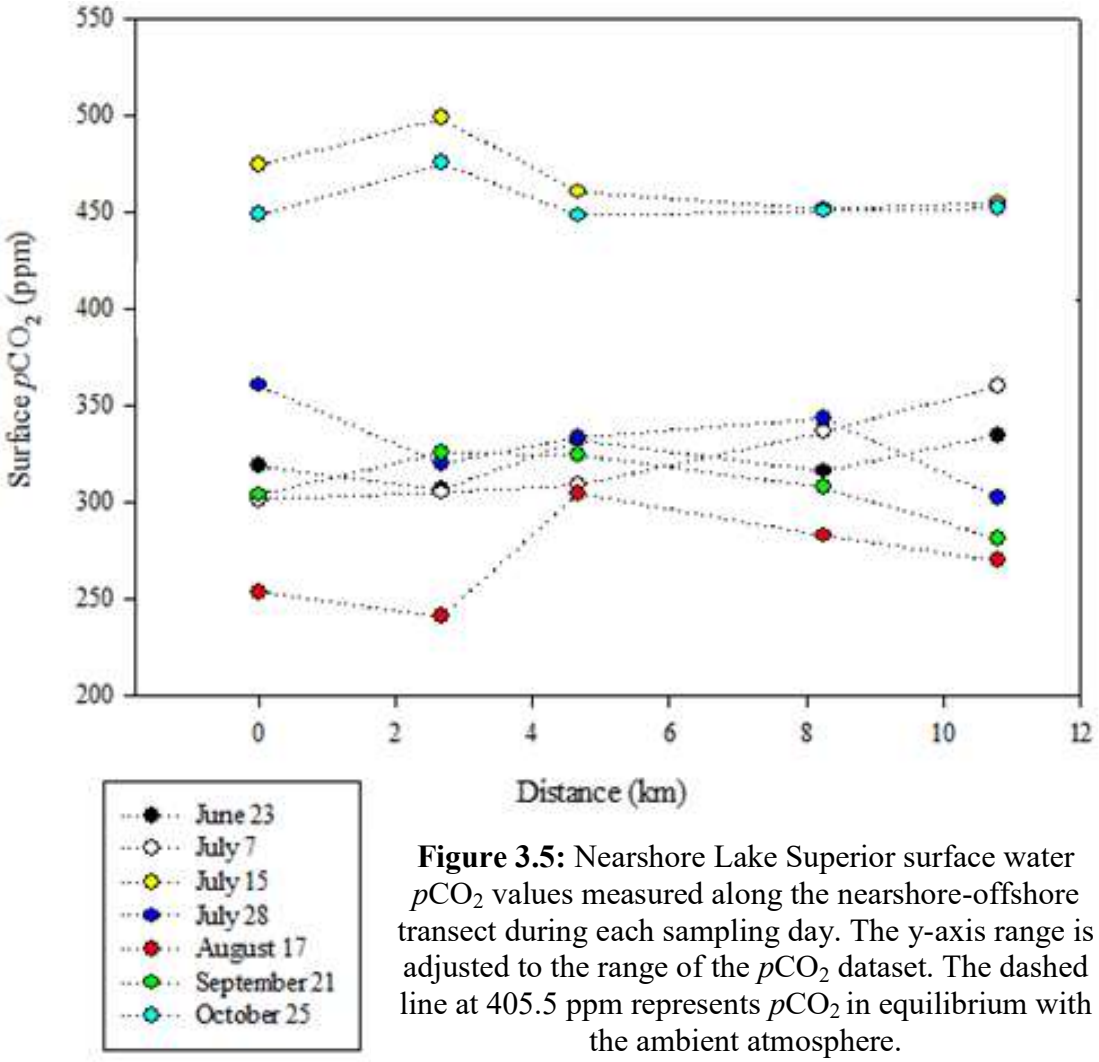

Figure 3.5: Nearshore Lake Superior surface water pCO_2 values measured along the nearshore-offshore transect during each sampling day. The y-axis range is adjusted to the range of the pCO_2 dataset. The dashed line at 405.5 ppm represents pCO_2 in equilibrium with the ambient atmosphere.

Lake-Atmosphere CO_2 & O_2 Flux

The flux of CO_2 from the surface of Lake Superior to the atmosphere ranged from -15.4 to 7.7 mmol m^{-2} d^{-1}, and averaged -2.7 mmol m^{-2} s^{-1} ± 5.8 mmol m^{-2} d^{-1} (n = 35) over the course of the 2016 field season. Only two dates showed net evasion of CO_2 from the lake to the atmosphere (i.e. positive values), July 15th and October 25th. The net evasion of CO_2 out of the lake on July 15th occurred immediately after the storm event, and during the period the surface plume reached maximum extent (Fig. 2.9). Based on Fig. 3.6, the degree to which the nearshore zone shifts to net heterotrophy following the storm is much less than the shift observed on October 25th. In late October, the lake turned over (Fig. 2.16) and so much of the excess CO_2 within the hypolimnion would have reached the surface accounting for the apparent larger shift to heterotrophy.

An ANOVA showed that the variation in CO_2 flux over time is statistically significant ($F_{6,6}$= 55.3, p = 1.4 x 10^{-13}). As expected, post hoc comparisons using Tukey HSD show that the mean flux on July 15th (1.4 mmol m^{-2} d^{-1} ± 0.4 mmol m^{-2} d^{-1}) and October 25th (6.4 mmol m^{-2} d^{-1} ± 0.7 mmol m^{-2} d^{-1}) were different than that of June 23rd, July 7th, July 28th, August 17th, and September 21st. Although the net flux from the atmosphere to the lake appeared larger on August 17th relative to some of other days (Fig. 3.6), there was no statistical difference (p>>0.01). Over the 2016 field season flux of CO_2 into the lake was much greater on average (-5.6 mmol m^{-2} s^{-1}) than the flux out of the lake (3.9 µmol m^{-2} s^{-1}).

For O_2, the flux from the surface of Lake Superior to the atmosphere ranged from -64.6 to 59.7 mmol m^{-2} d^{-1}, and averaged 12.3 mmol m^{-2} d^{-1} ± 33.8 mmol m^{-2} d^{-1} (n = 35).The magnitude in O_2 flux was significantly larger than that of CO_2. There was net flux of O_2 from the lake to the atmosphere (i.e. positive values) over the course of the 2016 field season. An ANOVA showed

that temporal changes in O_2 flux over the course of the field season were statistically significant ($F_{6,6}$= 69.2, p = 9.7 x 10^{-15}). Post hoc comparisons using Tukey HSD show that the mean flux into the lake on July 15th (-11.6 mmol m^{-2} d^{-1} ± 3.3 mmol m^{-2} d^{-1}) and October 25th (-46 mmol m^{-2} d^{-1} ± 18.6 mmol m^{-2} d^{-1}) was statistically different and opposite in direction compared to the other sampling dates.

The efflux of O_2 and influx of CO_2 at the lake surface is indicative of net autotrophy. For the nearshore ecosystem adjacent to the Apostle Islands archipelago, the relationship between net lake – atmosphere flux of O_2 and CO_2 is illustrated in Fig. 3.6. The nearshore zone of western Lake Superior was net autotrophic for every sampling day except for July 15th and October 25th. The sudden shift towards net heterotrophy on July 15th was likely a response to the storm event on July 12th. About two weeks later, however, the nearshore zone shifted back to a net autotrophic system as evident Fig. 3.6. The shift towards net autotrophy increased even further a month after the storm event. Finally, on October 25th, the nearshore zone shifted back towards apparent net heterotrophy, albeit at a larger scale than July 15th. However, the shift in October is most likely due to upwelling of cold, CO_2-rich hypolimnetic water as demonstrated in Fig. 3.7.

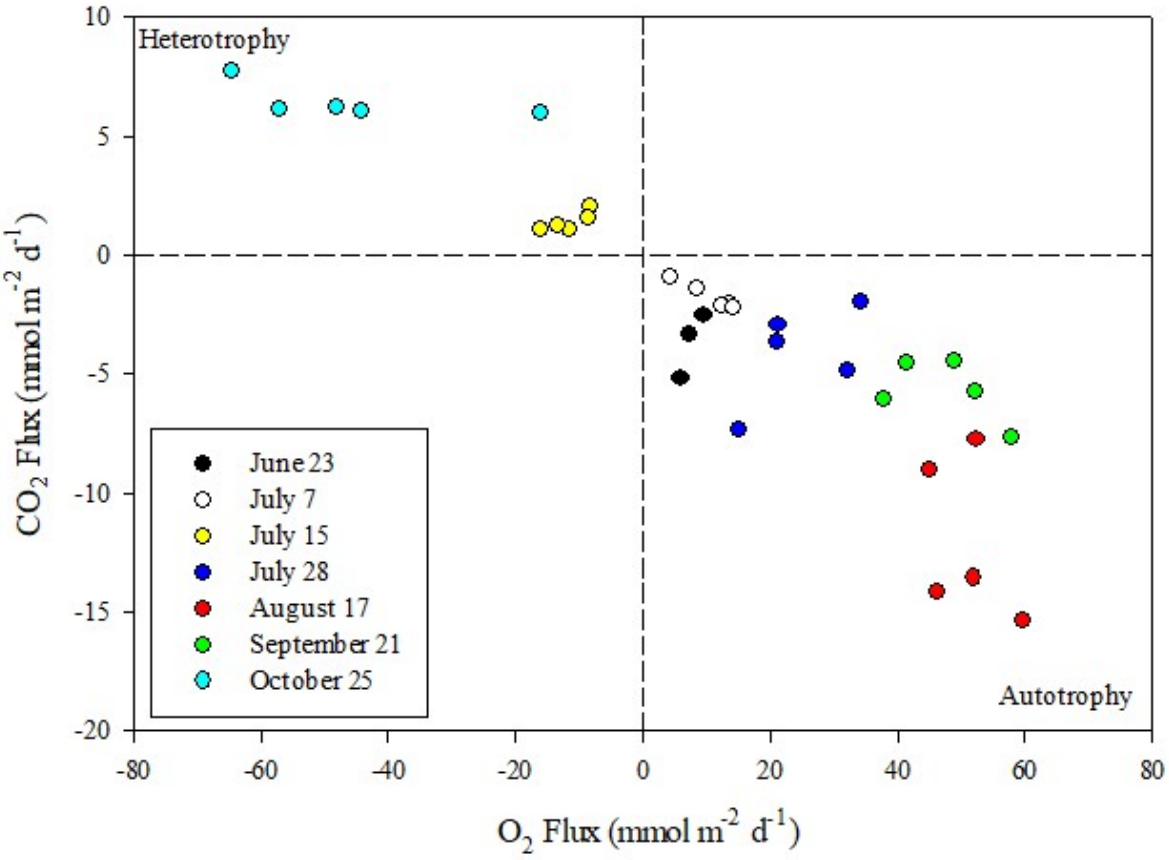

Figure 3.6: CO_2 and O_2 lake – atmosphere flux biplot illustrating temporal shifts in surface mixed layer metabolism. The dotted lines represent equilibrium conditions between the lake surface and atmosphere for each dissolved gas. Positive values indicate efflux of the respective gas, whereas negative values represent influx to the lake. Note that the standing stock of dissolved O_2 is larger in comparison to dissolved CO_2. Therefore, the range of O_2 flux is much greater than that of CO_2.

Temperature-Biological Effect on pCO_2

Trends in pCO_2 generally follow those of the biologically-driven component (Fig. 3.7). Early in the summer (i.e. June 23rd and July 7th) and near the end of October, variations in observed surface pCO_2 were the approximate difference between those of the biological component and the temperature-driven component of pCO_2. This may be a result of the upwelling of cold, CO_2-rich water. Interestingly, in the two months following the episodic storm event, anomalies in observed pCO_2 are no longer the approximate difference between the biological and temperature component suggesting a much greater contribution of the biological component to surface pCO_2.

Following the episodic storm event, surface pCO2 driven by non-temperature factors alone decreased by about a net 300 ppm from July 15th to August 17th. This decrease approximates the net biological effect on surface pCO_2. The warming water over the course of the summer resulted in a net increase of about 100 ppm, which describes the net temperature effect on surface pCO_2. This suggests that the estimated biological drawdown following the influx of nutrients after the storm event (300 ppm) is compensated somewhat by an effect of rising temperature (100 ppm) to yield an observed pCO_2 of about 250 ppm in August. This approximation based on the biological and temperature components is very close to the actual pCO_2 at the surface (270.3 ppm ± 24.9 ppm).

Regression analysis between observed surface pCO_2 and the biological and temperature components suggests strong influence on the variability in pCO_2 following the storm event by non-temperature, or biological, factors (Fig. 3.8). There was a strong correlation between observed surface pCO_2 and its biological component for all observations (n = 33) made in 2016 ($r^2 = 0.84$). The lack of correlation between surface observed pCO_2 and the temperature

component ($r^2 = 0.49$) also suggests that the variability in surface pCO_2 following the storm event was primarily driven by biological factors.

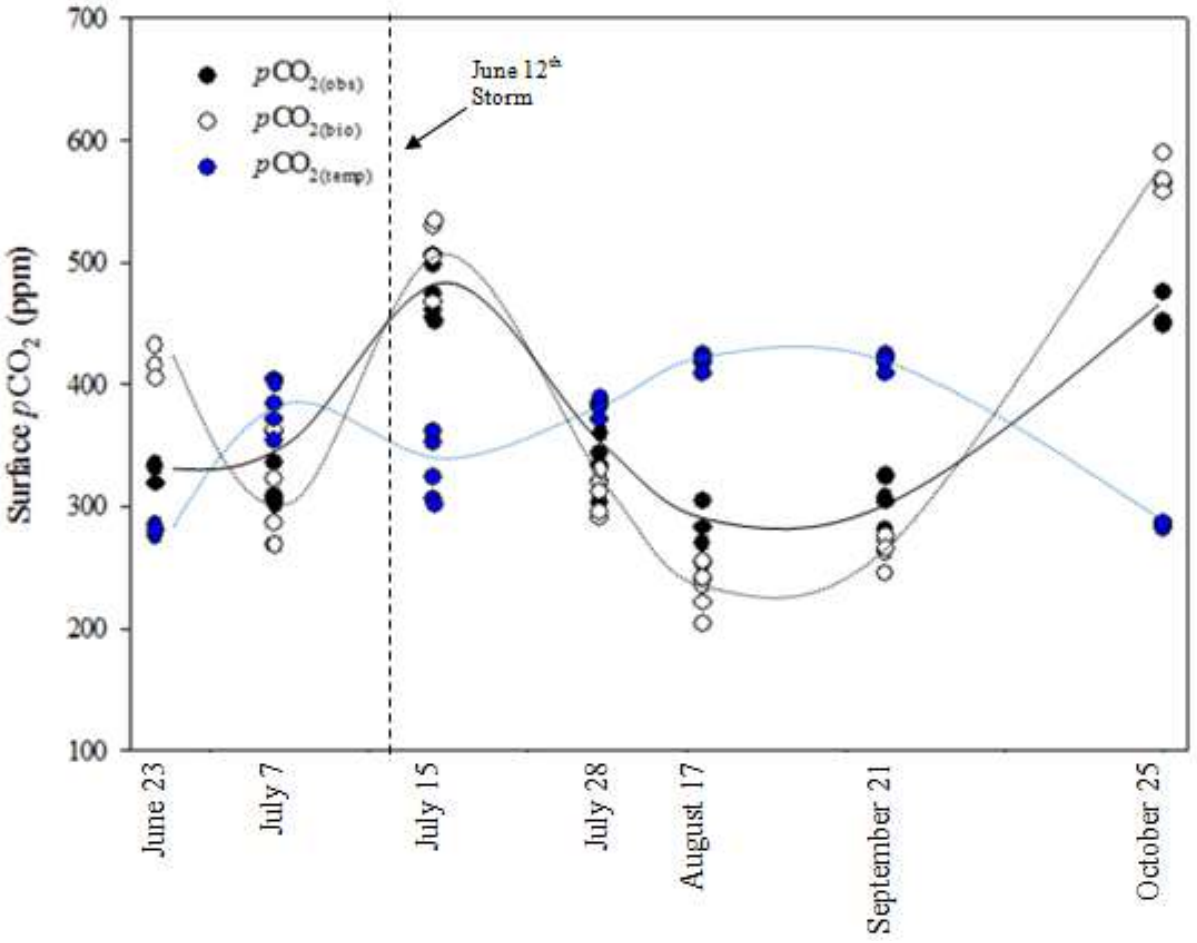

Figure 3.7: Surface observed pCO_2 and its components; the black circles refer to observed pCO_2, the white circles to the biological component, and the blue circles represent the temperature-driven component of pCO_2.

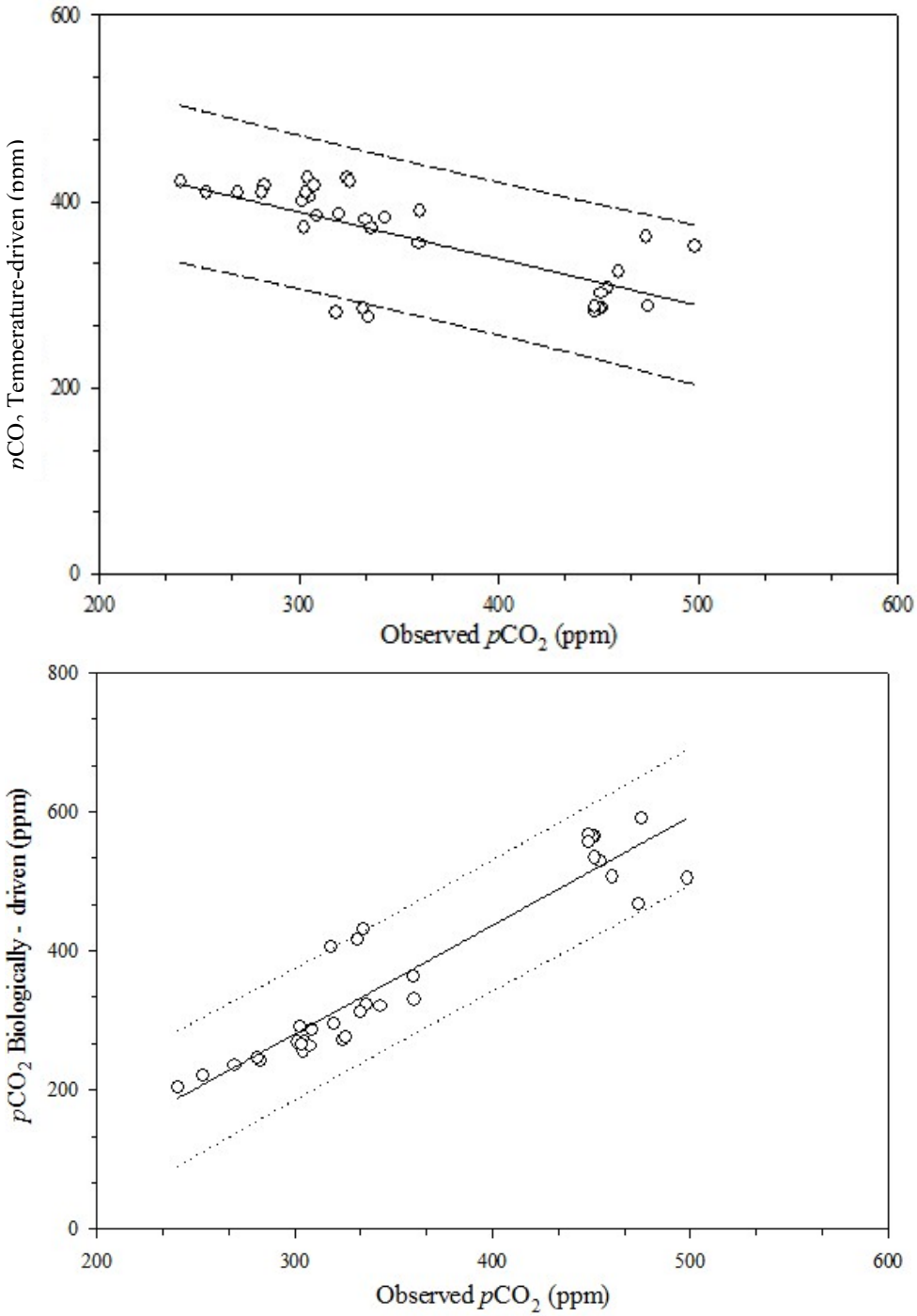

Figure 3.8: Linear relationships between observed pCO_2 and (A) the biological component and (B) the temperature component. The solid black line represents the general trend. The 90% confidence interval for the dataset is represented by the dashed, black lines.

Discussion

Overall, the results presented here suggest riverine nutrient and organic carbon loads following a storm event drive shifts in community metabolism within nearshore Lake Superior. Lake systems with high TDP and low DOC concentrations tend to be more productive, while lakes with low TDP and high DOC tend to be dominated by respiration (Cole et al., 2000; Hanson et al., 2003). Following the major storm event, both TDP and DOC increased significantly; for example, on July 28th, total water column concentrations of TDP and DOC approximately doubled with respect to baseline concentrations in the early summer and fall. The development of distinct horizontal and vertical gradients in TDP and DOC within the nearshore zone following the storm event might be expected to result in spatiotemporal differences in metabolism. The nearshore zone of Lake Superior is large in comparison to the lakes studied by Cole et al. (2000) and Hanson et al. (2003). Therefore, the distinct TDP and DOC gradients may result in localized metabolic responses within the nearshore. The depth and stability of thermal stratification, river intrusion flowpath, and hydrodynamics effectively control localized metabolic response.

Immediately following the plume, the nearshore zone shifted from a net autotrophic system to a net heterotrophic system on July 15th indicating greater community respiration relative to primary production. Although DOC increased to a maximum of 3.9 mg L^{-1} and it decreased far quicker than TDP, Prairie et al. (2002) and Hanson et al. (2003) show that net heterotrophy does not occur in temperate lakes unless the DOC concentration is >6 mg L^{-1}.The scale of the net evasion of CO_2 to the atmosphere on this day was relatively small suggesting that respiration may not have increased dramatically, but rather there was a significant enough reduction in community primary production that resulted in a efflux of CO_2 to the atmosphere.

The extremely turbid water as a result of a substantial surface plume (Fig. 2.9; B) may have inhibited the ability of autotrophs to photosynthesize due to decreasing light intensity. Minor et al. (2014) described a similar trophic response to a major river plume in nearshore Lake Superior.

Their research suggested that close to the Duluth-Superior harbor, phytoplankton transitioned from nutrient – to light – limitation under turbid, surface plume conditions. By the time the water column cleared enough to promote photosynthesis, TDP concentrations had returned to concentrations typical of Lake Superior. Therefore, primary production did not increase in response to episodic riverine loading. Anecdotal evidence, however, suggests areas in close proximity to the Apostle Islands exhibited an autotrophic response to episodic riverine loading of nutrients (Larson et al., 2012). Larson et al. (2012) reported the presence of a cyanobacteria bloom near the Apostle Islands in response to an episodic river plume in June of 2012. Remote sensing imagery (Fig. 2.9) indicates that the turbid surface plume was present near the Duluth-Superior harbor for a longer period of time than near the Apostle Islands during the present study. It is also evident there is a temporal mismatch between the nutrient availability and light levels, where TDP remains relatively high and surface turbidity decrease within the month following the storm event. The observed asynchrony in the decrease of surface turbidity and TDP suggests there may be a temporal lag in the phytoplankton response to elevated nutrient availability, which is supported by the low surface pCO_2 values observed over two weeks after the storm event (Fig. 3.5).

The substantial decrease in surface pCO_2 following July 15th within the nearshore zone suggests an increase in primary production or the advection of low pCO_2 water from another region of the lake. Immediately following July 15th the nearshore zone shifted back towards a net

autotrophic system, further evident by comparisons between lake – atmosphere CO_2 and O_2 flux. In proximity to the Apostle Islands, the surface plume dissipated quickly, thereby increasing the availability of light while TDP concentrations were still relatively high. On July 28th, surface pCO_2 decreased by about 100 ppm, relative to July 15th, and the surface mixed layer was significantly oversaturated with O_2. About a month later, primary productivity increased even more as evident by another decrease in surface pCO_2 and an associated increase in O_2 % saturation. The further increase in the rate of CO_2 flux into the lake and associated O_2 flux out of lake on August 17th suggests increasing primary production within the nearshore zone. Prior to the episodic surface plume and accompanying riverine loading, the biological and temperature effect on surface pCO_2 were approximately equal. However, after the storm event, the biological drawdown controlled the variability in pCO_2 to a greater extent than temperature.

Below the surface within the nearshore, vertical and horizontal gradients in TDP and DOC resulted in localized spatiotemporal variability in metabolism. On July 28th, elevated pCO_2 was evident near the bottom of the lake between 0 and 2.67 km offshore, which was validated by an associated undersaturation of O_2 within the same area. DOC within this area decreased sharply after July 28th, while phosphorus remained high, suggesting remineralization of allochthonous DOC occurred near the lake bottom, below the thermocline thereby releasing CO_2 to the surrounding water. Similarly, Hanson et al. (2003) illustrated a strong correlation between allochthonous DOC inputs and increased respiration (i.e. CO_2 production) in small temperate lakes. Interestingly, further offshore DOC was relatively high along 10 m in depth; however, there were no other localized increases in community respiration as indicated by the pCO_2 profile. Following the storm event and subsequent river loading of TDP and DOC, increases in community respiration were evident by the shift towards net heterotrophy of the nearshore zone

on July 15th. The lack of sustained heterotrophy and the apparent shift two weeks later to net autotrophy suggests that the majority of the plume was replaced by less turbid offshore water, thereby increasing water clarity and primary production within the nearshore.

At 10 m in depth, concentrations of TDP were relatively high in comparison to other depths. On July 28th, at the furthest extent offshore (> 11 km) there was subsurface spike in primary production at 10 m, which also corresponded to a region of high Chl*a* concentration. This increase in primary production was evident by a decrease in pCO_2 and a corresponding area of O_2 supersaturation. Not only was this region of increased primary production apparent on July 28th, a month after the initial river loading of TDP increased primary productivity between 5 and 15 m within the offshore Chl*a* spike was evident in the pCO_2 and O_2 % saturation profiles. Therefore, surface measurements of pCO_2 and lake – atmosphere CO_2 and O_2 flux estimates tell only part of the story. Localized subsurface increases in primary productivity and respiration are apparent. The subsurface variability in community metabolism varies by distance offshore and depth, and is often associated with vertical and horizontal TDP and DOC gradients.

As a whole, Lake Superior has been shown to be relatively heterotrophic. Urban et al. (2004) illustrate the consistent supersaturation and net efflux of CO_2 within the nearshore along the Keweenaw Peninsula. The partial pressure of CO2 determined by Urban et al. was consistently above 400 ppm. Cotner et al. (2004) also describe the lake as a whole as net heterotrophic by illustrating that on average respiration dominates over primary production in Lake Superior. It is important to note, however, that neither of these studies examined the metabolic response of the lake following an episodic storm and flood event. Therefore, although in the long-term the lake as a whole may be heterotrophic this may shift in response to increased tributary loading.

Within western Lake Superior during the summer, Russ et al. (2004) showed a persistence of net autotrophy (whereas the rest of Lake Superior remains net heterotrophic) in proximity of the Duluth, MN suggesting increased primary productivity was driven by river nutrient loading. However, as evident by the marked shift towards net heterotrophy seen following the development of a surface plume and the work of Minor et al. (2014), episodic plume events may decrease autotrophic production by reducing light intensity. Episodic inflows rich in CDOM and red clay complexes may suppress primary production while simultaneously resulting in slight increases in respiration within the nearshore ecosystem. Once the surface plume dissipates and the water column clears the influx of riverine nutrients results in an increase in community primary production. Large storm events have a short-term effect of increasing heterotrophy. This effect appears to be due more to decreased water clarity than to organic carbon loading. By contrast, over the long-term (i.e. greater than 2 weeks), large storm events appear to promote nearshore autotrophy.

Chapter 4: General Conclusions

As the interface between the terrestrial landscape and the open lake, nearshore zones play an important role in modulating whole-lake response to inputs of nutrients and energy from the watershed. Nearshore zones of large lakes are regions of substantial temporal and spatial heterogeneity. This heterogeneity stems from the juxtaposition of a terrestrial environment with an aquatic environment, and the complexity of hydrodynamics within the nearshore zone. The proximity of the nearshore zone to the terrestrial environment makes them susceptible to anthropogenic impacts (Chu et al., 2014) and variations in land-use (Yurista et al., 2011). Many environmental variables drive spatiotemporal variability within the nearshore zone, including temperature regimes, light intensity, water and soil chemistry, hydrodynamics, episodic inflow events, and the quality and quantity of inflowing nutrients and energy to name a few (Strayer and Findlay, 2010). The connectivity, and thereby the influence of the nearshore zone on the whole-lake, is large dependent on general circulation patterns (Rao and Schwab, 2007).

The dynamics of nutrients and energy within offshore waters are primarily driven by mechanisms of internal cycling and the lateral transfer between the nearshore and offshore zones. Despite the relatively low watershed to surface area ratio of large lakes, river influence, and thereby, terrestrial influence, on large lake nutrient and organic carbon cycling can be significant. In Lake Baikal, the Selenga River accounts for over 50% of the nutrient load (Müller et al., 2005) and often results in spatial variations in phytoplankton biomass (Popovskaya, 20000 and primary productivity (Straškrábová et al., 2005). Straškrábová et al. (2005) illustrated spatial differences in net ecosystem production between the northern and southern basins of Lake Baikal. For reference, the southern basin of the lake is the receiving basing for the inflowing Selenga River. Annual primary production in the southern basin was 1,730 mmol C m^{-2} $year^{-1}$,

whereas annual production was lower in the more secluded northern basin (1,220 mmol C m^{-2} $year^{-1}$). This suggests riverine input of nutrients from the Selenga River subsidizes the nutrient pool in the southern basin resulting in annually greater autotrophic production.

For southern Lake Michigan, Biddanda and Cotner (2002) reported that terrestrial nutrient and organic carbon subsidies introduced by riverine inflow supported approximately 10% of the organic carbon remineralized by heterotrophic bacteria, and 20% of phosphorus associated with autotrophic primary production. Therefore, allochthonous input of phosphorus via rivers appears to have a larger influence on community metabolism relative to inputs of organic carbon. A similar conclusion was arrived at in this study, based on the metabolic patterns and chemical dynamics of nearshore Lake Superior. Enrichment experiments conducted by Johengen et al. (2008) suggest riverine input stimulates autotrophic production to a greater extent than heterotrophic bacterial production. Johengen et al. (2008) found that the ratio of bacterial to primary production in ambient lake water was 0.23, and decreased to approximately 0.10 with the addition of river water.

As mentioned, shifts towards net autotrophy in western Lake Superior relative to the rest of the lake are clearly apparent (Russ et al., 2004; Urban et al., 2005). Both Russ et al. (2004) and Urban et al. (2005) conclude that this shift was in response to increased river input of nutrients. The study conducted by Russ et al. (2004) illustrated respiration to photosynthesis ratios (R: P) for offshore Lake Superior to be generally greater than 1, while an average R: P ratio of 0.6 was determined for western Lake Superior. The watershed of western Lake Superior drains some of the largest tributaries of the lake, such as the St. Louis and Nemadji Rivers. The research presented here also suggests the ecosystem is net autotrophic during the summer, and variations in magnitude of autotrophic primary production are heavily influenced by riverine

input. Evidence of increased primary production in response to point-source inputs of nutrients via rivers is also apparent in other regions of Lake Superior, such as near the mouth of the Ontagonon River along the Keweenaw Peninsula (Auer and Bub, 2004).

A large body of evidence suggests, despite the size of many large lakes, whole-lake variability in metabolic processes in response to river loading of nutrients and organic carbon is apparent. Therefore, the lateral transfer of terrestrially-derived nutrients and organic carbon between the nearshore and offshore zones is extremely important in subsidizing whole-lake food webs.

REFERENCES

Ahmed, S., Troy, C. D., & Hawley, N. (2014). Spatial structure of internal Poincaré waves in Lake Michigan. *Environmental Fluid Mechanics*, *14*(5), 1229-1249.

Allan, J. D., P. B. McIntyre, S.D.P Smith, B.S. Halpern, G.L. Boyer, A. Buchsbaum, G.A. Burton, L.M. Campbell, W.L. Chadderton, J.J.H Cibrowski, P.J. Doran, T. Eder, D.M. Infante, L.B. Johnson, C.A. Joseph, A.L. Marino, A. Prusevich, J.G. Read, J.B. Rose, E.S. Rutherford, S.P. Sowa, & Steinman, A.D. (2013). Joint analysis of stressors and ecosystem services to enhance restoration effectiveness. *Proceedings of the National Academy of Sciences, 110*(1), 372-377.

Alldredge, A. L., Cowles, T. J., MacIntyre, S., Rines, J. E., Donaghay, P. L., Greenlaw, C. F., ... & Zaneveld, J. R. V. (2002). Occurrence and mechanisms of formation of a dramatic thin layer of marine snow in a shallow Pacific fjord. *Marine Ecology Progress Series*, *233*, 1-12.

Anderson, J. D., C.H. Wu, & Schwab, D.J. (2015). Wave climatology in the Apostle Islands, Lake Superior. *Journal of Geophysical Research: Oceans*, *120*(7), 4869-4890.

Atilla, N., McKinley, G. A., Bennington, V., Baehr, M., Urban, N., DeGrandpre, M., Desai, A. R.,& Wu, C. (2011). Observed variability of Lake Superior pCO2. *Limnology and Oceanography*, *56*(3), 775.

Auer, M. T., & Bub, L. A. (2004). Selected features of the distribution of chlorophyll along the southern shore of Lake Superior. *Journal of Great Lakes Research*, *30*, 269-284.

Austin, J. (2013). Observations of near-inertial energy in Lake Superior. *Limnology and Oceanography*, *58*(2), 715-728.

Austin, J. A., & Colman, S. M. (2007). Lake Superior summer water temperatures are increasing more rapidly than regional air temperatures: A positive ice-albedo feedback. *Geophysical Research Letters*, *34*(6).

Austin, J., & Colman, S. (2008). A century of temperature variability in Lake Superior. *Limnology and Oceanography*, *53*(6), 2724-2730.

Azam, F., Fenchel, T., Field, J. G., Gray, J. S., Meyer-Reil, L. A., & Thingstad, F. (1983). The ecological role of water-column microbes in the sea. *Marine ecology progress series. Oldendorf*, *10*(3), 257-263.

Baehr, M. M. & McManus, J. (2003). The measurement of phosphorus and its spatial and temporal variability in the western arm of Lake Superior. *Journal of Great Lakes Research*, *29*(3), 479-487.

Barbiero, R. P., & Tuchman, M. L. (2001). Results from the US EPA's biological open water surveillance program of the Laurentian Great Lakes: I. Introduction and phytoplankton results. *Journal of Great Lakes Research*, *27*(2), 134-154.

Barbiero, R. P., & Tuchman, M. L. (2004). The deep chlorophyll maximum in Lake Superior. *Journal of Great Lakes Research*, *30*, 256-268.

Beletsky, D., Saylor, J. H., & Schwab, D. J. (1999). Mean circulation in the Great Lakes. *Journal of Great Lakes Research*, *25*(1), 78-93.

Bennington, V., McKinley, G. A., Kimura, N., & Wu, C. H. (2010). General circulation of Lake Superior: Mean, variability, and trends from 1979 to 2006. *Journal of Geophysical Research: Oceans*, *115*(C12).

Biddanda, B. A., & Cotner, J. B. (2002). Love handles in aquatic ecosystems: the role of dissolved organic carbon drawdown, resuspended sediments, and terrigenous inputs in the carbon balance of Lake Michigan. *Ecosystems*, *5*(5), 431-445.

Bocaniov, S. A., D. R. Barton, S. L. Schiff, & Smith, R. E. (2013). Impact of tributary DOM and nutrient inputs on the nearshore ecology of a large, oligotrophic lake (Georgian Bay, Lake Huron, Canada). *Aquatic sciences*, *75*(2), 321-332.

Bootsma, H. A., Hecky, R. E., Hesslein, R. H., & Turner, G. F. (1996). Food partitioning among Lake Malawi nearshore fishes as revealed by stable isotope analyses. *Ecology*, *77*(4), 1286-1290.

Bootsma, H. A., & Hecky, R. E. (2003). A comparative introduction to the biology and limnology of the African Great Lakes. *Journal of Great Lakes Research*, *29*, 3-18.

Bootsma, H. A., Hecky, R. E., Hesslein, R. H., & Turner, G. F. (1996). Food partitioning among Lake Malawi nearshore fishes as revealed by stable isotope analyses. *Ecology*, *77*(4), 1286-1290.

Boyce, F. M. (1974). Some aspects of Great Lakes physics of importance to biological and chemical processes. *Journal of the Fisheries Board of Canada*, *31*(5), 689-730.

Carter, C.H. & Haras, W.S. (1985). Great Lakes. In *The World's Coastline*, E.C.F. Bird & M.C. Schwartz, eds., pp. 253-260. New York: VanNostrand Reinhold.

Chapra, S. C., Dove, A., & Warren, G. J. (2012). Long-term trends of Great Lakes major ion chemistry. *Journal of Great Lakes Research*, *38*(3), 550-560.

Chen, C. C., Petersen, J. E., & Kemp, W. M. (2000). Nutrient uptake in experimental estuarine ecosystems: scaling and partitioning rates. *Marine Ecology Progress Series*, *200*, 103-116.

Christensen, J. H., & Christensen, O. B. (2003). Climate modelling: severe summertime flooding in Europe. *Nature*, *421*(6925), 805-806.

Chu, C., M.A. Koops, R.G. Randall, D. Kraus, & Doka, S.E. (2014). Linking the land and the lake: a fish habitat classification for the nearshore zone of Lake Ontario. *Freshwater Science*, *33*(4), 1159-1173.

Cole, J. J., Caraco, N. F., Kling, G. W., & Kratz, T. K. (1994). Carbon dioxide supersaturation in the surface waters of lakes. *Science-AAAS-Weekly Paper Edition*, *265*(5178), 1568-1569.

Cole, J. J., Pace, M. L., Carpenter, S. R., & Kitchell, J. F. (2000). Persistence of net heterotrophy in lakes during nutrient addition and food web manipulations. *Limnology and oceanography*, *45*(8), 1718-1730.

Corman, J. R., McIntyre, P. B., Kuboja, B., Mbemba, W., Fink, D., Wheeler, C. W., ... &Flecker, A. S. (2010). Upwelling couples chemical and biological dynamics across the littoral and pelagic zones of Lake Tanganyika, East Africa. *Limnology and Oceanography*, *55*(1), 214-224.

Cotner, J.B., B.A. Biddanda, W. Makino, & Stets, E. (2004). Organic carbon biogeochemistry of Lake Superior. *Aquatic Ecosystem Health & Management, 7*(4), 451-464.

Csanady, G. T. (1972). Response of large stratified lakes to wind. *Journal of Physical Oceanography*, *2*(1), 3-13.

Csanady, G. T. (2013). *Circulation in the coastal ocean* (Vol. 2). Springer Science & Business Media.

del Giorgio, P.A.& Peters, R. H. (1994). Patterns in planktonic P: R ratios in lakes: Influence of lake trophy and dissolved organic carbon. *Limnol. Oceanogr*, *39*(4), 772-787.

del Giorgio, P.A., J.J. Cole, &. Cembleris, A. (1997). Respiration rates in bacteria exceed phytoplankton primary production in unproductive aquatic ecosystems. *Nature, 385*(6612), 148-151.

del Giorgio, P. A., & Williams, P. J. L. B. (Eds.). (2005). *Respiration in aquatic ecosystems*. Oxford University Press, USA.

Dillon, P. J., & Rigler, F. H. (1974). The phosphorus-chlorophyll relationship in lakes. *Limnology and oceanography*, *19*(5), 767-773.

Eadie, B. J., Schwab, D. J., Johengen, T. H., Lavrentyev, P. J., Miller, G. S., Holland, R. E., ... & Hawley, N. (2002). Particle transport, nutrient cycling, and algal community structure associated with a major winter-spring sediment resuspension event in southern Lake Michigan. *Journal of Great Lakes Research*, *28*(3), 324-337.

Edsall, T. A., & Charlton, M. N. (1997). *Nearshore waters of the Great Lakes*. Environment Canada.

Falkowski, P. G., & Raven, J. A. (2013). *Aquatic photosynthesis*. Princeton University Press.

Fahnenstiel, G., Pothoven, S., Vanderploeg, H., Klarer, D., Nalepa, T., & Scavia, D. (2010). Recent changes in primary production and phytoplankton in the offshore region of southeastern Lake Michigan. *Journal of Great Lakes Research, 36*, 20-29.

Fietz, S., Kobanova, G., Izmest'eva, L., & Nicklisch, A. (2005). Regional, vertical and seasonal distribution of phytoplankton and photosynthetic pigments in Lake Baikal. *Journal of Plankton Research*, *27*(8), 793-810.

Frost, P. C., J. H. Larson, C. A. Johnston, K. C. Young, P. A. Maurice, G. A. Lamberti, & Bridgham, S. D. (2006). Landscape predictors of stream dissolved organic matter concentration and physicochemistry in a Lake Superior river watershed. *Aquatic Sciences*, *68*(1), 40-51.

Geider, R. J., MacIntyre, H. L., & Kana, T. M. (1997). Dynamic model of phytoplankton growth and acclimation: responses of the balanced growth rate and the chlorophyll a: carbon ratio to light, nutrient-limitation and temperature. *Marine Ecology Progress Series*, *148*, 187-200.

George, D. G., & Jones, D. H. (1987). Catchment effects on the horizontal distribution of phytoplankton in five of Scotland's largest freshwater lochs. *The Journal of Ecology*, 43-59.

Gilbert, P. M. (2012). Ecological stoichiometry and its implications for aquatic ecosystem sustainability. *Current Opinion in Environmental Sustainability*, *4*(3), 272-277.

Gray, J. S. (1997). Marine biodiversity: patterns, threats and conservation needs. *Biodiversity and conservation*, *6*(1), 153-175.

Green, W. R., Robertson, D. M., & Wilde, F. D. (2015). Lakes and reservoirs-Guidelines for study design and sampling: U.S. Geological Survey Techniques of Water-Resources Investigations, book 9, chap. A10, sec. 10.5.1, accessed June 29, 2017, from https://water.usgs.gov/owq/FieldManual/Chapter10/pdf/ch10.pdf

Guildford, S. J., & Hecky, R. E. (2000). Total nitrogen, total phosphorus, and nutrient limitation in lakes and oceans: Is there a common relationship?.*Limnology and Oceanography*, *45*(6), 1213-1223.

Guildford, S. J., Bootsma, H. A., Fee, E. J., Hecky, R. E., & Patterson, G. (2000). Phytoplankton nutrient status and mean water column irradiance in Lakes Malawi and Superior. *Aquatic Ecosystem Health & Management*, *3*(1), 35-45.

Halder, J., Decrouy, L., & Vennemann, T. W. (2012). Mixing of Rhône River water in Lake Geneva (Switzerland–France) inferred from stable hydrogen and oxygen isotope profiles. *Journal of Hydrology*, *477*, 152-164.

Hall, S. R., Pauliukonis, N. K., Mills, E. L., Rudstam, L. G., Schneider, C. P., Lary, S. J., & Arrhenius, F. (2003). A comparison of total phosphorus, chlorophyll a, and zooplankton in embayment, nearshore, and offshore habitats of Lake Ontario. *Journal of Great Lakes Research*, *29*(1), 54-69.

Hanson, P. C., Bade, D. L., Carpenter, S. R., & Kratz, T. K. (2003). Lake metabolism: relationships with dissolved organic carbon and phosphorus. *Limnology and Oceanography*, *48*(3), 1112-1119.

Hecky, R.E., Bootsma. H.A., Mugidde, R.M., & Bugenyl, F.W.B. (1996). Phosphorus pumps, nitrogen sinks, andsilicon drains: Plumbing nutrients in the African Great Lakes, 205–224. *In*T. C. Johnson and E. O. Odada [eds.], Thelimnology, climatology, andpaleoclimatology of the EastAfrican lakes. Gordon and Breach.

Hecky, R. E., & Hesslein, R. H. (1995). Contributions of benthic algae to lake food webs as revealed by stable isotope analysis. *Journal of the North American Benthological Society*, *14*(4), 631-653.

Heinen, E. A., & McManus, J. (2004). Carbon and nutrient cycling at the sediment-water boundary in western Lake Superior. *Journal of Great Lakes Research*, *30*, 113-132.

Herdendorf, C. E. (1982). Large lakes of the world. *Journal of Great Lakes Research*, *8*(3), 379-412.

Hogg, C. A., Marti, C. L., Huppert, H. E., & Imberger, J. (2013). Mixing of an interflow into the ambient water of Lake Iseo. *Limnol. Oceanogr*, *58*(2), 579-592.

Homer, C. G., Dewitz, J. A., Yang, L., Jin, S., Danielson, P., Xian, G., ... & Megown, K. (2015). Completion of the 2011 National Land Cover Database for the conterminous United States-Representing a decade of land cover change information. *Photogrammetric Engineering and Remote Sensing*, *81*(5), 345-354.

Inamdar, S. P., O'leary, N., Mitchell, M. J., & Riley, J. T. (2006). The impact of storm events on solute exports from a glaciated forested watershed in western New York, USA. *Hydrological Processes*, *20*(16), 3423-3439.

Ivanikova, N. V., Popels, L. C., McKay, R. M. L., & Bullerjahn, G. S. (2007). Lake Superior supports novel clusters of cyanobacterial picoplankton. *Applied and environmental microbiology*, *73*(12), 4055-4065.

Jackson, G. A. (1988). Kelvin wave propagation in a high drag coastal environment. *Journal of physical oceanography*, *18*(11), 1733-1743.

Jackson, N. L., Nordstrom, K. F., & Farrell, E. J. (2017). Longshore sediment transport and foreshore change in the swash zone of an estuarine beach. *Marine Geology*, *386*, 88-97.

Jansson, M., Bergström, A. K., Blomqvist, P., & Drakare, S. (2000). Allochthonous organic carbon and phytoplankton/bacterioplankton production relationships in lakes. *Ecology*, *81*(11), 3250-3255.

Jassby, A. D., Cloern, J. E., & Powell, T. M. (1993). Organic carbon sources and sinks in San Francisco Bay: variability induced by river flow. *Marine Ecology Progress Series*, 39-54.

Ji, Z. G., & Jin, K. R. (2006). Gyres and seiches in a large and shallow lake. *Journal of Great Lakes Research*, *32*(4), 764-775.

Johengen, T. H., Biddanda, B. A., & Cotner, J. B. (2008). Stimulation of Lake Michigan plankton metabolism by sediment resuspension and river runoff. *Journal of Great Lakes Research*, *34*(2), 213-227.

Kalff, J. (2002). *Limnology: inland water ecosystems* (Vol. 592). New Jersey: Prentice Hall.

Karlsson, J., Byström, P., Ask, J., Ask, P., Persson, L., & Jansson, M. (2009). Light limitation of nutrient-poor lake ecosystems. *Nature*, *460*(7254), 506-509.

Kasprzak, P., Padisák, J., Koschel, R., Krienitz, L., & Gervais, F. (2008). Chlorophyll a concentration across a trophic gradient of lakes: An estimator of phytoplankton biomass?. *Limnologica-Ecology and Management of Inland Waters*, *38*(3), 327-338.

Kawamiya, M. (2001). Mechanism of offshore nutrient supply in the western Arabian Sea. *Journal of marine research*, *59*(5), 675-696.

Kelly, J. R., Yurista, P., Starry, M., Scharold, J., Bartsch, W., & Cotter, A. (2015). Exploration of spatial variability in nearshore water quality using the first Great Lakes National Coastal Condition Assessment survey. *Journal of Great Lakes Research*, *41*(4), 1060-1074.

Kritzberg, E.S., J.J. Cole, M.L. Pace, W. Granéli, & Bade, D.L. (2004). Autochthonous versus allochthonous carbon sources of bacteria: Results from whole-lake 13C addition experiments. *Limnol. Oceanogr., 49*(2), 588-596.

Larson, N.J., LaLiberte, G.D., & Van Stappen, J. (2012). Blue-green Algae Observed in Lake Superior.Joint Press Release—Wisconsin Department of Natural Resources and Apostle Islands National Seashore (July 23). http://dnr.wi.gov/news/BreakingNews_Print.asp?id=2440

Lesht, B. M., Stroud, J. R., McCormick, M. J., Fahnenstiel, G. L., Stein, M. L., Welty, L. J., & Leshkevich, G. A. (2002). An event-driven phytoplankton bloom in southern Lake Michigan observed by satellite. *Geophysical Research Letters*, *29*(8).

Lohrenz, S. E., Dagg, M. J., & Whitledge, T. E. (1990). Enhanced primary production at the plume/oceanic interface of the Mississippi River. *Continental shelf research*, *10*(7), 639-664.

Lohrenz, S. E., Fahnenstiel, G. L., Redalje, D. G., Lang, G. A., Chen, X., & Dagg, M. J. (1997). Variations in primary production of northern Gulf of Mexico continental shelf waters linked to nutrient inputs from the Mississippi River. *Marine Ecology Progress Series*, 45-54.

Lou, J., Schwab, D. J., Beletsky, D., & Hawley, N. (2000). A model of sediment resuspension and transport dynamics in southern Lake Michigan. *Journal of Geophysical Research: Oceans*, *105*(C3), 6591-6610.

MacIntyre, S., Sickman, J. O., Goldthwait, S. A., & Kling, G. W. (2006). Physical pathways of nutrient supply in a small, ultraoligotrophic arctic lake during summer stratification. *Limnology and Oceanography*, *51*(2), 1107-1124.

Mackey, S. D., & Goforth, R. R. (2005). Great Lakes nearshore habitat science. *Journal of Great Lakes Research*, *31*, 1-5.

Makarewicz, J.C., Lewis, T.W., Pennuto, C.M., Atkinson, J.F., Edwards, W.J., Boyer, G.L., Howell, E.T., & Thomas, G. (2012). Physical and chemical characteristics of the nearshore zone of Lake Ontario. *Journal of Great Lakes Research*, *38*, 21-31.

Martin, R. F. (2000). General Deming regression for estimating systematic bias and its confidence interval in method-comparison studies. *Clinical chemistry*, *46*(1), 100-104.

McCullough, G. K., Barber, D., & Cooley, P. M. (2007). The vertical distribution of runoff and its suspended load in Lake Malawi. *Journal of Great Lakes Research*, *33*(2), 449-465.

McManus, M. A., Alldredge, A. L., Barnard, A. H., Boss, E., Case, J. F., Cowles, T. J., ... & Herren, C. M. (2003). Characteristics, distribution and persistence of thin layers over a 48 hour period. *Marine Ecology Progress Series*, *261*, 1-19.

Mesri, G. & Olson, R.E. (1971). Mechanisms controlling the permeability of clays. *Clays and Clay Minerals, 19*, 161-158.

Megard, R. O., Kuns, M. M., Whiteside, M. C., & Downing, J. A. (1997). Spatial distributions of zooplankton during coastal upwelling in western Lake Superior. *Limnology and Oceanography*, *42*(5), 827-840.

Millero, F. J. (2007). The marine inorganic carbon cycle. *Chemical reviews*, *107*(2), 308-341.

Minor, E. C., B. Forsman, & Guildford, S. J. (2014). The effect of a flood pulse on the water column of western Lake Superior, USA. *Journal of Great Lakes Research*, *40*(2), 455-462.

Mortimer, C. H. (2006). Inertial oscillations and related internal beat pulsations and surges in Lakes Michigan and Ontario. *Limnology and oceanography*, *51*(5), 1941-1955.

Mouw, C. B., Chen, H., McKinley, G. A., Effler, S., O'Donnell, D., Perkins, M. G., & Strait, C. (2013). Evaluation and optimization of bio-optical inversion algorithms for remote sensing of Lake Superior's optical properties. *Journal of Geophysical Research: Oceans*, *118*(4), 1696-1714.

Müller, B., Maerki, M., Schmid, M., Vologina, E. G., Wehrli, B., Wüest, A., & Sturm, M. (2005). Internal carbon and nutrient cycling in Lake Baikal: sedimentation, upwelling, and early diagenesis. *Global and Planetary Change*, *46*(1), 101-124.

Murthy, C. R., & Dunbar, D. S. (1981). Structure of the flow within the coastal boundary layer of the Great Lakes. *Journal of Physical Oceanography*, *11*(11), 1567-1577.

Murthy, C. R., Simons, T. J., & Lam, D. C. L. (1986). Dynamic and transport modelling of the Niagara River Plume in Lake Ontario. *Rapports et procès-verbaux des réunions-Conseil international pour l'exploration de la mer*, *186*, 150-165.

Nalewajko, C., Lee, K., & Shear, H. (1981). Phosphorus kinetics in Lake Superior: light intensity and phosphate uptake in algae. *Canadian Journal of Fisheries and Aquatic Sciences*, *38*(2), 224-232.

Nezlin, N. P., & DiGiacomo, P. M. (2005). Satellite ocean color observations of stormwater runoff plumes along the San Pedro Shelf (southern California) during 1997–2003. *Continental Shelf Research*, *25*(14), 1692-1711.

Niemi, G. J., Kelly, J. R., & Danz, N. P. (2009). Environmental indicators for the coastal region of the North American Great Lakes: introduction and prospectus.

Padisák, J., Krienitz, L., Koschel, R., & Nedoma, J. (1997). Deep-layer autotrophic picoplankton maximum in the oligotrophic Lake Stechlin, Germany: origin, activity, development and erosion. *European Journal of Phycology*, *32*(4), 403-416.

Peterson, D. H., Perry, M. J., Bencala, K. E., & Talbot, M. C. (1987). Phytoplankton productivity in relation to light intensity: a simple equation. *Estuarine, Coastal and Shelf Science*, *24*(6), 813-832.

Pomeroy, L. R., leB. Williams, P. J., Azam, F., & Hobbie, J. E. (2007). The microbial loop. *Oceanography*, *20*(2), 28-33.

Popovskaya, G. I. (2000). Ecological monitoring of phytoplankton in Lake Baikal. *Aquatic Ecosystem Health & Management*, *3*(2), 215-225.

Prairie, Y. T., Bird, D. F., & Cole, J. J. (2002). The summer metabolic balance in the epilimnion of southeastern Quebec lakes. *Limnology and Oceanography*, *47*(1), 316-321.

Rabalais, N. N., Turner, R. E., Justić, D., Dortch, Q., Wiseman, W. J., & Sen Gupta, B. K. (1996). Nutrient changes in the Mississippi River and system responses on the adjacent continental shelf. *Estuaries and coasts*, *19*(2), 386-407.

Rao, Y. R., & Murthy, C. R. (2001). Coastal boundary layer characteristics during summer stratification in Lake Ontario. *Journal of physical oceanography*, *31*(4), 1088-1104.

Richards, F. A., & Thompson, T. G. (1952). The estimation and characterization of plankton populations by pigment analyses. 2. A spectrophotometric method for the estimation of plankton pigments. *Journal of Marine Research*, *11*(2), 156-172.

Ries, K. G. (2007). *The national streamflow statistics program: A computer program for estimating streamflow statistics for ungaged sites*. DIANE Publishing.

Russ, M. E., N. E. Ostrom, H. Gandhi, P. H. Ostrom, & Urban, N. R. (2004). Temporal and spatial variations in R: P ratios in Lake Superior, an oligotrophic freshwater environment. *Journal of Geophysical Research: Oceans*, *109*(C10).

Salonen, K., Sarvala, J., Järvinen, M., Langenberg, V., Nuottajärvi, M., Vuorio, K., & Chitamwebwa, D. B. R. (1999). Phytoplankton in Lake Tanganyika—vertical and horizontal distribution of in vivo fluorescence. In *From Limnology to Fisheries: Lake Tanganyika and Other Large Lakes* (pp. 89-103). Springer Netherlands.

Sander, R. (2015). Compilation of Henry's law constants (version 4.0) for water as solvent. *Atmospheric Chemistry & Physics*, *15*(8).

San Martin, E., Irigoien, X., Harris, R. P., López-Urrutia, A., Zubkov, M. V., & Heywood, J. L. (2006). Variation in the transfer of energy in marine plankton along a productivity gradient in the Atlantic Ocean. *Limnology and Oceanography*, *51*(5), 2084-2091.

Scheu, K. R., D. A. Fong, S. G. Monismith, & Fringer, O.B. (2015). Sediment transport dynamics near a river inflow in a large alpine lake. *Limnology and Oceanography*, *60*(4), 1195-1211.

Schindler, D. W., & Nighswander, J. E. (1970). Nutrient supply and primary production in Clear Lake, eastern Ontario. *Journal of the Fisheries Board of Canada*, *27*(11), 2009-2036.

Schindler, D. W. (1978). Factors regulating phytoplankton production and standing crop in the world's freshwaters. *Limnology and Oceanography, 23*(3), 478-486.

Shchepetkin, A. F., & McWilliams, J. C. (2003). A method for computing horizontal pressure-gradient force in an oceanic model with a nonaligned vertical coordinate. *Journal of Geophysical Research: Oceans*, *108*(C3).

Smith, E. M., & Prairie, Y. T. (2004). Bacterial metabolism and growth efficiency in lakes: the importance of phosphorus availability. *Limnology and Oceanography*, *49*(1), 137-147.

Stainton, M., Capel, M. J. , & Armstrong, F. A. J. (1977). Chemical analysis of fresh water.

Steinman, A., Chu, X., & Ogdahl, M. (2009). Spatial and temporal variability of internal and external phosphorus loads in Mona Lake, Michigan. *Aquatic Ecology*, *43*(1), 1-18.

Sterner, R. W., Smutka, T. M., McKay, R. M. L., Xiaoming, Q., Brown, E. T., & Sherrell, R. M. (2004). Phosphorus and trace metal limitation of algae and bacteria in Lake Superior. *Limnology and Oceanography*, *49*(2), 495-507.

Sterner, R. W. (2010). In situ-measured primary production in Lake Superior. *Journal of Great Lakes Research*, *36*(1), 139-149.

Sterner, R. W. (2011). C: N: P stoichiometry in Lake Superior: freshwater sea as end member. *Inland Waters*, *1*(1), 29-46.

Stortz, K., Clapper, R., & Sydor, M. (1976). Turbidity sources in Lake Superior. *Journal of Great Lakes Research*, *2*(2), 393-401.

Straškrábová, V., Izmest'yeva, L. R., Maksimova, E. A., Fietz, S., Nedoma, J., Borovec, J., ... & Pislegina, E. V. (2005). Primary production and microbial activity in the euphotic zone of

Lake Baikal (Southern Basin) during late winter. *Global and Planetary Change*, *46*(1), 57-73.

Strayer, D. L., & Findlay, S. E. (2010). Ecology of freshwater shore zones. *Aquatic Sciences*, *72*(2), 127-163.

Takahashi, T., Sutherland, S. C., Sweeney, C., Poisson, A., Metzl, N., Tilbrook, B., Bates, N., Wanninkhof, R., Feely, R. A., Sabine, C., & Olafsson, J. (2002). Global sea–air CO 2 flux based on climatological surface ocean pCO 2, and seasonal biological and temperature effects. *Deep Sea Research Part II: Topical Studies in Oceanography*, *49*(9), 1601-1622.

Thupaki, P. (2012). *Nearshore Hydrodynamics and the Fate and Transport of Indicator Bacteria in Lake Michigan: Field Experiments and Numerical Modeling*. Michigan State University. Civil and Environmental Engineering.

Thrane, J. E., Hessen, D. O., & Andersen, T. (2014). The absorption of light in lakes: negative impact of dissolved organic carbon on primary productivity. *Ecosystems*, *17*(6), 1040-1052.

Tranvik, L. J. (1992). Allochthonous dissolved organic matter as an energy source for pelagic bacteria and the concept of the microbial loop. *Hydrobiologia*, *229*(1), 107-114.

Turschak, B. A., Bunnell, D., Czesny, S., Höök, T. O., Janssen, J., Warner, D., & Bootsma, H. A. (2014). Nearshore energy subsidies support Lake Michigan fishes and invertebrates following major changes in food web structure. *Ecology*, *95*(5), 1243-1252.

United States Environmental Protection Agency. (1979). Impact of Nonpoint Pollution Control on Western Lake Superior. EPA - 905/9-76-002. U.S. Environmental Protection Agency, Washington, DC.

United States Environmental Protection Agency. (2009). National Coastal Condition Assessment: Field Operations Manual. EPA-841-R-09-003. U.S. Environmental Protection Agency, Washington, DC.

Urban, N. R., Apul, D. S., & Auer, M. T. (2004). Community respiration rates in Lake Superior. *Journal of Great Lakes Research*, *30*, 230-244.

Vadeboncoeur, Y., Lodge, D. M., & Carpenter, S. R. (2001). Whole-lake fertilization effects on distribution of primary production between benthic and pelagic habitats. *Ecology*, *82*(4), 1065-1077.

Vadeboncoeur, Y., Vander Zanden, M. J., & Lodge, D. M. (2002). Putting the lake back together: Reintegrating benthic pathways into lake food web models. *Bioscience*, *52*(1), 44.

Vadeboncoeur, Y., Peterson, G., Vander Zanden, M. J., & Kalff, J. (2008). Benthic algal production across lake size gradients: interactions among morphometry, nutrients, and light. *Ecology*, *89*(9), 2542-2552.

Vadeboncoeur, Y., McIntyre, P. B., & Vander Zanden, M. J. (2011). Borders of biodiversity: life at the edge of the world's large lakes. *Bioscience*, *61*(7), 526-537.

Van de Bogert, M. C., Carpenter, S. R., Cole, J. J., & Pace, M. L. (2007). Assessing pelagic and benthic metabolism using free water measurements. *LimnolOceanogr Methods*, *5*, 145-155.

Vollenweider, R. A., Munawar, M., & Stadelmann, P. (1974). A comparative review of phytoplankton and primary production in the Laurentian Great Lakes. *Journal of the Fisheries Board of Canada*, *31*(5), 739-762.

Vollenweider, R. A. (1976). Advances in defining critical loading levels for phosphorus in lake eutrophication. *Memoriedell'IstitutoItaliano di Idrobiologia, Dott. Marco de MarchiVerbaniaPallanza*.

Wang, B. (2002). Kelvin waves. *Encyclopedia of Atmospheric Sciences*, 1062-1068.

Wanninkhof, R. (1992). Relationship between wind speed and gas exchange over the ocean. *Journal of Geophysical Research: Oceans*, *97*(C5), 7373-7382.

Wanninkhof, R., Asher, W. E., Ho, D. T., Sweeney, C., & McGillis, W. R. (2009). Advances in quantifying air-sea gas exchange and environmental forcing.

Wanninkhof, R. (2014). Relationship between wind speed and gas exchange over the ocean revisited. *Limnol. Oceanogr. Methods*, *12*(6), 351-362.

Wawrik, B., & Paul, J. H. (2004). Phytoplankton community structure and productivity along the axis of the Mississippi River plume in oligotrophic Gulf of Mexico waters. *Aquatic Microbial Ecology*, *35*(2), 185-196.

Wetzel, R. G. (2001). *Limnology: lake and river ecosystems*. Gulf Professional Publishing.

Wolter, P. T., Johnston, C. A., & Niemi, G. J. (2006). Land use land cover change in the US Great Lakes basin 1992 to 2001. *Journal of Great Lakes Research*, *32*(3), 607-628.

Yang, K.S., Chen, Y.Y., Li, M.S., & Hsu, H.C. (2013). Theoretical and Experimental Study of Breaking Wave on Sloping Bottoms. *China Ocean Engineering, 26,* 6, 737-750.

Yoshii, K. (1999). Stable isotope analyses of benthic organisms in Lake Baikal. *Hydrobiologia*, *411*, 145-159.

Yurista, P. & Kelly, J.R. (2009). Spatial patterns of water quality and plankton from high-resolution continuous *in situ* sensing along a 537-km nearshore transect of western Lake Superior, 2004. *State of Lake Superior. Edited by M. Munawar and IF Munawar. Aquatic Ecosystem Health and Management Society, Burlington, Ont., Canada*, 439-471.

Yurista, P., Kelly, J.R., & Miller, S.E.. (2011). Lake Superior: Nearshore variability and a landscape driver concept. *Aquatic Ecosystem Health and Management, 14*(4), 345-355.

Yurista, P. M., Kelly, J. R., Cotter, A. M., Miller, S. E., & Van Alstine, J. D. (2015). Lake Michigan: Nearshore variability and a nearshore–offshore distinction in water quality. *Journal of Great Lakes Research*, *41*(1), 111-122.

APPENDIX A: Oxygen Percent Saturation Function

$$\ln[O_2]_{sat}(T) = a_0 + \frac{a_1}{T} + \frac{a_2}{T} + \frac{a_3}{T} + \frac{a_4}{T}$$

$a_0 = -1.352996 \times 10^{2}$

$a_1 = 1.572288 \times 10^{5}$

$a_2 = -6.637149 \times 10^{7}$

$a_3 = 1.243678 \times 10^{10}$

$a_4 = -8.621061 \times 10^{12}$

$$f(T) = b_0 + \frac{b_1}{T} + \frac{b_2}{T^2}$$

$b_0 = -2.0573 \times 10^{-2}$

$b_1 = 1.2142 \times 10^{1}$

$b_2 = -2.3631 \times 10^{3}$